Aus der Medizinischen Klinik und Poliklinik III der Ludwig-Maximilians-Universität München
Direktor: Prof. Dr. Wolfgang Hiddemann

in Kooperation mit der
Klinik und Poliklinik für Radiologie der Ludwig-Maximilians-Universität München
Direktor: Prof. Dr. habil. Jens Ricke

Surrogate MRI markers for chemodosimetry of doxorubicin with thermosensitive liposomes in tumors

Dissertation
zum Erwerb des Doktorgrades der Humanbiologie
an der Medizinischen Fakultät der
Ludwig-Maximilians-Universität zu München

vorgelegt von
Linus Willerding

aus
Bad Nauheim

2017

Mit Genehmigung der

„Medizinischen Fakultät der Universität München“

Berichterstatter:

Prof. Dr. med. Lars H. Lindner

Mitberichterstatter:

Prof. Dr. med. Thorsten Johnson

Prof. Dr. med. Dr. phil. Fuat Oduncu

Mitbetreuung durch die promovierten Mitarbeiter:

Dr. rer. biol. hum. Dipl. Phys. Michael Peller

Dr. rer. nat. Martin Hossann

Dekan

Prof. Dr. med. dent. Reinhard Hickel

Tag der mündlichen Prüfung: 29. November 2017

TABLE OF CONTENTS

ABSTRACT

Purpose: The efficacy of systemically-applied anti-cancer drugs is limited by insufficient selectivity, and the maximum applicable dose is limited by side effects. Improved effectiveness can be achieved by targeting the cytotoxic drugs directly to the tumor. Using thermosensitive liposomes (TSL) as drug carriers, such targeting is achieved by control of temperature in the target volume. The approach can be further improved by magnetic resonance imaging guided local hyperthermia (HT) to visualize the content release using contrast agent (CA)-loaded TSL. Such visualization is considered to be an important tool for further improvement of HT/chemotherapy concepts based on TSL, and may facilitate chemodosimetry during HT. Real-time imaging of drug targeting offers better treatment control, and is an important step towards personalized medicine. Therefore, in this work quantitative assessment of HT-induced doxorubicin release (chemodosimetry) in tumors is examined by injecting a mixture of TSL loaded with CA or DOX into the tumors, and using MRI parameters.

Methods: In the first part of this work a novel laser light-based HT devise was developed to investigate MRI-guided HT for preclinical research. To prove its effectiveness, the new device was compared systematically with the frequently used cold light lamp and water bath HT. Experiments were performed in 18 male Brown Norway rats with a syngeneic soft tissue sarcoma (BN 175) located on each hind leg. One tumor was heated while the second tumor remained unheated as a reference. Six animals were investigated per HT method. $DPPG_2$-TSL were injected i.v. at a stable tumor temperature above 40 °C. Thereafter, temperature was maintained for 60 min. Total DOX concentration in plasma, tumor tissue, and muscle was determined post-therapy by high pressure liquid chromatography (HPLC).

In the second part, the new HT device was used to identify surrogate MRI markers to quantify HT-enhanced DOX delivery to a heated tumor. These experiments were performed in an additional six male Brown Norway rats with one syngeneic tissue soft tissue sarcoma (BN175) located on each hind leg. Tumor temperature was monitored using an intratumoral fiberoptic temperature probe. In group A (N=4), one tumor was superficially selectively heated by a 940 nm diode laser with a new MRI-compatible applicator, while the second tumor remained unheated. After reaching a temperature of 40°C, a bolus of mixed DPPG2-TSL and CA-TSL was administered i.v.. After 1 h, HT was stopped and the tumor was allowed to cool down to the temperature determined pre-HT. In group B (N=2),

the same experiment was performed without HT. Finally, tumors were excised for DOX measurement by HPLC. MRI was performed at 3T. T_1-mapping using variable flip angle was established before and after HT. Furthermore, dynamic mapping of T_1 and the phase were performed during the experiment. Phase change (PC), T_1- and T_1-related parameters (absolute and relative changes), or areas under the curve (AUC) of T_1dyn(t) were correlated with the DOX enhancement in the corresponding tissue.

Results: All heating methods exhibited highly effective DOX delivery by TSL with 4.5-23.1 ng/mg found in the heated tumors. In contrast, the mean DOX concentration in the unheated tumors, and in abdominal muscle, was 0.5 ± 0.1 ng/mg. Independent of the HT methods investigated during this study, more DOX was found in the smaller tumors. By comparison, the water bath induced the lowest DOX delivery in large tumors, but still displayed a fourfold higher DOX compared to the un-heated tumors. Using the laser-based applicator, a DOX deposition 13 times higher than levels found in unheated tumors was possible for larger tumors, where levels in smaller tumors were recorded 15 times higher compared to the unheated tumors. Temperature gradients inside the tumor volume were higher with the laser and cold light lamp (– 0.3 °C/mm to – 0.5 °C /mm) than with the water bath (– 0.1 °C/mm and – 0.2 °C/mm).

The MRI experiments for chemodosimetry in group A showed a tumor temperature of 41.1±1.2°C during one hour. HPLC of 18 tumor samples demonstrated highly efficient DOX delivery to heated tumors. Compared to unheated tumors, DOX delivery was increased by a factor of 9.4 ± 2.9. All investigated T_1 and PC parameters were highly correlated with DOX concentrations measured by HPLC. Using the highly significant linear relationship of MRI and DOX, MRI-derived DOX parameter maps of the tumors were calculated.

Conclusion: The comparative work with different heating methods has demonstrated that DPPG2-TSL drug delivery and targeting is highly effective independently from the HT method. Nevertheless, it was also shown that the effectiveness of the therapies is dependent on the method of heating and on tumor size. Both factors must be considered in study designs, and when comparing results with other studies in temperature-triggered drug delivery. In this work, the cold light lamp and new laser applicator furnished more efficient drug delivery than water bath heating.

Furthermore, this was the first time that a mixture of TSL encapsulating either a clinically approved CA or DOX has been investigated for in vivo DOX concentration assessment. An assessment and visualization of DOX deposited in tumors was possible with the MRI. A variety of static or dynamic MRI surrogate markers based on T_1 or phase appeared to correlate with the DOX concentration in the tumor tissue. MR thermometry was affected by

CA-TSL, but phase information was confirmed to be suitable for DOX assessment. Local DOX differences in the tumors indicated the need for visualization of drug release for further improvement of targeted chemotherapy.

In conclusion, promising MRI surrogate parameters were also identified for the assessment of DOX tissue concentration when using a mixture of CA-TSL and DOX-TSL.

ZUSAMMENFASSUNG

Motivation: Die therapeutische Wirkung von systemisch verabreichten Chemotherapeutika in soliden Tumoren ist limitiert durch die fehlende Selektivität der Medikamente und die maximal mögliche verabreichbare Dosis welche durch Nebenwirkungen begrenzt ist. Die Effektivität kann durch ein gezieltes Freisetzen der Medikamente im Tumor gesteigert werden. Mit Hilfe von temperatursensitiven Liposomen (TSL) ist es möglich die Freisetzung des Medikaments durch lokaler Temperaturerhöhung (HT) zu steuern. Eine Möglichkeit zur weiteren Verbesserung dieser Methodik bietet die Visualisierung der Wirkstofffreisetzung mit Hilfe der Magnetresonanztomographie (MRT) gestützten lokalen HT. Dies wird durch die Beladung der TSL mit MRT Kontrastmittel (CA) erreicht. Die Visualisierung wird als Voraussetzung zur Verbesserung der HT kombiniert mit der Chemotherapie mit TSL gesehen und ermöglicht eine Chemodosimetrie während der HT. Die Analyse der Wirkstoffaufnahme in den Tumor in Echtzeit ermöglicht eine bessere Therapiesteuerung und ist ein Schritt hin zur personalisierten Medizin. Ziel dieser Arbeit war daher die quantitative Bestimmung des durch HT im Gewebe freigesetzten Medikaments im Tumor unter Verwendung verschiedener MRT Parameter und mit Hilfe von DOX beladenen TSL gemischt mit CA beladenen TSL.

Methoden: Um eine vorklinische Untersuchung zur MRT-überwachten Hyperthermie zu ermöglichen wurde ein MR-kompatibler, auf Laserlicht basierender HT-Applikator entwickelt. Die Effektivität dieses neuen Applikators wurde in einer ersten Studie systematisch durch den Vergleich mit etablierten experimentellen Erwärmungsmethoden wie einer Kaltlichtlampe und einem Wasserbad getestet. Bei 18 männlichen „Brown Norway“ Ratten mit syngenen Weichteilsarkomen (BN 175) an beiden Hinterläufen wurde jeweils nur ein Tumor erwärmt. Der zweite, nicht erwärmte Tumor diente als Referenz. Die Wirkung der drei Erwärmungsmethoden auf die erreichte DOX-Konzentration wurde an jeweils 6 Tieren untersucht. Nach Erreichen einer stabilen Tumortemperatur von über 40°C unter Verwendung einer der drei HT-Methoden wurde eine Mischung aus DPPG2-TSL mit verkapseltem DOX oder CA intravenös injiziert. Anschließend wurde die Tumortemperatur über weitere 60min stabil gehalten. Nach der Behandlung wurde die DOX Konzentration im Plasma, im Tumor und im Muskelgewebe mit der Hochdruckflüssigkeitschromatographie (HPLC) gemessen.

Mit dem neuen Laserlicht basierten HT-Applikator wurden in einer zweiten Studie mögliche MR Parameter für eine MR-gestützte Chemodosimetrie an 6 männlichen „Brown Nor-

way“ Raten mit jeweils einem syngenen Weichteilsarkom (BN 175) an jedem Hinterlauf untersucht. In einer Gruppe (A) mit 4 Tieren wurde jeweils ein Tumor mit dem neuen MRT kompatiblen Laserapplikator erwärmt, während der zweite nicht erwärmte Tumor als Kontrolle diente. Nachdem im erwärmten Tumor eine stabile Temperatur über 40 °C erreicht wurde, ist ein Gemisch aus $DPPG_2$-TSL und CA-TSL i.v. injiziert worden. Nach einer Stunde wurde die Erwärmung gestoppt und der Tumor kühlte bis auf die Temperatur vor der Erwärmung ab. In der zweiten Gruppe (B, N=2) wurde das gleiche Experiment, jedoch ohne Erwärmung durchgeführt. Die Tumortemperatur wurde bei allen Untersuchungen mit einer intratumoral gelegten fiberoptischen Temperatursonde überwacht. Nach Abschluss wurden die Tumore zur Analyse mit der HPLC entnommen. Die MRT-Bildgebung bei 3T fand kontinuierlich während des ganzen Verlaufs statt. Mit der variablen Flipwinkel Methode wurden vor und nach Hyperthermie T_1-Parameterkarten erstellt. Zusätzlich sind zeitaufgelöste T_1 Messungen und Phasenmessungen während der Experimente durchgeführt worden. Die Phasenänderungen, die T_1-Relaxationszeiten und weitere T_1 abhängige Parameter (absolute und relative Änderung oder die Fläche unter der Kurve (AUC) der T_1-Zeitverlaufs) wurden mit der DOX Anreicherung im dazu gehörigen Gewebevolumen verglichen.

Ergebnisse: Alle verwendeten Erwärmungsmethoden führten zu einer deutlich verbesserten Anreicherung von DOX (4,5-23,1 ng/mg) durch den Einsatz von TSL im erwärmten Tumor. Im Gegensatz dazu lag die durchschnittliche DOX Konzentration im nicht erwärmten Tumor und im abdominellen Muskelgewebe bei 0,5 +- 0,1 ng/mg. Unabhängig von der verwendeten HT Methode wurde mehr DOX in den kleineren Tumoren gefunden.
Das Wasserbad führte zur geringsten Anreicherung in den großen Tumoren, zeigte jedoch im Gegensatz zu den nicht erwärmten Tumoren immer noch eine vierfach höhere DOX-Anreicherung. Die Erwärmung mit dem Laserapplikator führte zu einer 13-fach höheren DOX Anreicherung für die großen Tumore und einer 15-fach höheren DOX-Anreicherung in den kleinen Tumoren im Vergleich zum nicht erwärmten Tumor. Die Temperaturgradienten im Tumor bei Erwärmung mit dem Laserapplikator oder der Kaltlichtlampe (- 0,3 °C/mm bis - 0,5 °C/mm) waren höher im Vergleich zu denen des Wasserbads (- 0,1 °C/mm bis -0,2 °C/mm)

Die MRT-Experimente im zweiten Teil der Arbeit zur Chemodosimetrie wurden bei einer mittleren Tumortemperatur von 41.1 ± 1,2 °C während einer Stunde in Gruppe A durchgeführt. Die HPLC Analyse der 18 Tumorproben zeigte eine sehr effiziente DOX Anreicherung im erwärmten Tumor im Vergleich zu den nicht erwärmten Tumoren. Die DOX Anreicherung war um einen Faktor von 9,4 ± 2,9 höher. Alle untersuchten T1 und Phasenparameter besaßen eine hohe Korrelation mit der HPLC gemessenen DOX Konzentration.

Unter der Verwendung der hoch signifikanten linearen Abhängigkeit der MR Parameter und der DOX-Werte wurden DOX Konzentrationskarten der Tumore berechnet.

Fazit: Die Vergleichsstudie mit unterschiedlichen Erwärmungsmethoden hat gezeigt, dass unabhängig von der Erwärmungsmethode ein sehr effektiver zielgerichteter Medikamententransport und –freisetzung mit DPPG2-TSL erreicht wird. Gleichwohl ist die Höhe der Effektivität sowohl von der Methode als auch von der Tumorgröße abhängig. Diese beiden Faktoren sollten somit in weiteren Studien und bei dem Vergleich von Ergebnissen verschiedener Studien zur temperaturinduzieren Medikamentenfreisetzung berücksichtigt werden. In dieser Studie ist eine effektivere Medikamentenanreicherung im Tumorgewebe durch die Erwärmung mit der Kaltlichtlampe oder dem neu entwickeltem Laserlichtapplikator im Vergleich zur Erwärmung mit dem Wasserbad erreicht worden.

Erstmals konnte auch gezeigt werden, dass auch eine Mischung aus TSL, die entweder ein klinisches zugelassenes MR CA oder DOX enthielten, zur Messung einer in vivo DOX-Gewebekonzentration verwendet werden kann. Eine Vielzahl von statischen und dynamischen T_1 oder phasenbasierenden MRT Parametern korrelierten mit der DOX Konzentration im Tumorgewebe. Damit waren eine Abschätzung des im Tumorgewebe platzierten DOX mit dem MRT und eine entsprechende Visualisierung der DOX-Verteilung im Tumor möglich. Die MR-Thermometrie wurde durch die CA-TSL beeinträchtigt, jedoch konnten die gleichen Phaseninformationen stattdessen für die DOX-Abschätzung genutzt werden. Lokale Unterschiede in der DOX-Gewebekonzentration zeigen, dass die Visualisierung der Medikamentenfreisetzung und der Medikamentenaufnahmen für eine weitere Verbesserung der zielgerichteten Chemotherapie wichtige zusätzliche Informationen liefern können.

1. INTRODUCTION

In highly developed regions worldwide, cancer has been the second most common cause of death over the past few decades, with circulatory diseases being the most responsible for fatalities [1]. Different methods of tumor therapy are available to patient, such as surgery, radiation therapy and chemotherapy, and hyperthermia. These methods are used depending on the type, grade and stage of the tumor, and are generally used in combination. Due to the severe side effects of chemotherapy, different improvements to the therapy have been developed. Regional Hyperthermia (HT)—in combination with chemotherapy [2,3] or radiation [4–6]—has been shown to be an effective therapeutic modality for cancer treatment. A significant improvement in tumor control and overall survival was observed with the combined therapy in comparison to the stand-alone therapy for high risk soft tissue sarcomas [2,7]. Radio frequency (RF) is commonly used to induce mild HT in tumors [8], and high intensity focused ultrasound (HIFU) is currently under development as well [9].

To reduce side effects and to improve the therapy provided by chemotherapy, mild HT combined with thermosensitive liposomes (TSL) as nano-carrier systems has been the subject research for decades. Studies have demonstrated that HT can be used to trigger drug release from nano-carriers containing chemotherapeutics such as doxorubicin and higher drug concentrations in tumors can be achieved. As RF and HIFU are proven methods used to heat controlled volumes, it is possible to combine these technologies with the TSL nano-carriers to achieve a triggered local release of chemotherapeutic drugs into the tumor tissue upon externally-controlled heating [10]. Lysolipid-based TSL with encapsulated doxorubicin (DOX) have been developed and have recently entered human clinical trials [11].

The mechanism of TSL nanocarrier action is their HT-induced ultra-fast intravascular DOX release inside of the heated tumor vasculature, which significantly increases the concentration of bioavailable drug in the interstitial space compared to conventional PEGylated liposomes or free drugs [12]. Alternative targeting concepts for TSL include a pre-HT treatment to increase their extravasation by the enhanced permeability retention (EPR) effect [13,14], combined with a second heat trigger to increase interstitial drug release [15]. In recent years, an improved TSL formulation for intravascular drug release based on the synthetic phospholipid 1,2-dipalmitoyl-*sn*-glycero-3-phosphodiglycerol ($DPPG_2$) has been developed [16–20] and is currently under preclinical investigation in a feline phase I

study. Hence, the control of temperature in the target volume is vital to optimal targeting and triggering, parallel to the development of new nano-carriers, and there is a need for better therapy control for HT in combination with drug-loaded TSL.

Temperature monitoring and control over the entire volume is necessary in order to avoid HT-induced necrosis and cell death and thus achieve an optimal therapeutic outcome in order to sufficiently heat up the whole volume of interest in a controlled manner. Different methods such as temperature probes can be used for these purposes, but probe based methods only provide one- or two-dimensional locally confined temperature information. In contrast, magnetic resonance imaging (MRI) provides different noninvasive methods for temperature mapping during mild HT, and was thus developed by several study groups [21–26].

For effective radiation therapy, precise and uniform dose coverage of the target volume is crucial [27]. An analogous drug dose painting is therefore an advancement towards personalized chemotherapy and more accurate predictions about the likely treatment response. In addition to invasive methods of drug quantification such as biopsy, histology, or micro dialysis, some non-invasive methods for drug dose painting—SPECT, CT, PET, and MRI—are examined in several studies [28–31]. All of these methods present their own advantages and disadvantages in areas such as the spatial and temporal resolution, quantitative measurement, and covered volume. CT scans, for example, demand ionizing radiation, but provide a high spatial and temporal resolution. SPECT and PET provide quantitative data for radio-labelled pharmaceuticals, but require radioisotopes with generally short half-lives and yields only limited spatial resolution. MRI, however, combines high spatial and temporal resolution with no requirement for ionizing radiation and a good sensitivity for common CAs.

In the first part, this work investigates the effectiveness of mild HT-induced drug release from TSL in small animals with subcutaneous implanted syngeneic tumors by juxtaposing widely applied methods such as water baths or a cold light lamp with a newly developed MR-compatible laser light-based device (Chapter 3).

In the second part,, different static and dynamic MR parameters are examined using the new device, and their potential to serve as a surrogate marker for drug dose painting during mild HT-induced drug release from TSL is evaluated (Chapter 4). As temperature is the trigger for drug release from TSL, 3D information of temperature distribution or local drug concentration is suggested as the next area of improvement in further research in order to provide a more effective therapy.

2. BASICS

2.1 CHEMOTHERAPY WITH DOXORUBICIN

Chemotherapy is a method of treating cancer with cytotoxic drugs, which can be naturally or synthetically produced. There are more than 50 drugs used, alone or in combination, to treat more than 100 types of cancer [32]. Systemic chemotherapy is accompanied by systemic side effects that limit the usable dosage. For experiments with cytotoxic drugs in this work, the drug Doxorubicin (DOX) was used.

Doxorubicin is an anthracycline antibiotic used for systemic treatment. It works by intercalating DNA and RNA, thereby causing an inhibition of type II toboisomerase, disturbance in DNA synthesis, and an increase in radicals. This affects DNA and membrane damage, crosslinks, and oxidative stress, among other effects [33]. DOX is used in the treatment of cancers such as mamma carcinoma, soft tissue sarcoma, and osteosarcoma. Common side effects of the treatment include hair loss, nausea, vomiting, myelosuppression, and cardio toxicity [34]. Therefore, the therapy would be improved by a targeted release of DOX to reduce side effects.

DOX is also useful for the development of new therapy strategies due to its fluorescence and rapid intercalation with DNA. These properties can assist with analysis of tissue concentration.

2.2 HYPERTHERMIA

To understand the benefits of mild hyperthermia and distinguish it among other heat therapies, this section begins with a short introduction. Hyperthermia (HT) in cancer therapy is defined as a treatment in which body tissue is exposed to temperatures between 39 to 42 °C for a period of time (usually 60 min). This approach causes less significant changes in the treated tissue compared to major tissue change induced by coagulation or ablation. Regional or local HT must also be distinguished from whole-body HT, which involves body temperatures around 39°C and is not restricted to a single organ or part of the body. Likewise, thermoablation is distinguished as a treatment where temperatures above 60 °C are administered to a small tissue volume.

Heating of a target area can be accomplished using a number of techniques. In a clinical setup, regional deep HT with radio frequency field is common. Radio frequency transmitters located in specific areas around the body are used to heat up the tissue in the target area.

At a normal body temperature of 37 °C, permeability in the blood vessels of tumorous tissue manifests itself differently than permeability in healthy tissue. Heating of the tumor causes an increase of perfusion and permeability of blood vessels, even in normally impermeable tumor vessels [11]. For tumor therapy—in particular for use in drug enhancement within tumor tissue—perfusion and the permeability of blood vessels are crucial. These factors can be meaningfully influenced by HT [8,35]. In induced mild HT, direct tumor cell death is not the therapeutic goal as the tissue temperatures do not rise high enough to achieve coagulation necrosis. The main objective of mild HT, aside from the potential immune effects, is its synergistic effect with chemotherapy or radiation therapy [36]. For this, a constant temperature in the range of 39 °C to 42 °C for a minimum of one hour is necessary. This induces positive effects such as inhibition of DNA-repair caused through chemotherapy or radiotherapy, changes in perfusion and oxygenation of tumor tissue, change in the extracellular pH, liberation of heat shock proteins and stimulation of the immune system [37]. Due to these effects, HT is approved as a standard treatment modality in combination with chemotherapy within a multimodal treatment strategy for high risk soft tissue sarcoma [38]. It must be noted that mild HT has to be used in combination with radiotherapy or chemotherapy to prompt a significantly better therapy outcome over chemotherapy or radiotherapy alone [2].

2.3 LIPOSOMES

Due to the cytotoxic drugs' lack of tumor specificity and severe short-term side effects of chemotherapy, new strategies such as the use of liposomes as drug carrier are urgently needed for a better therapy outcome. Liposomes as nanocarrier are capable of incorporating drugs inside their aqueous interior, or to integrating drugs into their membranes. They were described first by Bangham et al. 1965 [39] and have been improved for tumor treatment since the late 70s . The lipids used in this work were developed by Eibl et al. [40]. The next section briefly introduces the release kinetics and effect of liposomes.

Liposomes are synthetically-produced vesicles consisting of a phospholipid bilayer membrane surrounding an aqueous interior. These membranes are biocompatible and the phospholipids can be enzymatically metabolized mainly in the liver [41]. The phospholipids themselves are composed of hydrophobic tails and hydrophilic head groups (Figure 1).

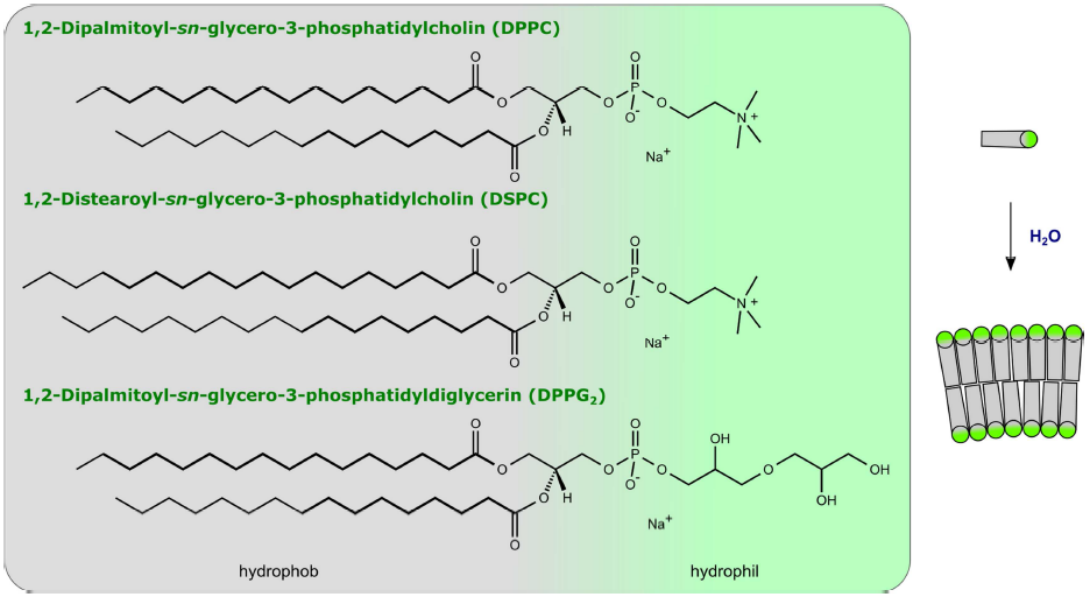

Figure 1: Chemical structure of the used phospholipids DPPC, DSPC, and $DPPG_2$ and illustration of the lamellar structure after mixing in aqueous solution.

In the clinic, the main representative of a liposomal chemotherapy using doxorubicin is Caelyx/Doxil (Janssen Pharmaceutica NV, Bersee, Belgium, or LP, Horsham, USA). Caelyx/Doxil belongs to the group of non-TSL with long circulating times and thereby takes advantage of the enhanced permeability and retention (EPR) effect. Despite potential passive accumulation in tumor tissue, these drugs have not exhibited improved antitumor efficacy due to a generally weak EPR-effect in solid human tumors and a strong liposomal membrane disabling DOX leakage. However, there is a reduction of cardiotoxicity with these liposomes [42]. Thermodox (Celsion Corporation, Lawrenceville, USA) instead is a thermosensitive liposome (TSL), which facilitates release of the encapsulated drug at temperatures higher than 39°C. Such a mechanism promotes a higher drug concentration in heated tissue, and thus fewer side effects and a better therapy outcome. There are ongoing clinical studies regarding this method, which is based on lysolipids [11]. The disadvantage of TSL based on lysolipids is their shorter circulation time at normal body temperature. As a result, fewer liposomes reach the target tissue, reducing the effectiveness of the therapy.

Thermosensitive functionality of liposomes is driven by the phase transition of the lipids, which was first described by Yatvin et al. in 1978 [43]. The phase transition can be induced by heating the lipids above their specific phase transition temperature, T_m. beneath T_m, the liposome membrane is in a solid-gel phase, thus the densely-packed lipids prevent a diffusion of water or drugs through the membrane. Above the phase transition temperature, lipids enter into a liquid-crystalline phase, which alters the structure of the membrane until diffusion of macromolecules can occur.

This phase transition is specific for each phospholipid type (Table 1), thus the phase transition temperature of the liposomes can be defined by mixing different lipids.

The liposomes employed in this work are TSLs based on the novel synthetic phosphatidyldiglycerol (DPPG2) that lacks lysolipids. Elimination of lysolipids results in a longer circulation time at body temperature and a rapid drug release at T_m (chapter 3.2.1), which are mandatory for effective drug delivery by TSL.

Lipid	hydrophobic tail	hydrophile head group	Tm [°C]
DPPC	palmitic acid	phosphocholine	41.5
DSPC	stearic acid	phosphocholine	56.0
DPPG2	palmitic acid	phosphodiglycerin	39.7

Table 1: Different phospholipids with their phase transition temperatures T_m

2.4 BIOMEDICAL OPTICS

The effect of light on biological tissue has been leveraged in medical therapy and diagnostics for a long time. From an optical point of view, tissue is a complex medium due to its inhomogeneous microscopic and macroscopic scale [44]. Therefore, the effects on tissue are dependent on the wavelength, light power, irradiation time, and tissue attributes such as reflection, scattering, absorption, polarization, and fluorescence. This section provides a short introduction to biomedical optics and its application in medicine in order to inform later discussion about a suitable laser system for mild HT with a high penetration depth in biological tissue. A high penetration depth is necessary to obtain an as homogenous heating pattern as possible. For further information, the author also refers to Jelinkova et al. 2013 [45].

2.4.1 INTERACTION OF LASER RADIATION WITH TISSUE

Penetration depth of light into tissue depends mainly on three factors: reflection, scattering and absorption [45].

Reflection

Reflection determines the amount of radiation that penetrates into the tissue. This effect plays an important role for transparent tissue; however for opaque tissue, reflection has only a minor influence and scattering and absorption are more dominant [45].

Scattering

Scattering occurs when the radiation is forced to deviate from its straight trajectory. Scattering emits the light in all directions around the scattering center and is not limited by a

given direction. Release of energy in the tissue is dependent on factors such as the wavelength, light polarization, and the size of the molecule [45].

Absorption

For therapeutic treatment, the medium's ability to absorb electromagnetic radiation is important. Absorption of electromagnetic radiation depends on factors such as: the electronic structure of the atoms and molecules, radiation wavelength, and the thickness of the medium. In biological tissue, absorption is mainly caused by water molecules, although macromolecules, e.g. proteins and pigments, also play a role [45].

2.4.2 LASER LIGHT FOR MEDICAL APPLICATIONS

Lasers are mostly used for three forms of treatment in medicine: laser surgery, thermal therapy, and photodynamic therapy. The application of a laser is defined by its wavelength and pulse modulation.

Absorption of optical radiation in water is highest in the ultra violet (UV) (100 nm - 380 nm) and long wave infrared ranges (IR). Biological tissue usually contains a great deal of water, thus the short wave and long wave radiation is absorbed easily. For visible light and near IR, hemoglobin and melanin determine absorption, as demonstrated in Figure 2 [46].

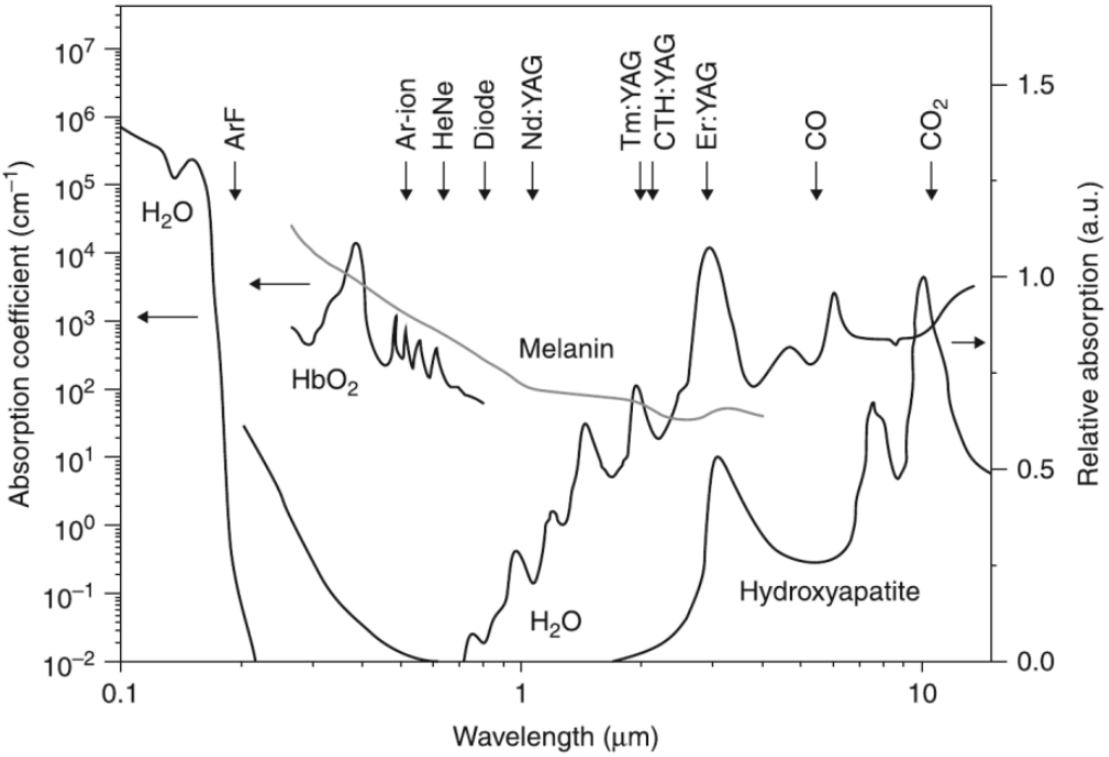

Figure 2: Absorption of optical radiation depending on wavelength for different constituents of tissue. Typical wavelength for different laser types are marked with arrows and corresponding laser medium. (from [45] with permission by Elsevier GmbH)

The nature and severity of the tissue reaction depend mainly on the irradiation time and intensity (Figure 3). Therefore, photochemical reactions would be triggered by a long irradiation time (several minutes or hours) in the range of less than one Watt per square centimeter (cm^2). For radiation in the visible- or infrared-light range, molecules can absorb radiation and release their energy in the surrounding tissue. This can lead to an increased presence of free radicals (this effect can be enhanced by a photosensitizer i.e. for photodynamic therapy (PDT)), which harm genetic material (DNA) and oxygen proteins. Light radiation in the UV range can also cause direct damage to DNA.

For short irradiation times (few seconds to milliseconds) and a power of a few Watts per cm^2 up to one Megawatt, different thermal effects are observed. These effects range from a slight warming of the tissue or denaturation of protein, to charring and black staining of the tissue. Such thermal effects are harnessed therapeutically for laser surgery or laser-induced thermotherapy (LITT). With short irradiation times of nano- to microseconds and an irradiation power of megawatts per cm^2, the target tissue vaporizes, while the surrounding tissue is barely warmed.

Even higher power—in the order of Gigawatts per cm^2 in tissue—creates plasma. This creates a shock wave that spreads out and destroys tissue mechanically. This is the basis for disruption of kidney- or gallstones (lithotripsy).

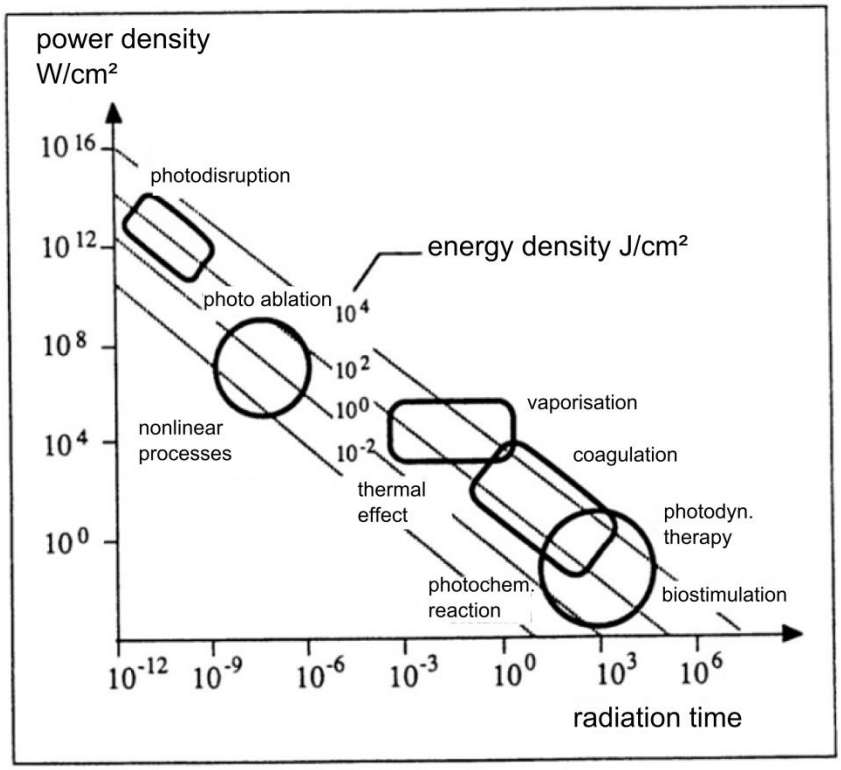

Figure 3: Dependency of light effects on tissue in relation to radiation time and power of applied light (adapted from Berlien [47,48])

In biological tissue, absorption is weak in the near-infrared (NIR) range, which is defined as 600 nm – 1350 nm wavelengths [49]. For the NIR window, a free path of about 0.1mm can be assumed between photon-scattering events. This free path results in an absorption length from 10 mm – 100 mm [50]. For subcutaneous mild HT, a wavelength in the NIR window is necessary.

2.5 MR-IMAGING

Nuclear Magnetic Resonance (NMR) was discovered by Bloch and Purcell in 1946 and is based on different energy levels in an atom nucleus [51,52]. MRI uses this effect to resolve the distribution and relaxation properties of hydrogen atoms. This chapter only provides an overview of MRI, principles of tissue quantification, and temperature mapping—all of which were used for the following experiments. For further information, the reader is referred to books by Haacke and Bernstein [53,54].

2.5.1 NUCLEAR SPIN AND NET MAGNETIZATION

The properties of an atomic nucleus are described, among other things, by the number of protons Z and the mass number *N,* as well as its nuclear spin quantum number *I*, which can be either zero, a half-integer, or an integer. For the hydrogen nucleus ^{1}H, which is used

mostly in clinical MRI, the spin quantum number is $I = ½$. For all nucleuses with a spin quantum number nonequal to zero, the magnetic moment μ can be written with:

$$\vec{\mu} = \gamma \vec{I}$$

1

where γ is the gyromagnetic ratio, which is characteristic for a specific nucleus. The hydrogen nucleus has a gyromagnetic ratio γ at $2.675*10^8$ rad T^{-1} s^{-1}.

Within a large external magnetic field (B_0), nuclear spins "align" with the external magnetic field. This behavior can be described by

$$\frac{d\vec{\mu}}{dt} = \gamma \vec{\mu} \times \vec{B}$$

2

This equation implies that a given magnetic moment (spin) will precess around the axis of the B_0 field, with the field strength B and with the Larmor frequency $\omega_0 = \gamma B$. The sum of all magnetic moments generated from the nuclei in a sample is called the net magnetization (M_z). In absence of an external field, the net magnetization vanishes because the direction of these magnetic moments is randomly distributed in a sample. Within an external magnetic field, nuclear spins align either parallel (P↑) or antiparallel (P↓) to the external field, resulting in a net magnetization in the direction of B_0 that can be described with [55]:

$$M_z = \frac{\hbar\gamma}{2}(P_\uparrow - P_\downarrow) \approx \frac{\hbar^2 \gamma^2 B_0}{4kT}$$

3

were ħ denotes the reduced Planck constant and k for the Boltzmann constant. This approximation is valid when $kT > \gamma \hbar B_0$. For a typical MRI setting i.e. a magnetic field of 1.5T and room temperature, the polarization of the spins is 10^{-6} [55]. This shows that strong magnetic fields are required to yield a measurable magnetization in a sample. Given that the hydrogen nucleus has the highest γ of all stable nuclei ($\gamma = 2.675 * 10^8 \frac{\text{rad}}{\text{Ts}}$), and the percentage of water is high (~ 70 %) in the human body, the hydrogen nucleus is mainly used for clinical MR-imaging.

2.5.2 RADIOFREQUENCY EXCITATION

With a radiofrequency (RF) pulse $B_1(t)$ the net magnetization M_z can be tipped out of their state of equilibrium. Assuming that $B_1(t)$ rotates around the magnetic field $\overrightarrow{B_0} = B_0 * \hat{z}$ with a frequency ω_p the RF pulse can be written as [53]:

$$B_1(t) = B_1\left(\hat{x}\cos(\omega_p) + \hat{y}\sin(\omega_p)\right)$$

4

Now the resulting magnetization in a constant magnetic field B_0 can be described with

$$\frac{dM(t)}{dt} = \gamma * M(t) \times \left(B_0 + B_1(t)\right)$$

$$= \gamma * M(t) \times \left(B_1\cos(\omega_p t)\hat{x} + B_1\sin(\omega_p t)\,\hat{y} + B_0\hat{z}\right)$$

5

To simplify the equation, this system is transformed from a stationary coordinate system into a rotating coordinate system with $x' = x\cos(\omega_p t) + y\sin(\omega_p t)$; $y' = -x\sin(\omega_p t) + y\cos(\omega_p t)$; and $z' = z$, which results in

$$\frac{dM(t)}{dt} = \gamma * M(t) \times \left(B_1\widehat{x'} + \left(B_0 - \frac{\omega_p}{\gamma}\right)\widehat{z'}\right)$$

6

Thus, the magnetization rotates in the rotating system around the axis of the effective magnetic field B_{eff}. If ω_p is equal to the Larmor frequency, only the x'-component of B_{eff} remains and the magnetization can be written as

$$\frac{dM(t)}{dt} = \gamma * M(t) \times B_1\widehat{x'}$$

7

If a field on-resonance B_1 is applied for a finite time t_p, the net magnetization can be tipped by an angle α with

$$\alpha = \gamma B_1 t_p$$

8

After switching of the RF pulse, the resulting magnetization $M_\perp$ induces a signal in a receiver coil, which is the signal detected in NMR-measurements.

2.5.3 RELAXATION

Interactions between spins lead to a statistically-changing local magnetic field that changes the magnetization relaxation of the spin. This relaxation is characterized by the longitudinal relaxation time T_1 and the transversal relaxation time T_2. [53]

The *longitudinal* or *spin-lattice* relaxation time T_1 characterizes the restoration of the longitudinal component of the magnetization M_z. This relaxation is induced by a spin-lattice interaction and the surrounding tissue absorbs the released energy.

The *transversal* or *spin-spin* relaxation time T_2 is characterized by the decay of the transverse magnetization. Here, the coherent transverse magnetization that exists after a RF pulse is destroyed by an interaction between the spins. This destruction leads to a loss of phase coherence between the different spins. Furthermore, every spin is exposed to a fluctuating field, which varies the magnetic fields in M_z direction and hence the precession rate and thus the phase of the spins. This relaxation process is an entropic effect, and there is no energy exchange with the environment.

Due to magnetic field inhomogeneity, there is a faster decay of the MR-Signal due to the spin-spin relaxation. Static variations in B_0 lead to an additional phase, which is called the T_2* relaxation. In contrast to the T_2-relaxation, the T_2*-relaxation can be reversed by inverting the phase. The resulting decay of the transverse magnetization is described by the T_2* relaxation time and can be written as:

$$\frac{1}{T_2^*} = \frac{1}{T_2} + \frac{1}{T_2'}$$

9

Longitudinal (T_1) and transversal relaxation times (T_2, T_2*) depend on e.g. different tissue types and the magnetic field strength B_0. Typical T_1 and T_2 relaxation times for tissue are shown in Table 2.

Tissue	T_1 relaxation time				T2 relaxation time			
	1.5 T		3 T		1.5 T		3 T	
muscle	1130	± 91.7	1420	± 38.1	35.3	± 3.85	31.7	± 1.9
cartilage	1060	± 155	1240	± 107	42.1	± 7.05	36.9	± 3.81
synovial fluid	2850	± 279	3620	± 320	1210	± 140	767	± 48.8
subcutaneous fat	288	± 8.42	371	± 7.94	165	± 5.5	133	± 4.43

Table 2: T_1 and T_2 relaxation times for 1.5 T and 3.0 T with SD in different tissue [56]

These relaxation effects are descripted by Bloch 1946 with equation 10 [51].

$$\frac{dM_x}{dt} = \gamma\left(\vec{M} \times \vec{B}\right)_x - \frac{M_x}{T_2}$$
$$\frac{dM_y}{dt} = \gamma(M \times B)_y - \frac{M_y}{T_2}$$
$$\frac{dM_z}{dt} = \gamma(M \times B)_z - \frac{M_0 - M_z}{T_1}$$

10

With the introduction of the complex transversal magnetization $M_\perp = M_x + iM_y$ and a constant magnetic field B = (0,0,B_0)$^\perp$ this equation can be simplified to

$$M_\perp(t) = M_\perp(0)e^{-i\omega_0 t}e^{-\frac{t}{T_2}}$$

$$M_z(t) = M_0 - \big(M_0 - M_z(0)\big)e^{-\frac{t}{T_1}}$$

11

This is called the free induction decay (FID). After an RF pulse, the transversal magnetization precesses around the B_0 axis with the Larmor frequency, and decays with $e^{-\frac{t}{T_2}}$ whereas the longitudinal magnetization recovers with $1 - e^{-\frac{t}{T_1}}$.

2.5.4 Spatial Encoding and k-Space

For MR-imaging, this NMR-signal needs to be modified to provide a spatial encoding. Here a short introduction is given about the spatial encoding and the resulting k-space.

Spatial encoding

In a homogeneous magnetic field, all spins have the same Larmor frequency ω_0, and the NMR-signal after an RF pulse contains no information about the position of the spins. Therefore, spatial encoding is essential for MR-Imaging, which relies on applying magnetic field gradients. The first step in approaching the problem is to reduce the dimension of the volume of excitation by applying a slice selection. A two-dimensional slice in one direction is selected and yields to a two-dimensional matrix that must be resolved. Slice encoding in the x-y plane is achieved by applying a linear magnetic gradient G_z in the z-direction, which leads to a location-dependent Larmor frequency in the z-direction, and a simultaneous excitation RF pulse with the frequency ω_a and bandwidth $\omega_{(z)}$.

$$\omega_z = \gamma(B_0 + G_z)$$

12

The properties of the gradient and the RF pulse bandwidth $\omega_{(z)}$ determine the position and the thickness of the excited slice, which is illustrated in Figure 4.

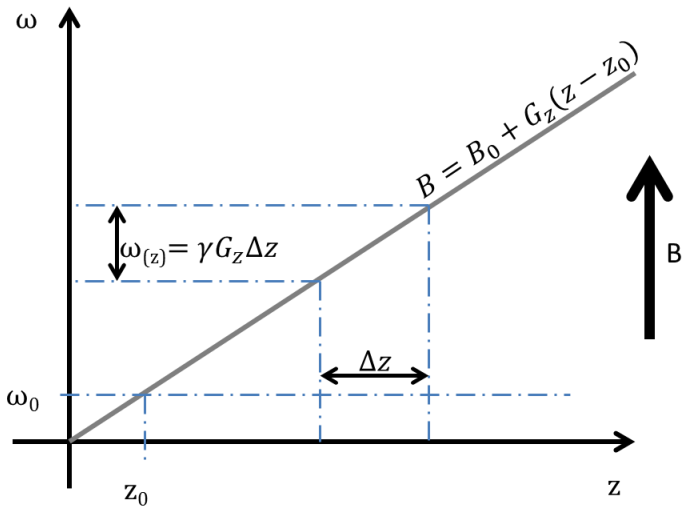

Figure 4: Principle of slice selection. For a defined Gradient G_z and an RF pulse with a bandwidth $\omega_{(z)}$, a slice with thickness Δz is excited.

For in-plane encoding, two further gradients are necessary: the frequency and the phase-encoding gradient. A signal with a high bandwidth is generated by adding a linear gradient $G_{(x)}$ during the readout. With a Fourier transformation, every frequency can be assigned to a specific place in the direction of the gradient. Determining the remaining dimensions requires that a phase-encoding gradient $G_{(y)}$ be added after the RF pulse, and before readout. To satisfy the criterion of Nyquist, this cycle is repeated with an incrementally altered gradient for phase-encoding until enough data is received to calculate the image with the target spatial resolution in phase direction.

k-space

The acquired signals create the so-called “k-space”. With these data, the image can be reconstructed by Fast-Fourier transformation. Each point in the k-space corresponds with one spatial frequency in the whole image. Low spatial frequencies are found in the center of k-space and high spatial frequencies correspond to peripheral points in k-space.

The acquisition of the k-space is controlled by the strength of the gradients. Thus with varying gradients different sampling grids can be acquired (Figure 5). The position (k_x k_y k_z) of data points in this grid defines the strength of the gradients. Here an acquisition with Cartesian coordinate system will be used. A schematic diagram for k-space filling is shown in Figure 5.

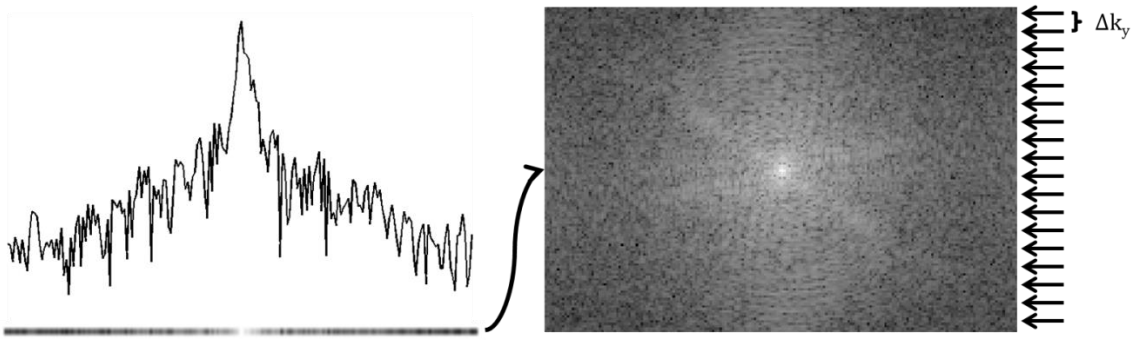

Figure 5: The Signal modified with gradients is sampled with a given frequency and resulting magnitude is transferred into the k-space. Position in k_y-direction is set by the phase-encoding gradient, position in k_x is modified by frequency encoding gradient during signal readout.

2.5.5 SEQUENCES

Every sequence in MR-imaging consists of essential components such as an RF excitation pulse, gradients for spatial encoding, and signal readout combined with an echo type (spin echo, gradient echo, …). There are different sequence types with different advantages and limitations.

SpinEcho sequence

The spin echo (SE) sequence is the most basic sequence and was developed by Carr and Purcell 1954 [57]. The principle of the spin echo sequence is described in Figure 6 . A 90° RF pulse with a 180° pulse is combined. With this technique, the T_2* effect can be reversed using the 180-degree refocusing pulse. It flips the magnetization by a 180° pulse at TE/2 after excitation were TE is the echo time, which induces a revocation of phase difference between spins. This leads to an echo after TE. After a defined repetition time TR, this sequence cycle is repeated until k-space is completely acquired.

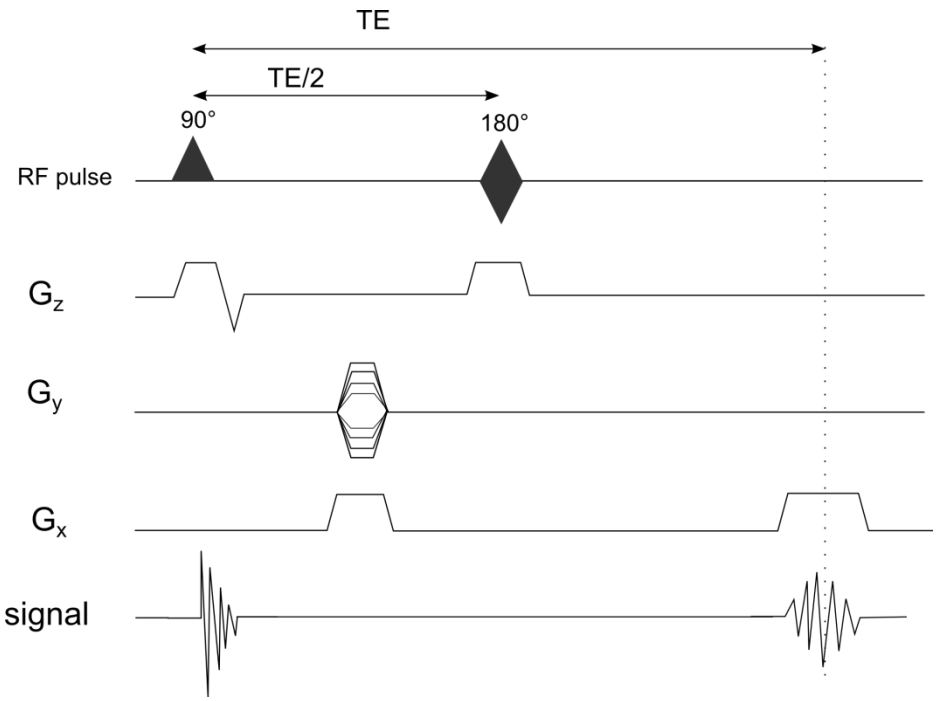

Figure 6: Schematic of a spin echo sequence with RF pulse, gradients, and generated spin echo. This schema is repeated after TR.

Gradient Echo sequence

Gradient echo (GRE) is a class of pulse sequences that was developed primarily for rapid scanning; it is widely used in dynamic 3D volume imaging [58]. In contrast to the spin echo sequence, the echo is generated with a negative gradient, which is applied after the initial RF pulse and without a 180° RF rephrasing pulse. The flip angle is usually below 90°. After the pulse, a positive gradient is applied, rephasing the net magnetization. Here the echo is not compensating for dephasing caused by static field inhomogeneities or transversal relaxation. Therefore, the decay of the echo is T_2* dependent [59]. The benefit of this sequence is its faster acquisition time, which can be realized due to the lower FA, resulting in a possibly shorter T_R. One limitation is that for this sequence, there is always a T_2* effect despite T_1 weighted sequence parameters.

2.5.6 TISSUE CONTRASTS

Simply by varying the sequence parameters, different image contrasts—which represent the tissue specific properties—can be generated. Notably, these contrasts provide qualitative information about the tissue.

Proton density weighted image: High signal intensity represents a high proportion of water protons in the corresponding volume. For this contrast, relaxation times should have only a minimal influence on the image contrast. This is achieved with a spin echo sequence with short TE and a long TR.

T_1-weighted image: This contrast is mainly based on the different longitudinal relaxation times of biological tissue, where high signal intensity stands for a short T_1 time. This is achieved with a short TE and short TR.

T_2-weighted image: This contrast is dominated by the transversal relaxation times of biological tissue. High signal intensity in the image results from a long T_2-time. This is achieved with a long TE and a long TR.

2.5.7 T_1 QUANTIFICATION

For some applications, qualitative information from T_1 weighted images is not sufficient and a T_1 quantification is necessary. In this work, the T_1 quantification was based on a variable flip angle method [53].

Variable flip angle

A method for T_1 determination is the variable flip angle (VFA) method. This method is based on the FLASH signal equation[58]:

$$S = S_0 * \sin(\alpha) * \frac{1-E_1}{1-\cos(\alpha)*E_1} * E_2$$

13

Where $E_1 = \exp(-T_R/T_1)$ and $E_2 = \exp(-T_E/T_2^*)$. For T_1 determination, typically two or more FA α are used in a range between 2° and 30° [60]. Measuring the signal amplitude for at least two different flip angles, the T_1 relaxation time can be calculated with equation 13. For applications requiring a high temporal resolution, the acquisition time can be accelerated by combining a baseline acquisition with two flip angles, which is followed by repeated measurements with only one flip angle. This method was introduced by Brookes et al. in 1996 [61], and was improved by Dietrich et al. [62] with multiple flip angles serving as the baseline for calculating S_0. With S_{dyn}, the single flip angle α_{dyn}, and the known S_0 from the baseline measurement, the value for T_1 can be determined with:

$$E_{1,dyn} = \frac{S_0 E_2 \sin(\alpha_{dyn}) - S_{dyn}}{S_0 E_2 \sin(\alpha_{dyn}) - S_{dyn}\cos(\alpha_{dyn})}$$

$$\approx \frac{S_0 \sin(\alpha_{dyn}) - S_{dyn}}{S_0 \sin(\alpha_{dyn}) - S_{dyn}\cos(\alpha_{dyn})}$$

14

The resulting approximation is based on neglecting the T_2* dependence.

For the dynamic measurement from time-resolved data, contrast-enhanced MRI usually employs 2D or 3D sequences with a spoiled gradient echo readout. The use of 3D acquisition provides different benefits compared to a 2D measurement. For example, with a 3D acquisition, coverage of a whole volume is possible without slice spacing.

2.5.8 NON-INVASIVE TEMPERATURE MEASUREMENT

Non-invasive temperature measurement by MRI is a tool that controls mild HT in biological tissue. There are numerous parameters in MR-Imaging that are temperature-sensitive. Temperature-sensitive parameters include: magnetization M_0, T_1-relaxation time, T_2-relaxation time, diffusion, and proton resonance frequency. Only the T_1-relaxation time and the proton frequency allow a sufficient acquisition time, a good signal to noise ratio, and a good spatial resolution during MR-Imaging [63].

T_1-relaxation temperature dependency

Bloembergen et al. demonstrated the temperature dependence of the T_1-relaxation time in 1948 [64], and in 1984, this dependence was investigated for non-invasive thermometry in MRI[65]. As described in chapter 2.5.3, spin-lattice relaxation in biological tissues results from dipolar interactions of macromolecules and water molecules, which appear from their relative movement to each other. These motions are temperature-dependent, and are thus reflected in changes in the spin-lattice relaxation time T_1 [66]. The variation of the T_1 relaxation time of water protons can be described with [67]:

$$\boldsymbol{T_1} \propto \boldsymbol{e^{-E_\alpha/kT}}$$

15

where E_α is the activation energy for self-diffusion of water, k is the Boltzmann constant, and T is the absolute temperature. From the change in the spin-spin-lattice relaxation and the temperature change, a linear relationship can be assumed for small physiological temperature changes [63]:

$$\boldsymbol{T_1(T) = T_1(T_{ref}) + m * (T - T_{ref})}$$

16

where T_{ref} is the reference temperature and T the absolute temperature. The dependency $m = dT_1/dT$ must be empirically determined for every tissue. At an initial approximation, a 1%/°C T_1-change can be expected [63]. This approximation is not valid for large temperature changes and tissue modification, which occur during, for example, coagulation or other pathological tissue changes.

It is also possible to calculate the temperature change with the T_1 weighted signal change caused by the T_1-change. For this method, the change in the M_0 must be determined or neglected, which yields greater inaccuracies and is not commonly used for quantitative temperature mapping [63].

Temperature-induced frequency shift

After Fourier transformation (chapter 2.5.4) of the MRI-signal, there are three kinds of data sets reconstructed from the raw data: real data, the magnitude data, and the phase data. This phase information can be used to calculate a temperature change between two different time points. That temperature dependency of the proton resonance frequency shift was first observed by Hindman [68] and was implemented for MRI temperature-mapping by De Poorter et al. [69,70].

Among other factors, the lamor frequency of a nucleus is determined by the local magnetic field, expressed by [63]:

$$\boldsymbol{\omega = \gamma B_0 (1 - s)}$$

17

where *s* is the shielding constant. This shielding constant, which differs with the chemical compound, is used e. g. in MR-spectroscopy. Furthermore, this shielding constant is temperature-dependent. The ^{1}H-nucleus is shielded by electrons. For Water (H_2O) the electrons are bound in hydrogen bonds. This yields a smaller shielding compared to the ^{1}H-nucleus. An increase in temperature leads to a destabilization of the hydrogen bonds, therefore the electrons are less “tied” in these bonds. This ensures better shielding of the ^{1}H-nucleus and a decrease in the Larmor frequency. Frequency changes cause a phase difference in the acquired signal (Figure 7),

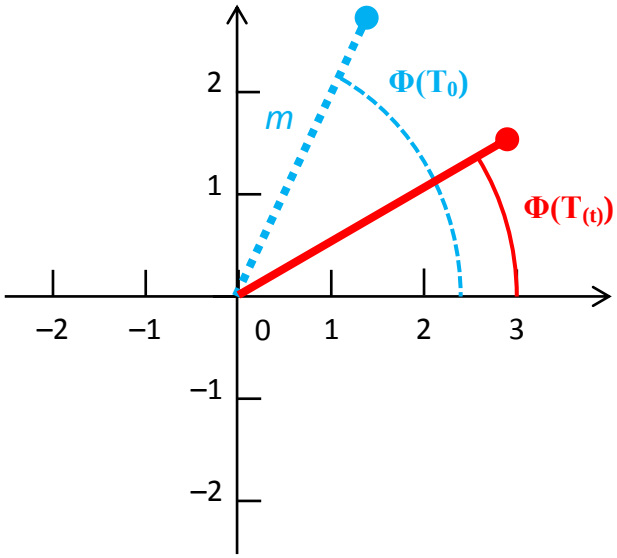

Figure 7: Phase value Φ for temperature baseline measurement T_0 (blue/ dotted line) and follow up measurement $T_{(t)}$ (red/ continuous line).

which can be used to calculate temperature change with:

$$\Delta T_{(t)} = \frac{\phi(T_{(t)}) - \phi(T_0)}{\gamma \alpha B_0 TE} \quad (18)$$

where γ is the gyromagnetic ratio (42.567 MHz/T for ^{1}H [53]), α is the PRF change coefficient (-0.01 ppm/°C), B_0 is the magnetic field strength and TE is the echo time [63].

2.5.9 Dynamic Contrast-Enhanced MR-Imaging

Medical application of MR-Imaging can be enhanced by the application of contrast agents (CA). In the context of MR-Imaging, the CA is not directly visible; instead, the effect of the contrast agent on the relaxation of surrounding nuclear spins is observable. The CA influences the relaxation times T_1, T_2 and T_2* in its direct environment. Different tissues are affected differently depending on the magnetic properties of the contrast agents. The image contrast can be changed with CA to provide additional information about the tissue. For clinical use, contrast agents are most commonly based on gadolinium (Gd), which shortens the T_1 relaxation time. This results in increased signal intensity in a T_1-weighted image. Gadolinium-based contrast agents reduce beside T_1 also the T_2 relaxation times. In T_1-weighted scans, change of T_2 relaxation time is only visible at high Gd concentrations of several mM [71,72]. Dynamic contrast-enhanced MR-Imaging is used to determine ancillary information about the examined tissue, such as hemodynamic parameters.

The Fundamental effect of CA-TSL

Encapsulating contrast agents in TSL alters signal performance in comparison to free CA. The CA-TSL used in this study has a low r_1 as long as the CA is encapsulated in the TSL at temperatures below T_m. This condition is due to the limitation in water exchange through the membrane resulting in a limitation of the dipolar relaxation process [73]. Limiting the dipolar relaxation process then results in little T_1 variation in the presence of the TSL, and a low signal change in a T_1-weighted image. After heating up the liposomes, the membranes of the TSL becomes more permeable to water at T_m, and the water exchange through the membrane increases until the CA is released above T_m. CA release results in a decrease of T_1 and a signal increase; as the temperature initially increases, these effects are instigated by water exchange. At yet higher temperatures, the CA is released as described in figure 8.

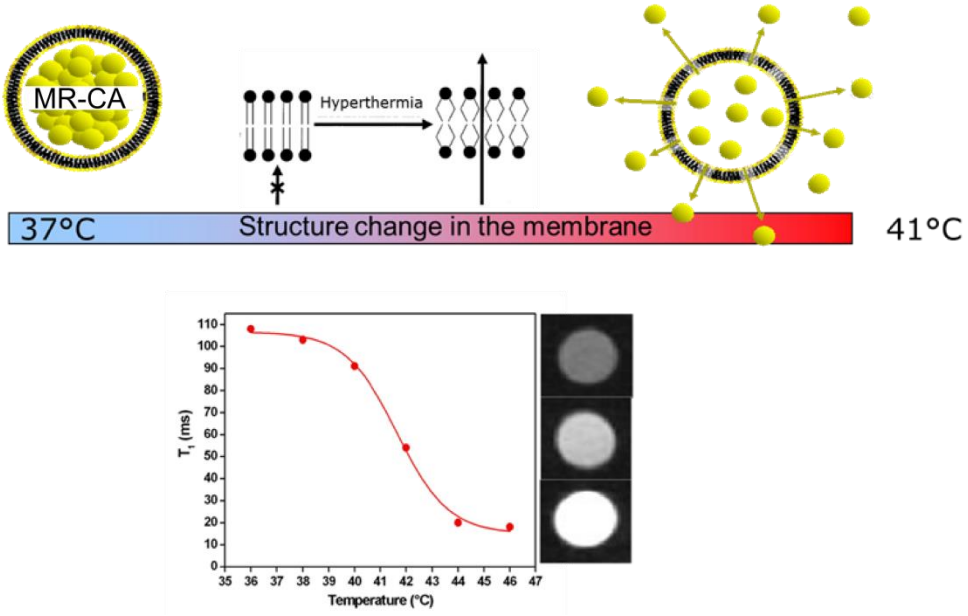

Figure 8: Principle of T_1 and signal change for CA-TSL in water during temperature increase.

3. COMPARISON AND VALIDATION OF HEATING METHODS

Markedly diverse localized heating methods have been applied in preclinical animal studies for various drug delivery systems and related studies. This diversity prevents proper comparison of experimental results, such as homogeneity of the heating and the effectiveness of drug uptake in the tumor that these parameters warrant due to their role in the therapeutic response. Heating methods can be non-invasive—such as water bath heating [74–77], electric heating coils [14,78], heating lamps [20,79–81], laser light [82], focused ultrasound [83–85], and radio frequency [30]—or as invasive as a heat pipe through the tumor [26].

To investigate mild HT in combination with TSL in a small animal model, a newly developed MRI-compatible laser light applicator was built and compared to previously popular methods for inducing mild HT in experimental setups. The laser light applicator was also tested in order to validate its use in the MRI study in the second part of the thesis.

In this study described in chapter 3, the characteristics and the comparability of three different methods for mild HT for subcutaneous tumors in small animal models were investigated. Mild HT was applied to a subcutaneous syngeneic rat tumor using either a water bath, a cold light lamp, or an infrared laser. In light of the rising popularity of MRI-guided treatments, the laser applicator was built to be MRI-compatible, and was then compared to the other heating methods.

The new method may therefore offer a more local heat application than the regional heating achievable with water baths, in the context of MRI and CA-TSL [74,86]. The new method is also easier to implement in an MRI birdcage coil than a water bath or a heating lamp.

In this work, the effectiveness of mild HT-induced drug release from TSL in small animals with subcutaneous implanted syngeneic tumors was investigated with different preclinical HT methods. Therefore, widely applied HT methods such as cold light lamp and water bath were characterized and compared to HT-induced by a newly developed MR-compatible laser-based device.

Parts of this section (Chapter 3) are also published in the Journal Of Controlled Release by Willerding et al. [87].

3.1 EXPERIMENTAL SETUP

The comparability of temperature homogeneity and the effectiveness of drug uptake in combination with TSL in the tumor were examined. A water bath, a cold light lamp, and a newly developed infrared laser light applicator were used for heating. To assess the heating methods in different tumor volumes, two separate groups of tumor volumes ($0.5\ cm^3 < V < 1.0\ cm^3$ and $2.0\ cm^3 < V < 3.0\ cm^3$) were investigated.

Different parameters were investigated: heat distribution and drug concentration in the heated tumor, and drug concentration in the unheated tumor. Furthermore, a pharmacokinetic (PK) study was performed. Data were analyzed with statistics software (SPSS Statistics V22, IBM, Germany).

After reaching the expected tumor size, experiments were carried out in accordance with the protocols described further on.

Tumor-bearing rats were assigned randomly to one of the three heating methods and one of the two tumor size groups. This results in six different groups, each with three animals. After one tumor reached the target tumor size, this tumor was defined as the "heated tumor". Minimum tumor size for both tumors was $0.1\ cm^3$. Both of the tumors were shaved, and the tumor probes were implanted as described below (chapter 3.2.3).

For water bath heating, the leg of the heated tumor was wrapped in plastic foil to prevent swelling of the skin caused by warm water. For lamp heating, the surrounding skin of the tumor was protected with cotton wool. Due to the Gaussian distribution of optical power in the laser beam as described above (chapter 3.2.4), the laser light beam was adjusted 10 mm larger in diameter than the tumor.

After animal preparation, the heating began. DOX-TSL (2 mg/kg) were injected after minimum target temperature – 40 °C – was reached in each of the temperature probes. 60 min after injection the heating device was turned off—or the leg was taken out of the water bath—and the tumor was cooled down immediately with a cooling pack. For PK, capillary blood (200 µl) was taken before heating, 2 min and 60 min after injection with a heparin-coated tube (Microvette 200, Sarstedt AG & Co., Nürnbrecht, Germany); the sample was centrifuged and frozen until HPLC DOX measurement. After letting the tumor cool down to normal temperature, the rats were euthanatized during deep inhalation anesthesia by injection of pentobarbital.

For drug uptake analysis in tumor tissue, the heated tumor was removed and bisected parallel to the body axis. The unheated tumor was removed completely. To exclude possi-

ble influence of the heating mattress on the PK and the drug uptake in the tumor, for every heating device, one muscle tissue sample from the abdominal wall was taken.

3.2 METHODS

3.2.1 PREPARATION OF LIPOSOMES

Lipid composition of all TSL formulations was DPPC/DSPC/$DPPG_2$ 50/20/30 (mol/mol) ($DPPG_2$-TSL). TSL encapsulating either 300 mM citrate pH 4.0 or 250 mM Gd-DTPA-BMA, pH 7.4 were prepared according to the lipid film hydration and extrusion method described in detail by Hossann et al. in 2010 and 2013 [18,88]. DOX was actively loaded to the citrate containing liposomes [18].

All preparations were performed as aforementioned [17,18,88]. In brief, the hydrodynamic diameter (z average) size intensity distribution plot and zeta potential were measured by DLS (Zetasizer Nano ZS, Malvern Instruments, Worcestershire, United Kingdom). The instrument was calibrated with a size standard (Nanosphere™, 125 nm, Thermo Fisher Scientific, Waltham, MA, USA). Phospholipid composition and shelf life was measured with thin layer chromatography (TLC). TLC plates were developed with chloroform/methanol/acetic acid (97.5%)/water 100:60:10:5 (vol/vol) to separately detect phosphatidylcholines (DPPC, DSPC), $DPPG_2$, and their decomposition products (Lyso-PC, Lyso-PG_2). A lipid standard containing DPPC, $DPPG_2$, and lyso-phosphatidylcholine was applied in every TLC run to check the separation quality. Phospholipid concentration was quantified by a phosphate assay using a 1 g/l phosphate solution (Merck KGaA, Darmstadt, Germany) as reference standard. DOX concentration was measured by fluorescence spectroscopy (Varian Cary Eclipse) after disruption of the liposomes with Triton X-100. Commercially available non-thermosensitive PEGylated liposomal DOX (Caelyx®, Jannsen-Cilag GmbH, Neuss, Germany) and non-liposomal DOX (Adriplastin®, Pharmacia GmbH, Karlsruhe, Germany) were used as reference standards. The concentration of gadodiamide was quantified by inductively-coupled plasma atomic emission spectroscopy (ICP-AES) using a gadolinium ICP standard solution (Merck KGaA, Darmstadt, Germany) as reference standard. The thermosensitivity of each preparation was shown in vitro by measuring the temperature-dependent release profile of DOX and gadodiamide with fluorescence spectroscopy (Cary Eclipse, Varian Inc., Palo Alto, CA, USA) and a 0.47 T NMR-analyzer (Minispec NMS120, Bruker BioSpin GmbH, Rheinstetten, Germany), respectively. The liposomes had a phase transition temperature (T_m) of 40 °C. The characterization of DOX liposomes is given in supplementary table 1, 2.

For the comparison and validation of heating methods, only DOX-TSL were used. CA-TSL were used for therapy monitoring in later experiments (chapter 4).

3.2.2 *ANIMAL MODEL*

For animal experiments, the syngeneic BN175 cell line was used (kindly provided by Timo ten Hagen, Erasmus MF, Rotterdam). Cells were grown in RPMI 1640 medium (Biochrom AG, Berlin, Germany) supplemented with 10 % fetal calf serum (FCS) (vol/vol), 100 U/ml penicillin and 100 µg/ml streptomycin, respectively. Cells were cultured at 37°C in a humidified atmosphere of 95 % air and 5 % CO_2.

Experiments were performed in accordance with approved protocols (Regierung von Oberbayern, CaNo. 55.22.1.54-2532.3-21-11). The experiments were performed under anesthesia (isofluran 2-5 % and oxygen 1.5 l/min) administered with an isofluran evaporator (Vapor 19.3, Dräger, Germany). For Tumor growth $1.5x10^6$ / 50 µl BN175 cells were injected in both hind legs. Tumor growth was recorded in three plains (length = a; width = b; height = c) by caliper measurements. The volume was calculated using an ellipsoid approximation (Equation 19). Tumor growth was measured every second day.

$$V = \frac{\pi}{6} * a * b * c$$

19

Injection of tumor cells was used, because for tumors with a volume larger than 2 cm^3 and the rapid tumor growth a re-opening of the lesion from an implantation cannot be excluded.

3.2.3 *TEMPERATURE MEASUREMENTS*

Temperature was measured with a temperature data-logger (K204, Voltcraft, Germany). To assess an overview of the temperature distribution in the tumor, three temperature probes were implanted in the tumor at a pre-defined depth. For accurate insertion of the temperature probes, three cannulas (20G needle, BD Microlance™, Germany) were implanted parallel to the body axis, and were removed after insertion of the probes. Specific depths were assigned by scale paper to ensure an approximated depth of 2-3 mm for the lateral, 5-6 mm for the central, and 7-10 mm for the medial probe. To assess the accurate depth of every tumor probe, photographs were taken with scale paper prior to removal of the cannulas. The distance to the skin was measured with an image post-processing program (GIMP 2.8, open source). Measurements were performed twice, on two different

photographs from different angles to reduce errors. The procedure of measurement is shown in Figure 9.

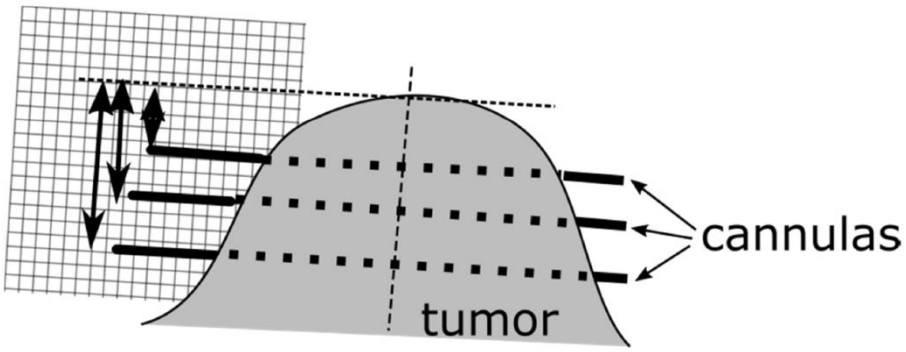

Figure 9: Procedure of measurements for probe depth, drawn lines marked the estimated position of the probe [87].

From the temperature data, the equivalent time at 43 °C ($CEM_{43\,°C}$) was calculated with equation 20 [89]:

$$CEM_{43°C} = \sum_{t=0}^{t=final} R^{(43-\bar{T})}\Delta t \qquad \textbf{20}$$

where $\overline{T}$ is the average temperature during time Δt. For temperatures above 43°C R = 0.5 and for temperatures below 43°C R = 0.25. $CEM_{43°C}$ considers varying temperatures in tissue – time-temperature relationship – and determines the equivalent heating time at 43 °C to attain a comparable effect on the tissue. $CEM_{43°C}$ was calculated as mean value for each temperature probe. Furthermore, the temperature exceeded by 10 %, 50 %, and 90 % of the measurement points were determined (T_{10}, T_{50}, T_{90}). This temperature representation is less influenced by outliers and is commonly used in clinical HT.

3.2.4 LASER LIGHT APPLICATOR

For adequate local heating of the tumor in the MRI, a novel non-invasive HT applicator was needed. The engineering drawings were created with a computer-aided design (CAD) program (Solid Works ST5, Siemens Industry Software GmbH & Co. KG, Germany) and are presented in the supplement chapter 6.2.3.

Requirements

Requirements for the applicator were as follows: the applicator should be able to locally heat up a subcutaneous tumor with a size up to 2,5 cm^3 homogenously. It must induce a minimal tumor temperature level of 40 °C and a maximum temperature of 44 °C. In addi-

tion, it must be MRI-compatible and –save. This means that must be no artifacts induced by the applicator, and no use of para-, ferromagnetic or electric conductive materials. It should fit into the lateral part of a dedicated wrist coil, beside the animal. Thus, it must have a maximum dimension of 35 mm in diameter. Because of the open design of the wrist coil, a maximum length was not given. Laser light should induce heating and source power had to be controllable from outside of the RF cabin. The heated volume should be adjustable to tumor size. In case of a defect or a change in requirements, all components of the applicator should be exchangeable.

Implementation

As power source, a 940 nm laser (Medilas D940, Dornier MedTech, Germany) was available. This wavelength in the NIR promises a high penetration depth of the light. The laser light was guided to the applicator with a glass fiber (10 m, 600 µm). The laser beam was adjusted using two lenses: one convex lens (focal length 5 mm) used as collimator and one concave lens (-10 mm) for beam expansion. A deflecting prism (25 mm Fused Silica Right Angle Prism Al & AR Coated, Edmund Optics GmbH, Germany) was used to significantly reduce the overall height of the applicator to fit into the wrist coil. An aluminized coated hypotenuse ensured a total reflection of the laser beam and protected the prism surface against damage during handling. The beam diameter was adjustable by controlling the distance between lens system and prism (Figure 10).

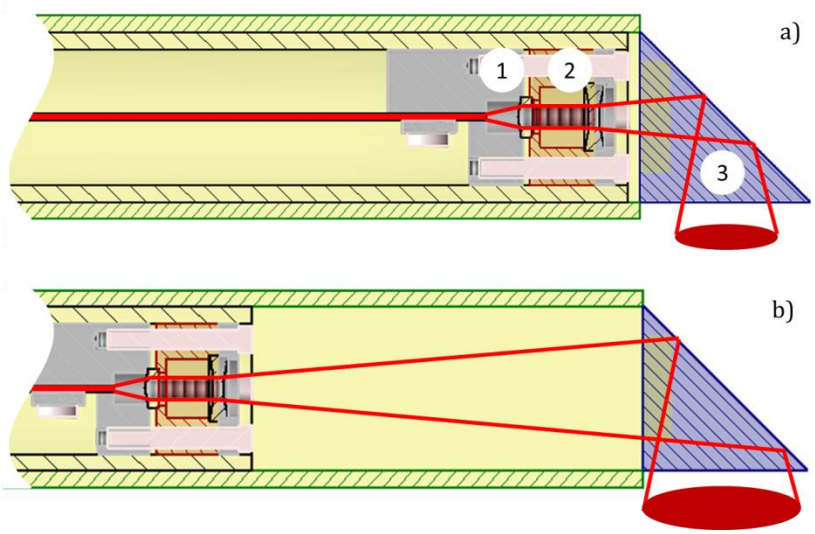

Figure 10: Half section of HT applicator with beam path (red lines) for a) small or b) large beam; ① convex lens; ② concave lens; ③ deflecting prism; green → outer tube; black→ inner tube.

The applicator consisted of six elements, which were divided into two assemblies, the housing and the lens system. The housing was made from two tubes. The outer tube (OT) held the prism and the inner tube (IT) held the second assembly. To guarantee the movability of the tubes against each other, an interference fit (d_{h9}^{H8}) was used. A slot in the OT

and a thread in the IT were made to secure the tube against rotation and to fix the lens system inside the IT with a screw, while allowing a shift of 60 mm in the axial direction. Lenses were installed in the second assembly, which consisted of three parts: the main part that fixed the glass fiber and the collimation lens; the middle part, which defines the distance between the collimation and concave lenses; and the cover that fixes the concave lens and the middle part to the main part. To guarantee MR-safety and compatibility, the housing and mount for the lenses were composed of plastics (Polyethylene). To facilitate replacement of single parts of the applicator, all joints were fixed with nylon screws. The prism was attached with a double-sided adhesive tape so the prism can be removed when necessary. Details and exact dimension are presented in the engineering drawings (chapter 6.2.3).

Laser power must be manipulated manually either with laser power itself, or by modulating the laser beam with on and off time periods. Laser power could be set to 1 W – 60 W (Watt) in steps of 1 W while the applicator could handle 10 W. The laser could be modulated with an increment of 0.01 s (0.01 s < t < 0.1 s) and an increment of 0.1 s (t > 0.1 s).

Preliminary tests revealed an insufficient heating of the base of the tumor along with a high temperature on the surface of the tumor with continuous wave heating (CW). Therefore, all following experiments were performed using a rectangle-shaped modulated laser power with: on time 0.05 s – 0.50 s; off time 0.05 s – 0.50 s.

For following experiments, the intensity of a TEM_{00} laser beam is described most closely by a Gaussian distribution [90]:

$$I(r) = I_0 * e^{\frac{-2r^2}{w^2}}$$

21

Where I_0 is the maximum intensity on the optical axis, r is the distance from this axis. Beam width is described as w, where the laser beam has $1/e^2$ of the maximum intensity I_0. Thus w of the laser beam had to be ~ 1.3 times of the tumor diameter to provide ~ 40 % of I_0 to the outer rim of the tumor.

3.2.5 WATER BATH

Many study groups use a temperature controlled water bath for mild HT optional with thermosensitive liposomes [74,85]. Therefore, a water bath was used as a reference method for comparison with the new laser applicator.

Requirements

Like the laser light applicator, the water bath had to be able to regionally, homogenously heat a subcutaneous tumor with a size of up to 2,5 cm^3. It also had to induce a tumor temperature of minimum 40 °C, with a maximum temperature of 44 °C. The rat body needed to be protected from the heat of the water bath. Water temperature had to be controllable in a range from 39 °C to 46 °C.

Implementation

A water bath served as a heating source and water reservoir (JB Aqua 26L, Gran Instruments, United Kingdom). The temperature was manually controllable and the temperature was measured with a temperature probe (temperature data-logger, Voltcraft K204; temperature probe GTF 101; ATP Messtechnik GmbH, Germany). The rat was separated from water with a plastic plate (PMMA, Polymethylmethacrylate) and insulated from the heat by a polystyrene sheet (20 cm x 20cm x 1 cm). Both the plastic plate and the polystyrene sheet had holes for submersion of the tumor-bearing leg into the water bath. For this setup, a plastic foil was applied around the heated leg to prevent swelling of the skin due to the warm water. The setup is shown in Figure 11. For the experiment, water was warmed up to 42°C before the tumor bearing leg was inserted into the water. Temperature was controlled either by raising the temperature or by cooling with cold water.

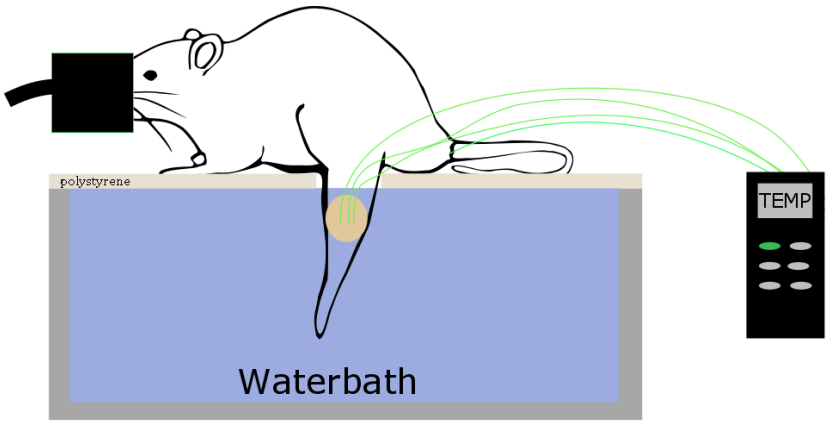

Figure 11: Illustration of experimental setup for water bath hyperthermia with polystyrene sheet and thermometer.

3.2.6 LAMP

In previous experiments [20], a cold light lamp was used to induce local HT in a subcutaneous tumor model. To facilitate comparability between the laser light applicator and the lamp, experiments were repeated under the same experimental setup as the laser light experiments.

Requirements

Like the laser light applicator, the lamp should be able to locally heat up a subcutaneous tumor with a size up to 2.5 cm^3 homogenously. It also had to induce a tumor temperature of minimum 40 °C and with a maximum temperature of 44 °C.

Implementation

To induce local mild HT a cold light lamp (Optich PL 2000, Photonic Optische Geräte GmbH & Co. KG, Austria) was used. The lamp had one light source with two fiberglass gooseneck lights. To prevent the goosenecks from overheating, an infrared absorption filter (Supplementary figure 1) was applied, resulting in a light spectrum, which is not optimal for a high penetration depth. The light power was controlled manually by a rotary knob.

Figure 12: Experimental setup for mild HT with cold light lamp, heating mattress and thermometer.

3.2.7 DOX Quantification in Pharmacokinetic studies

Concentrations of DOX of plasma and tissue samples were quantified with high performance liquid chromatography (HPLC). Prior to analysis, the analyte was extracted from samples through a modified liquid extraction protocol [91].

Plasma samples (50 µl) were diluted to 1 ml using phosphate-buffered saline. 100 µl internal standard (daunorubicin, 10 µg/ml) and 10 ml dichloromethane / isopropyl alcohol 9:1 (vol/vol) were added to each sample. Subsequently, the sample was vigorously mixed and centrifuged, and the organic phase was transferred to a fresh tube. Under a steady stream of nitrogen at 40 °C, the extract was freed from the solvent. The sediment was dis-

solved in 1 ml 80 mM potassium dihydrogenphosphate / acetonitrile 73:27 (vol/vol) and transferred to HPLC injection tubes after centrifugation.

Tissue samples (100 mg) were added to 1.5 ml methanol / water 2:1 (vol/vol) and 100 µl internal standard in 2 ml Eppendorf tubes. Homogenization was performed with tungsten carbide beads in a TissueLyser (Qiagen GmbH, Hilden, Germany) at 30 Hz for 5 min. To each sample, 200 µl silver nitrate 33% (weight/volume) was added and the sample was subsequently incubated for 10 min on ice to release DOX from its binding to DNA [92]. The samples were transferred to 10 ml centrifuge tubes and 5 ml chloroform / isopropyl alcohol 2:1 (vol/vol) was added. After vigorous mixing and centrifugation, the organic phase was transferred to a fresh tube, freed from solvent, and processed as described above for plasma samples.

Samples were measured with a Waters HPLC system (515 HPLC pump, 717plus autosampler, 470 fluorescence detector). Fluorescence detection was performed with an excitation wavelength of 480 nm and an emission wavelength of 560 nm. The runs were carried out on a C18 column (250 mm x 4.6 mm internal diameter, 5 µm particle size; 125 Å pore size) from Phenomenex Ltd., Germany. 50 µl per sample was injected and eluted with an isocratic flow of 1 ml/min using 80 mM potassium dihydrogenphosphate / acetonitrile 73:27 (vol/vol) as mobile phase. Adriblastin® was used as reference standard.

3.2.8 STATISTICAL ANALYSIS

Statistical analysis was performed using SPSS V22 (IBM, Germany). For correlation analysis, the concept of bivariate correlation according to Pearson was used [93]. Differences between two data sets were tested using two-tailed students t-test. P-values were considered to be (highly) significant if they were less than or equal to 0.05 (0.01).

3.3 RESULTS

18 animals were treated successfully. HPLC analysis was performed on 54 tumor samples, 3 muscle samples and 54 plasma samples for DOX-quantification. Red skin was observed in 5 animals (2x using the lamp with small tumor, 1 x laser large tumors, 1 x laser small tumors).

3.3.1 TUMOR SIZE AND POSITION OF TEMPERATURE PROBES

The median size of the tumors was 1.0 $cm^{3,}$ with a standard deviation of 0.1 cm^3 for small tumors and 2.2 cm^3 ± 0.2 cm^3 for larger tumors. The reference tumors had a median vol-

ume of 1.2 cm^3 ± 0.8 cm^3 (mean ± SD) across all experiments. The average depths of the temperature probes were 8.6 mm ± 1.4 mm for the medial, 5.6 mm ± 1.1 mm for the central, and 2.8 mm ± 0.7 mm for the lateral probe. The weight ratio between the lateral and medial tumor parts for all experiments was 1.02 ± 0.52.

3.3.2 TEMPERATURE DISTRIBUTION

In all experiments, the requested minimum mean temperature of 40°C was achieved for all three temperature probes in all treatment groups. The highest temperature was always measured in the lateral part of the tumor, decreasing with increasing tissue depth independent of the heating method. The highest temperature for a single animal (44.3 °C) was achieved with the laser light applicator in the lateral part of the larger tumors, decreasing to 40.0 °C in the medial part. For visualization, all temperature values are plotted in Figure 13.

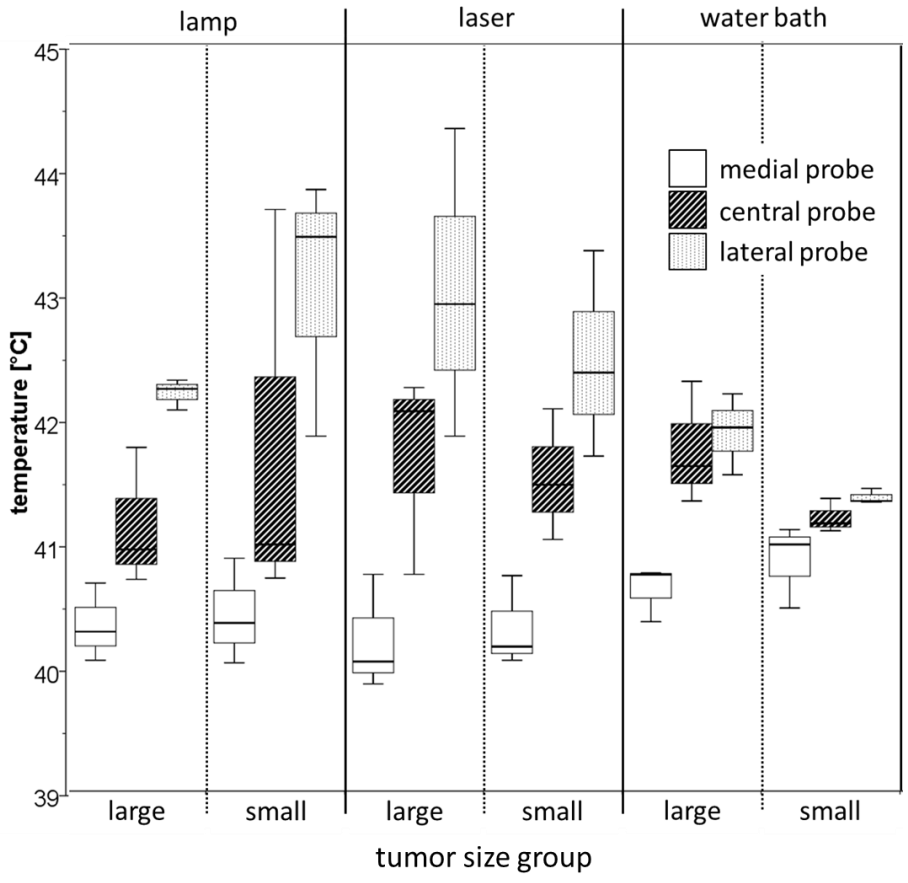

Figure 13: Boxplot of the temperature values for all experiments and temperature probes differentiated between heating method and smaller (1.0 ± 0.1 cm^3) or larger tumor volumes (2.2 ± 0.2 cm^3).

For each heating experiment, temperature data from the three probes were used to assess the temperature gradient inside the tumor (Table 3). The lowest temperature gradient was found during the water bath heating, with -0.1 °C/mm in the small tumor

and -0.2 °C/mm in the large tumor. The highest temperature gradient in the small tumors was recorded while using the lamp, and the laser resulted in the highest temperature gradient of the large tumors (-0.3 °C/mm). For the water bath and the laser, temperature gradients were steeper in the larger tumors, whereas in the lamp experiments, the mean gradient was steeper for smaller tumors (Table 3).

Method	Tumor size	Temperature gradient [°C/mm]	SD [°C/mm]
Lamp	large	0.25	±0.11
	small	0.54	±0.33
Laser	large	0.47	±0.34
	small	0.48	±0.29
Water bath	large	0.20	±0.07
	small	0.10	±0.11

Table 3: Temperature gradients with standard deviation for the different experimental groups.

The efficacy of heating was investigated by calculating T_{10}, T_{50}, T_{90} and $CEM_{43°C}$ (Table 4). The highest T_{10} of 44.4°C for a single experiment was obtained in a large tumor heated by the laser. The smallest T90 of 39.9 °C was achieved in a small tumor with the lamp.

Heating method	Tumor size	T_{90} [°C]	T_{50} [°C]	T_{10} [°C]	$CEM_{43°C}$ [min]
Lamp	small	40.2 ± 0.4	41.7 ± 1.4	43.3 ± 1.2	36.4 ± 34.0
	large	40.2 ± 0.2	41.0 ± 0.5	42.4 ± 0.0	10.5 ± 0.7
Laser	small	40.3 ± 0.4	41.5 ± 0.6	42.6 ± 0.9	16.4 ± 13.5
	large	40.1 ± 0.2	41.7 ± 0.7	43.1 ± 1.2	29.5 ± 26.5
Water bath	small	40.6 ± 0.2	41.2 ± 0.2	41.6 ± 0.1	5.2 ± 0.6
	large	40.6 ± 0.3	41.7 ± 0.4	42.1 ± 0.4	9.9 ± 5.2

Table 4: T_{90}, T_{50}, T_{10} and $CEM_{43°C}$ data for the whole tumor with standard deviation for every experimental group.

$CEM_{43°C}$ was calculated with equation 20 for every temperature probe, and results are displayed with corresponding tissue damage signs in table 5. For a single probe, the highest value reached was 152 $CEM_{43°C}$, from a laser experiment with a large tumor. Over 80 $CEM_{43°C}$ were reached in three experiments: two lamp experiments with a small tumor and one laser experiment with a large tumor. Four animals exhibited redness of the skin above the heated tumor after mild HT. These animals had a $CEM_{43°C}$ of 83.4 min, 115.8 min, 152.0 min and 77.0 min measured in the lateral tumor probe.

Heating	Tumor size	Animal no.	Tumor volume (cm³)	Tumor DOX concentration [ng/mg]	Equivalent minutes for 43 °C ($CEM_{43°C}$) medial (min)	central (min)	lateral (min)	Mean (min)
Lamp	large	N20	2.0	14.2	1.4	2.6	26.2	10.1 ± 14.0
		N23	2.2	13.5	1.1	3.7	25.3	10.0 ± 13.3
		V33	2.4	18.7	2.6	12.3	19.1	11.3 ± 8.3
	small	V23	0.8	23.3	1.0	3.9	83.4	29.5 ± 46.8
		V36	1.0	22.6	3.2	2.6	13.2	6.3 ± 6.0
		V37	1.0	23.4	1.7	102.3	115.8	73.3 ± 62.4
Laser	large	N44	2.1	7.0	2.9	2.8	13.3	6.3 ± 6.0
		V27	2.2	6.1	0.9	22.5	152.0	58.4 ± 81.8
		V39	2.1	18.0	1.0	16.2	53.5	23.8 ± 26.9
	small	N47	1.0	23.3	1.0	16.7	77.0	31.5 ± 40.1
		V21	0.9	19.7	2.6	3.9	10.0	5.5 ± 4.0
		V29	1.0	14.8	1.2	7.7	27.2	12.0 ± 13.4
water bath	large	V26	2.1	4.5	2.9	23.5	20.8	15.7 ± 11.2
		V32	2.7	4.8	1.6	9.2	14.3	8.3 ± 6.4
		V35	2.1	4.3	2.7	6.1	8.2	5.7 ± 2.8
	small	V24	1.0	6.1	4.8	5.1	6.4	5.4 ± 0.8
		V28	0.9	9.3	4.4	6.3	6.1	5.6 ± 1.1
		V38	0.9	24.5	1.9	4.5	7.0	4.5 ± 2.6

Table 5: $CEM_{43°C}$ for every experiment and temperature probe. Grey shaded areas imply animals with red skin after therapy caused by heating.

3.3.3 DRUG DISTRIBUTION

The mean DOX concentration in the three not-heated muscle tissue samples was 0.5 ± 0.1 ng/mg. The mean DOX concentration in the reference tumor averaged over all experiments was 1.2 ± 0.4 ng/mg. For the large treated tumors the DOX concentration in the reference tumor was 1.0 ± 0.3 ng/mg and for the small treated tumors it was 1.4 ± 0.4 ng/mg ($p < 0.05$). The highest DOX concentration (23.1 ± 0.4 ng/mg) was found in the animals with small tumors heated by lamp. The lowest DOX concentration was found in the tumors heated with the water bath (4.5 ± 0.3 ng/mg). Independently of the heating method, the DOX concentration was higher in smaller tumors compared to larger tumors. Concentration ratio in the heated tumor was 4 times up to 17 times the DOX concentration of the not-heated tumor dependent on the heating method (Table 6). All measured and calculated drug concentrations are shown in supplementary table 3.

		Tumor with HT (ng/mg) ± SD			T. without HT (ng/mg)	DOX ratio	
HT	Size	Lateral part	Medial part	Mean		lateral /medial	with/ without HT
Lamp	small	24.2 (± 0.9)	22.0 (± 1.3)	23.1 (± 0.4)	1.4 (± 0.5)	1.1	17
	large	23.4 (± 4.6)	7.9 (± 6.4)	15.4 (± 2.8)	1.0 (± 0.3)	3.0	15
Laser	small	24.4 (± 6.4)	12.8 (± 1.7)	19.3 (± 4.2)	1.3 (± 0.5)	1.9	15
	large	11.5 (± 9.8)	9.2 (± 4.8)	10.4 (± 6.6)	0.8 (± 0.2)	1.3	13
Water bath	small	11.8 (± 8.1)	14.5 (± 10.9)	13.3 (± 9.9)	1.4 (± 0.4)	0.8	10
	large	4.1 (± 1.2)	5.2 (± 0.5)	4.5 (± 0.3)	1.1 (± 0.5)	0.8	4

Table 6: Mean and standard deviation of DOX concentrations for the two tumor parts and their weighted sum of the tumors exposed to HT in comparison to the reference tumors not exposed to HT. For comparison, ratios of DOX concentration were calculated in the heated tumor comparing lateral and medial tumor parts or tumor exposed with and without HT.

The DOX concentration in the lateral and medial tumor sections of the heated tumors were evaluated in relation to the applied heating method (Figure 14) and relative to the total tumor size. The smallest concentration ratio between the medial and the lateral tumor part was found for the water bath heating with 0.8 for the small and large tumors, respectively. For the laser heating the drug ratios were 1.8 and 1.5, whereas for the lamp heating the ratios were 1.1 and 2.7, respectively.

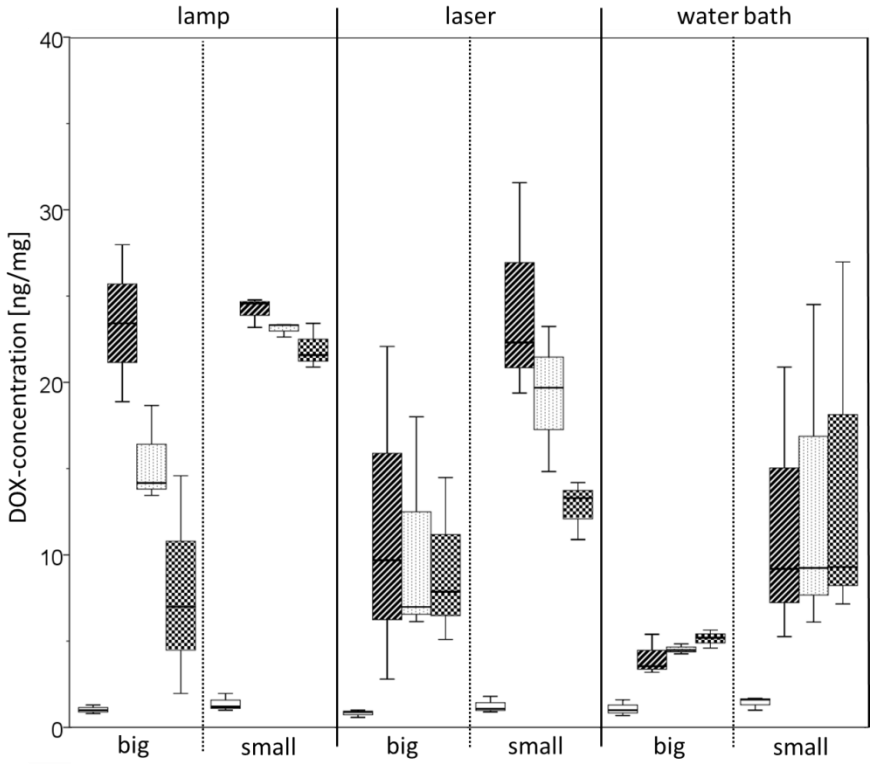

Figure 14: Boxplot for the DOX concentration for different tumor parts: The reference tumor (blank), lateral (hatched), the whole tumor (dotted) and the medial tumor (checker) part for all experiments

There was no significant correlation ($p > 0.05$) between the medial temperature, central temperature, lateral temperature, T_{90}, T_{50}, T_{10} and $CEM_{43°C}$ compared to the DOX concentration in the lateral tumor half, the medial tumor half or the whole tumor for all experiments (Table 7).

	medial temperature [°C]	central temperature [°C]	lateral temperature [°C]	mean temperature [°C]	T_{90} [°C]	T_{50} [°C]	T_{10} [°C]
lateral tumor tissue [ng/mg]	-0.311 (c)	0.017	0.241	0.083	-0.416	0.007	0.235
	0.209 (p)	0.948	0.336	0.742	0.086	0.980	0.347
medial tumor tissue [ng/mg]	-0.121 (c)	0.137	0.207	0.186	-0.176	0.105	0.211
	0.633 (p)	0.587	0.409	0.460	0.486	0.680	0.401
Whole tumor [ng/mg]	-0.286 (c)	0.069	0.269	0.140	-0.351	0.047	0.262
	0.250 (p)	0.787	0.280	0.578	0.153	0.852	0.293

Table 7: Correlation (c) between temperature [°C] and DOX concentration [ng/mg] with their corresponding p-values (p)

3.3.4 PHARMACOKINETICS

Plasma DOX concentration for all groups at 2 min after injection was 32.0 ± 10.0 ng/mg and decreased significantly ($p < 0.01$) to 7.7 ± 5.2 ng/mg after 60 min.

The lowest DOX concentration after 60 min was found 1.9 ± 1.0 ng/mg for the water bath with the large tumor. The highest DOX concentration of HT was found for the laser experiments in small tumors with 12.5 ± 2.6 ng/mg (Figure 15).

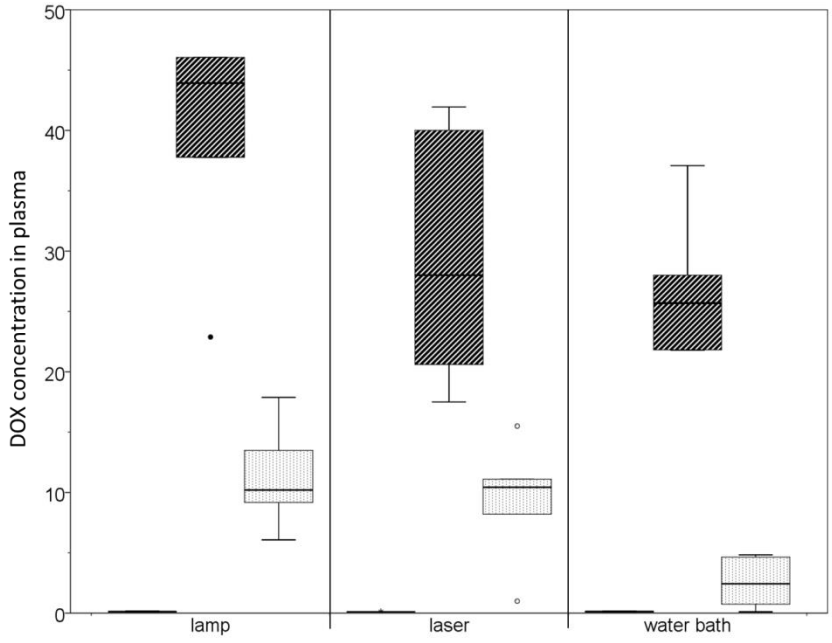

Figure 15: DOX concentration in plasma for all time points in ng/mg: pre-injection (blank), 2 min (hatched) and 60 min (dotted)

To compensate for the differences in the manner of injection, the 60 min values were normalized on 2 min plasma concentration value. The water bath heating groups demonstrated the highest decrease in DOX concentration compared to the other heating methods. The concentration dropped to 8.3 % ± 0.1 % and 12.4 % ± 10.5 % for animals with large and small tumors, respectively. For the lamp experiments, there were residual concentrations of 38.7 % and 24.7 %. For the laser experiment, 29.0 % and 39.6 % was measured for large and small tumors, respectively.

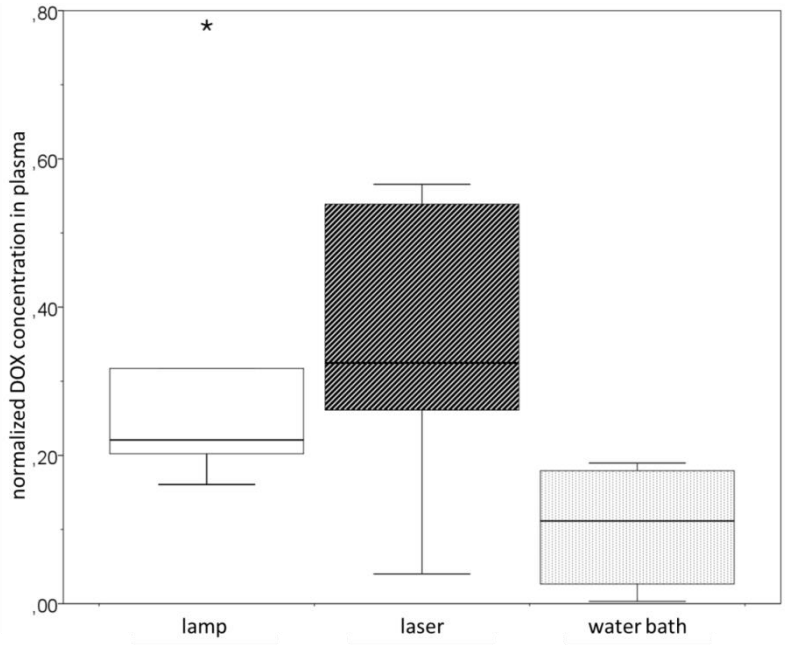

Figure 16: Normalized DOX concentration in plasma after 60 min of treatment.

The differences in normalized DOX concentration were significant between the lamp and the water bath ($p = 0.05$) and between the laser and water bath experiments ($p = 0.02$). In contrast, the difference between the laser and lamp heating method was not significant ($p = 0.84$).

In terms of the different tumor sizes, there were no significant differences ($p > 0.05$) between the groups due to the small group sizes. However, there was a tendency for higher plasma DOX concentration within the small tumors (Fig. 17)

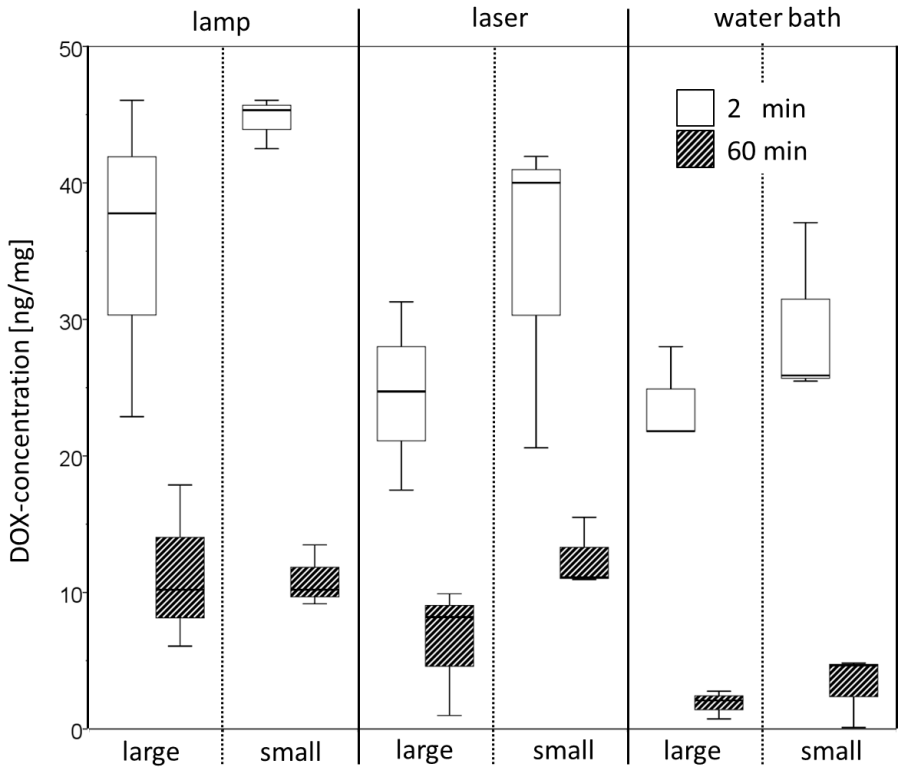

Figure 17: Plasma DOX concentration for all time points grouped by the different tumor sizes and heating methods: 2 min (blank) and 60 min (hatched)

3.4 DISCUSSION

Temperature in the tumor is used as an external trigger for drug release and thus for drug targeting in regional mild HT-induced doxorubicin release using TSL. There are many studies investigating the drug uptake, heat distribution, and therapy outcome with different heating and carrier systems. Laser light for HT itself has been examined for mild HT by different studies [79,94–96]. In combination with encapsulated cisplatin Dou et al. used laser light induced mild HT to heat up a murine subcutaneous tumor and investigated the drug enhancement in the whole tumor and temperature distribution in the heated tumor [82], which is discussed more detailed in the following section.
Laser light is a challenging heating source and—depending on the tissue, perfusion, and wavelength—different heating patterns can be achieved. Laser light used for laser surgery is commonly used in cancer therapy (15172 hits on PubMed) as well as LITT (1290 hits on PubMed), where deterministic effects are used for therapy. On the other hand, searching for 'mild HT and laser' generates 58 hits on PubMed and it is thus not as common in cancer therapy. Although temperature is a key factor, there seems to be no study comparing effectiveness of different HT methods for inducing drug release in vivo. Therefore, the different studies where drug carrier systems are examined regarding their potential for cancer therapy are difficult to compare.

Therefore, three different heating methods for mild HT were compared which were either newly developed or have been often used in small animal models before. To facilitate comparability, the tumor model, the DOX-TSL, the experimental timeline, and minimum tumor temperature were the same for all experiments. To assess the effectiveness of heating and drug release in the tumor, different key factors, including temperature distribution, tumor size, drug enhancement, and pharmacokinetics were examined.

The cold light lamp and water bath were selected for comparison with the new method as both were already established in our group [20,74] and thus allowed optimized therapies and improved assessment of the effectiveness. Requirements that led to the development of a new device were non-invasiveness, MRI-compatibility, and tumor selective heating in small animals. Other methods such as external FUS or RF heating systems—although already in clinical use—were not considered here for several reasons. The TSL release mechanism in FUS was considered not fully comparable because a mechanical trigger is added to the temperature trigger. RF was not considered because of its technical complexity, especially in the MRI environment.

3.4.1 HEATING

For laser and lamp heating, the temperature gradients were comparable and no significant difference was recorded. The unexpected effect of a smaller temperature gradient in the lamp experiment with large tumors, compared to the other methods, can be attributed to the use of two-armed gooseneck lamps, which were positioned on two opposite sides of the tumor. With this setup, it is assumed that it should be possible to heat up larger tumors more homogenously compared to smaller tumors, where the two lamps are naturally closer, and the tumor is effectively heated from above. The laser light causes a higher temperature gradient for heating up large tumors when compared to the other devices, and thus may not be as well-suited if homogeneous temperature distribution throughout a larger volume (above 2.5 cm^3) is of interest. This inhomogeneity might be reduced by an optical system where the light (wavelength = 763 nm) emanates from different directions, as used by Dou et al. in 2014 [82]. They used their system in combination with liposomal cisplatin in mice with a tumor size of max 0.4 cm^3 (maximum 6 – 9 mm tumor growth in one dimension). Further studies are required to investigate the possible implications of such a system for larger tumors (up to 2.5 cm^3), such as those investigated in this work.

By heating the whole leg, using warm water, a lower temperature gradient was achieved for the water bath experiment. The blood was pre-warmed and the tumor was heated from all sides.

To assess the likely unintended negative impacts of HT, like necrosis, skin burn, or oedemas, $CEM_{43°C}$ in the tumor was calculated. In addition, acute effects on heated tissue were evaluated visually. According to publications by Dewhirst et al., Rhoon et al., and Yarmalenko et al., acute minor tissue damage can be expected from 40 - 80 $CEM_{43°C}$ [97–99], and acute and chronic tissue damage can be expected above 81 $CEM_{43°C}$. Thus, a higher $CEM_{43°C}$ in the superficial probes results in a higher probability for “degree one” (red skin, epidermis involved, no blisters, dry textures) to “degree two” burns. Red skin was seen in one laser experiment with a large tumor, one with a small tumor, and for two experiments heated with the lamp with a small tumor. These symptoms were found in animals with calculated single probe equivalent minutes above 40 $CEM_{43°C}$. However, a precise definition of the degree of burning was not possible due to the immediate removal of the tumor, which precluded long term observations to assess such damages.

In 1992, Waldow et al. presented a study where superficial RIF-1 tumors (1.0 cm^3) in mice were superficially heated with a 1064 nm laser [100]. Waldow achieved a temperature gradient of 1.5 °C/mm in the tumors. Its temperature gradient was calculated from the given temperature probe depth and the mean temperature difference in the probes. The

measurements indicated a temperature of up to 52 °C and above on the surface of the tumor for a target temperature of 42.5 °C. Tissue necropsy, blanching, or necrotic areas were observed up to 5 mm depth 48 h after HT. These side effects were not expected to occur from the heating methods used in this thesis because the temperature gradient achieved by Waldow et al. was three times higher than that achieved in these experiments. The gradient difference may be explained as either an effect of differences of vascularization and the resulting blood flow of the different tumor models (no data available), or the modulation of the laser power. Our preliminary experiments with CW heating demonstrated a high temperature gradient compared to the later used modulated laser power. Thus, the high temperature gradient achieved with the 1064 nm laser by Waldow might be attributed to the CW-Laser. The different wavelengths should only have a minor effect because both are in the NIR window, which provides a high penetration depth of the light.

3.4.2 DOX ENHANCEMENT

To exclude unwanted DOX release induced by the heating mattress, three muscle samples were taken from the abdominal wall after the experiment and analyzed with HPLC. The analysis indicated a smaller DOX concentration (0.5 ± 0.1 ng/mg; 2 mg/kg TSL-DOX) compared to previous experiments (> 2.5 ng/mg; 5 mg/kg TSL-DOX) [86]. Even if the DOX concentration in the muscle tissue is normalized on the injected dose, it is recorded at half of the drug concentration compared to previous experiments [86]. Any noteworthy DOX release caused by the heating mattress can be excluded. The impressive stability of the liposomes used for temperatures beneath T_m is likely responsible for the integrity of the results in that respect.

When comparing heated and unheated tumors, a significantly improved DOX enhancement was seen. Here the DOX concentration was 16 – 17 fold higher in the heated compared to the unheated tumors using the lamp, and 13 – 15 fold higher using the laser heating. Compared to HIFU studies summarized by Hijnen et al. (DOX 2-5 mg/kg BW [24] review) or other HT methods [101], the DOX concentration achieved here is of the same order of magnitude. In the HIFU studies, different injection protocols, HT protocols and heating methods were used, which resulted in an increase of between 2.7 and 22.4 fold [24], which may be explained by the huge variation within the experimental setups. These data demonstrate the usability of the laser heating device and illustrate the effectiveness of $DPPG_2$-TSL.

As the volume of a rat leg is approximately 3% of the rat's body weight (own observation) or 9 g for a 300 g rat respectively, DOX tissue concentration in the tumor decreased by a different order of magnitude than the heating volume increased. Such a proportion indi-

cates that most of the drug is still released in the heated tumor and not in the heated leg, but the difference in DOX concentration in the tumor compared to light and laser heating is still significant ($p = 0.02$) for whole tumors. The effect might be a result of higher permeability of the vessels, the higher perfusion in tumor tissue generally, additionally increased by HT, which is discussed further on. Nevertheless tumor-specific heating should be achieved to avoid possible side effects such as skin irritation due to DOX accumulation in surrounding tissue [86].

3.4.3 Interdependence between heating and DOX enhancement

DOX enhancement was highly significant for all three heating methods. The results confirm interdependence between temperature distribution, applied heating method, and tumor size. The achieved DOX-concentration in the small tumors was higher across all experiments when compared to the DOX concentration in larger tumors. One potential explanation for the concentration disparity is that the injected dose of DOX was the same for both groups, while the heated tumor volume where DOX was released was different. This is supported by a significant negative correlation between tumor size and the overall DOX-concentration in the tumor. This effect is slightly less evident in the water bath experiment, which is described further on. The absolute DOX concentration for the water bath was the lowest, which might be caused by the larger heated tissue volume compared to the laser or lamp experiment. The larger heated tissue volume was larger because the heated volume included the whole leg with the.

Contrary to the expected effect that there is an increase in drug tissue concentration with higher tumor temperatures, there was no significant effect on the DOX concentration. A possible reason for that is that, if a specific temperature (> 40 °C) is reached, the drug release out of the liposomes will not be further enhanced [18,102]. Otherwise, it is known that the blood flow in tumorous tissue increases at temperatures above body temperature at HT temperature. Therefore, a higher blood flow in warmer regions—for example in lateral parts of the tumors—should deliver better drug availability, and thus a higher drug concentration. This effect is reversed when the temperature increases above 43 °C – 44 °C [103,104], which can have a negative effect on the perfusion. Nevertheless, a tendency of temperature dependency and DOX in tumor tissue was observed, and thus a temperature above T_m and an as homogeneous as possible heating pattern is crucial for therapy with TSL. Consequently, the most homogenous DOX concentration and temperature distribution was achieved with the water bath experiment; heating the whole leg increases the total tissue volume where DOX is released, while the total amount of DOX-TSL remains the same. Thus, the absolute amount of DOX delivered to the tumor volume decreases relatively.

3.5 CONCLUSION

An adequate heating of subcutaneously applied rodent tumors was possible with all three investigated heating methods. Both, laser and lamp heating achieved local HT treatment of only the tumor tissue. The heating pattern and the heat-triggered DOX release from $DPPG_2$-TSL into the heated tumor tissue were comparable for both methods. The advantages of the lamp system are an easy steering of the light source, significant lower costs and no need of laser associated personal and protective equipment like safety google and facilities with restricted access. If an MRI-compatible heating device is necessary, a laser-based HT system is preferably used as an easy MRI-appropriate guidance of laser power to the heated tissue. To provide a sufficient heating pattern, a maximum of $2.5cm^3$ tumor volume should not be exceeded.
In contrast, a water bath yields a more homogenous heating pattern, but since the whole leg is heated, the HT treatment is regional rather than local. Therefore, the achieved DOX enhancement ratio is significantly lower than those observed in the other two heating methods. This renders the occurrence of unwanted side effects in the normal tissue of the heated leg more likely, which highlights the exigency of therapy studies.

This standardized comparative study demonstrated that the tumor size and the method of heating must be considered when comparing the efficacy of temperature-induced drug release in subcutaneous experimental tumors. Drug delivery and drug targeting through the use of $DPPG_2$-TSL was shown to be even more efficient when using tumor specific heating. The heterogeneous DOX tissue concentration demonstrated the necessity for visualization of drug release and drug concentration in tumor tissue to improve the outcome of chemotherapy that uses $DPPG_2$-TSL.

The new laser light applicator is a valuable tool for exploration of local mild HT in subcutaneous tumor models. Consequently, the applicator was chosen for further investigation of drug-loaded TSL combined with mild HT and MR-Imaging.

4. THERAPY MONITORING WITH MRI

For locally advanced cancer, chemotherapy is commonly used within multimodal treatment strategies. In order to improve antitumor efficacy, knowledge of local tissue drug concentration would contribute clear advantages. At this point, drug concentration can only be derived from invasive biopsies. The limitation of biopsies is that only a small part of the tumor can be analyzed, neglecting the possibility of heterogeneous perfusion, varying vessel permeability, various interstitial fluid pressures, or different types of tissues (like necrosis) throughout a single tumor. These distinct tissue characteristics also result in a heterogeneous drug distribution within the tumor volume and then tissue characteristics complicate optimal therapy planning. Therefore, non-invasive imaging methods that survey the whole tumor, like MRI [29], PET [28], SPECT [105], are under development for drug dose painting or chemodosimetry.

Therapy monitoring of chemotherapy with TSL and imaging could facilitate more personalized medicine that achieves a better therapy response. Furthermore, as described in chapter 3, the temperature distribution in the treated volume influences drug release. Thus, the aim of this part of the work was to investigate an imaging method for non-invasive 3D temperature measurement and to structure a method for estimation of drug delivery into tumor tissue.

For image-guided drug delivery with TSL, MRI offers unique features. Encapsulation of paramagnetic MRI CA, such as the clinically utilized Gd-DTPA, allow the assessment of additional information on drug release and temperature pattern during therapy [29,63]. This is based on the indirect effect of CA on MRI signals in comparison to other imaging methods, such as X-ray, as described previously (Chapter 2.5.9).

The first step of this study involves verifying that a sufficient release of MR contrast agent with the laser light applicator is possible. Secondly, the possibility of MR-thermometry in the presence of CA-TSL is investigated in combination with drug dose painting, which is the subject of controversial discussions [106–109].
The third and final step of the study consists of testing a variety of static and dynamic MR parameters as surrogate markers for the quantification of HT-induced DOX release in tumors, using a mixture of TSL loaded with CA or DOX.

Parts of this section (Chapter 4.) are published in the Journal Of Controlled Release by Peller and Willerding et al. 2016 [110].

4.1 MATERIALS AND METHODS

4.1.1 EXPERIMENTAL SETUP

Six rats with two tumors each—one in each hind leg—were treated with DOX-TSL combined with CA-TSL during a dynamic MRI-measurement.

The rats were prepared (chapter 4.1.2) for the experiment eleven days (+ 2 days) before MR-Imaging and HT. For the MRI, the rat was positioned in the MRI-receiver coil (SMS Precision Eight Wrist Array Coil, Invivo, USA) together with the laser HT applicator. After T_1-, T_2, and PD weighted measurements for morphologic information and T_1 quantification of the tissue, a dynamic scan was started. After baseline measurement, mild HT was induced with the laser applicator in four of the six rats, while two animals remained unheated as a control group. Once the temperature in the probe had reached a stable value above 40 °C, CA-TSL (0.1 mmol/kg) was injected simultaneously with DOX-TSL (2 mg/kg) (Supplementary table 4, 5 and 6) (duration of bolus: ~ 10s). The tumor temperature was thereafter kept constantly above 40°C (preparation of liposomes is described in chapter 3.2.1). 60 min after injection, the laser was switched off, but the dynamic scan continued for another 20 min during cooling of the tumor.

After the MRI scan, the heated tumors were excised and prepared for HPLC analysis. Two tissue probes per rat (one sample of heated tumor and one not-heated tumor sample) were analyzed by HPLC. Static and dynamic MRI-information were used for further analysis. Post-processing was executed within the software “PMI”, which was (0.4) developed in-house.

For further examination of therapy monitoring, the following parameters were evaluated: the AUC of T_1-relaxation time over time, difference of T_1 relaxation time before and after heating, and the phase difference. Furthermore, dynamic and static phase change was considered.

4.1.2 ANIMAL MODEL

Experiments were performed in accordance with approved protocols (Regierung von Oberbayern, AZ. 55.2.-1-54-2532-144-11). The experiments were performed under anesthesia (isofluran 2-5 % and oxygen 1.5 l/min), administered with an isofluran evaporator.

Animal preparation with tumor for a bulk tumor: For tumor growth, $1.5x10^6$ / 50 µl BN175 cells were injected in one hind leg. Tumor growth was recorded with caliper measurements. The volume was calculated using an ellipsoid approximation (equation 19). After

10-14 days, the volume reached 1 cm^3 and the tumor was removed as a bulk tumor. Fragments of about 2x2x2 mm^3 of this tumor were stored in liquid nitrogen.

Animal preparation with tumor for MRI investigation: Fragments from the bulk tumor were implanted into a new animal. The advantages of this method compared to injection of cells are more homogenous tumor growth, prevention of cell dispersion, and prevention of invasive tumor growth.

For implantation of tumor pieces, both hind legs of the rat were shorn, and the skin was opened with a surgical scissor. The tumor was then implanted as deeply as possible in a subcutaneous tube. The wound was closed with a suture. Tumor growth was measured in three planes every second day, and the volume was calculated as described in the preceding study.

The exact size of the tumor at the time of the MRI experiment could not be fully measured because of restricted availability of measurement time on the clinical MRI-scanner. The tumors were allowed to grow for at least 11 days. Depending on the availability of scan time, there was a variation of + 2 days.

During MRI, body temperature was controlled by a rectal temperature probe and a water heating mattress. To prevent liposomes from releasing the drug due to the heating mattress, the water temperature was kept below 39 °C. To reduce MRI flow artifacts caused by the heating mattress, 20 mMol/L $MnCl_2$ was added to eliminate the signal from the water of the heating mattress by strong decreasing T_2*.

4.1.3 INVASIVE TEMPERATURE MEASUREMENTS

As a reference for MR thermometry, and to monitor absolute tumor temperature, invasive temperature measurement was performed using one intratumoral fiberoptic temperature probe (Reflex™ Signal Conditioner, Neoptic Inc., Canada) for tumor temperature control, and one rectal probe for body temperature measurements. The tumor probe was implanted with the assistance of a cannula (20G needle, BD Microlance™, Germany). The principle of probe implantation is described in figure 18. Morphologic MR-images were used to control the position of the temperature probe after bringing the rat into the MR-Scanner.

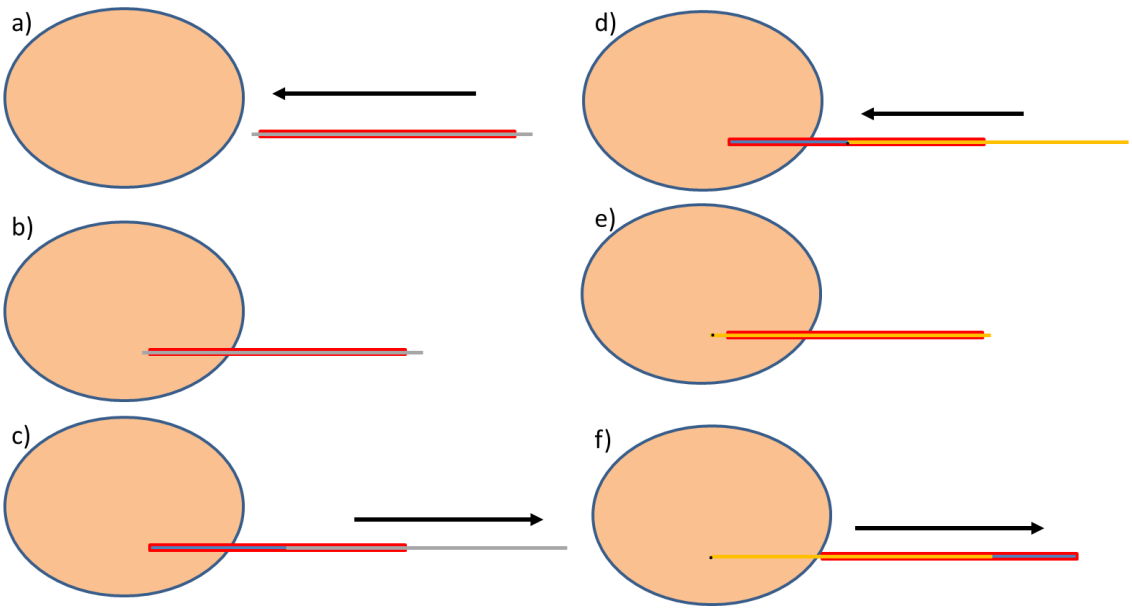

Figure 18: a) – b) insertion of the cannula including the needle in the lower third of the tumor c) needle was removed, cannula stayed inside the tumor d) – e) insertion of the temperature probe f) cannula was removed

After insertion, the probe was fixed to the rat with tape. The rectal tumor probe was inserted approximately two centimeters and fixed with tape to the rat's tail.

Tumor and body temperature were measured every second during the MRI experiments, and data was recorded every 10 seconds (via an AD converter with a laptop).

4.1.4 MRI TEMPERATURE MEASUREMENT

The sensitivity of T_1 to temperature change is tissue-dependent. This dependency factor m was determined for each animal. Therefore, dynamic T_1 change (ΔT_1) from a region of interest (ROI) around the tumor probe tip was fitted with the corresponding temperature change (ΔT_{probe}) from the tumor probe in equation 22.

$$\Delta T_{probe} = m * \Delta T_1 \quad \textbf{22}$$

To exclude the influence of injected TSL with CA, only data before injection of CA-TSL was used.

The PRFS coefficient was set to -0.01 $^{ppm}/_{°C}$ because it is mainly independent of tissue characteristics, as described by Rieke et al. [63] (see chapter 2.5.8).

4.1.5 HEATING

Tumors were heated with the laser light as described in chapter 3. To verify a minimum temperature of 40 °C throughout the whole tumor during the experiment, the required target temperature in the tumor probe was estimated with the tumor probe depth and the temperature gradient demonstrated in chapter 3.3.2. The target temperature was calculated with equation 23.

$$T_t = dT * \Delta p_d + T_{min,}$$

23

where T_t is the target temperature, dT/dx as temperature gradient that is set to 0.48 °C/mm (Table 3), T_{min} is the minimum target temperature of 40°C and Δp_d is the distance from the base of the tumor to the tumor probe. Tumor probe depth was measured in the pd-, T_1- or T_2- weighted morphological images on the MRI workstation.

4.1.6 MR ACQUISITION

Measurements were performed on clinical 3-T whole-body system (MAGNETOM Verio & MAGNETOM Skyra, Siemens Healthcare, Germany). For signal acquisition, a dedicated 8 channel wrist coil (SMS Precision Eight Wrist Array Coil, Invivo, USA) was used. Applied sequences and MR parameters are described in later sections.

Morphological Imaging

Prior to the T_1-quantification and MRI temperature measurements, T_1 weighted (TR/TE, 15.3/6.4 ms, 4 averages, FA = 10°) and a T_2 weighted (TR/TE, 6240/95 ms, 3 averages, FA = 142°), turbo spin echo images of 22 sagittal slices with a slice thickness of 2.5 mm were acquired using a 62 x 90 mm^2 FOV and a matrix size of 264x384. The total acquisition time for morphological images was around 15 min. These images were used for tumor localization and size measurements.

T_1 Quantification

As described above, T_1 can be used for temperature mapping and it is—for a defined range—a linear indicator of contrast agent concentration. In the following section, the sequences for T_1-quantification and dynamic measurement are described.

For static and dynamic T_1 mapping the variable FA method was used.

TWIST sequence

For T_1 mapping a 3D-gradient echo sequence with view-sharing was also used. In conventional MRI-sequences, the whole k-space is sampled for one image at a time, whereas the TWIST (Time-resolved Angiography With Stochastic Trajectories) sequence (Siemens Healthcare, Germany) shares parts of k-space for several images and achieves accelerated data acquisition for one image with the so-called "data sharing-method". As the inner k-space is responsible for the image contrast, the TWIST sequence samples only the inner k-space for every time point, while the outer k-space is only sampled partially, and missing parts are filled using previously acquired k-space data [111].

A 3-D-k-space is sampled with a readout direction in k_x and a phase-encoding direction in k_y and k_z. As described by Laub et al. in 2006 [112], all points are sorted by their polar coordinates. The first sorting criterion is the distance k_r from the middle of the phase-encoding plane with:

$$k_r = \sqrt{k_y^2 + k_z^2}$$

24

The sampling points were subdivided according to their radial distance k_r from the center of the k-space in two groups: Group A with $k_r<K_C$ representing the points with low spatial frequency and Group B with $k_r>K_C$ the points with high spatial frequency. Group B was randomly divided into different subgroups B_j with j = 1, 2, 3,..., N. During a dynamic image acquisition, the k-space is sampled only once in total. This happens either at the beginning or at the end of the dynamic acquisition. For the other time points, only area A and one subgroup B_j is sampled. To obtain complete k-space information, the next time point is sampled with area A and subgroup B_{j+1} until the whole k-space is sampled. Missing data for a specific time point are taken from previous (backward data sharing) or following (forward data sharing) acquisitions (Figure 19).

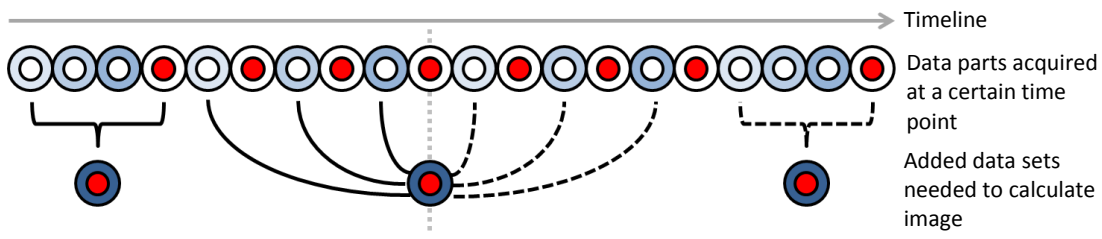

Figure 19: Reconstruction of k-space: continuous lines show "forward data sharing" and dashed lines show backward data sharing. Differing brightness show the different B_j.

The time required to obtain a reconstructed image (nominal time resolution TA_{TWIST}) can be described with:

$$TA_{TWIST} = TA_{full}(S_A + (1 - S_A)pB)$$

25

Where TA_{full} is the acquisition time for the whole k-space, S_A is the normalized size of sampling area A and pB is the sampling density of area B. Hence, two parameters influence the total acquisition time: with a reduction of the area A or by lowering the sampling density of area B, the required acquisition time can be reduced.

B_1 inhomogeneities and flip angle correction

For accurate and precise T_1-mapping with the VFA method, a homogenous RF transmission field (B_1) is needed. The inhomogeneities of the RF pulses necessitate correction of the FA, particularly at high magnetic field strengths. In 2006, Cunningham et al. suggested a technique to quantify the FA error [113] using a modified double angle method (DAM) for correction. DAM was previously described by Stollberger et al. [114] and Insko et al. [115]. Such a method allows the calculation of a flip angle map, which is an indirect measurement of the B_1 field.

Two images are acquired: I_1 with a flip angle α_1 and another image I_2 with $\alpha_2 = 2\alpha_1$. If all other signal-affecting sequence parameters are kept constant, the ratio of the magnitude images is [113]:

$$\frac{I_2(r)}{I_1(r)} = \frac{\sin\alpha_2(r)\ f_2(T_1, TR)}{\sin\alpha_1(r)\ f_1(T_1, TR)}$$

26

where r represents the spatial position of every voxel and $\alpha_1(r)$ and $\alpha_2(r)$ are the attendant local flip angles. For long repetition time ($TR \geq 5\ T_1$), f_1 and $f_2 = 1$. Cunningham's DAM was modified for the TWIST sequence used here because radial readout was not possible, and the reset sequence employed to bring the spin population to the same state regardless of their excitation, was not available. A long repetition time was used during which the longitudinal magnetization was recovered, and thus the actual flip angles can be written as:

$$\alpha(r) = arccos\left(\left|\frac{I_2(r)}{2I_1(r)}\right|\right)$$

27

For the flip angle correction, a TWIST sequence—as described in a later section—was also used. For I_1; α_1 was set to 22° and for I_2; α_2 was 11°. The TWIST sequence was limited to a maximum FA of 23° before changing the RF pulse type. The highest possible FA was chosen for stability reasons as a higher FA facilitates a more robust FA correction [116]. Aside from the dynamic measurements, K-space was sampled in total for every image. To mini-

mize T_1-effects, TR was set to 5000 ms. In order to reduce the acquisition time, parallel imaging (SENSE; R = 2) was used and matrix size was halved in the in-plane direction while maintaining the FOV—as used in the TWIST sequence—and using interpolation to fill in the missing data points. Total acquisition time for flip angle correction was 10 min and $\alpha_{(r)}$ was calculated retrospectively. Relative FA (α_{rel}) map for correction was calculated with:

$$\alpha_{rel} = {}^{\alpha(r)}/_{\alpha_{preset}}$$

28

where α_{preset} is the FA as set in the sequence parameter and $\alpha(r)$ is the calculated real FA from equation 27.

Static and dynamic T_1-mapping with the VFA method

Static T_1 -mapping

For relaxation time mapping before and after cooling (baseline mapping), a T_1 -measurement was used with seven different flip angles (5°, 7°, 10°, 12°, 15°, 18°, 23°) within the following parameters.

TWIST parameters were S_A = 30, pB = 20. The matrix size was 132 x 192 x 22 with FOV of 62 x 90 x44 mm^3 and the receiver bandwidth was 200 Hz/pixel. TR was fixed to 10.12 ms and TE to 6 ms. The relative long TE was chosen for PRFS measurement during dynamic measurement. TR was minimized as far as possible. Five averages were acquired for each flip angle to increase the SNR for baseline measurement. Total acquisition time was 8.5 min for a complete T_1-map. Baseline T_1 and M_0 map was calculated pixel-by-pixel by linear fitting of the FLASH equation to the acquired data for the linearized data of VFA measurements.

Dynamic T_1-mapping

For fast T_1 quantification during the treatment, a single FA mapping method was used. To reduce systematic errors, sequence parameters were optimized .

As described by Dietrich et al. in 2014 [62], a statistical error in dynamic T_1-mapping with one FA can be estimated by equation 29 (see also figure 20):

$$\Delta E_{1,dyn} \approx \frac{(1 - E_{1,dyn} * \cos(\alpha_{dyn}))^{2}}{S_0 \sin(\alpha_{dyn}) * (1 - \cos(\alpha_{dyn}))} \Delta S_{dyn}$$

29

where $E_{1,dyn} = \exp(-T_R/T_{1,dyn})$. This error is a function of α_{dyn}, defining a unique minimum for the optimal flip angle $\alpha_{dyn,opt}$ for dynamic T_1 measurements. The optimal FA $\alpha_{dyn,opt}$ can be calculated by:

$$\alpha_{dyn,opt} = \arccos\frac{2E_1 - 1}{2 - E_1}$$

30

where $E_1 = \exp(-T_R/T_1)$. For the T_R = 10.12 ms, as used in this case, the optimal FA for different T_1 relaxation times is shown in figure 20.

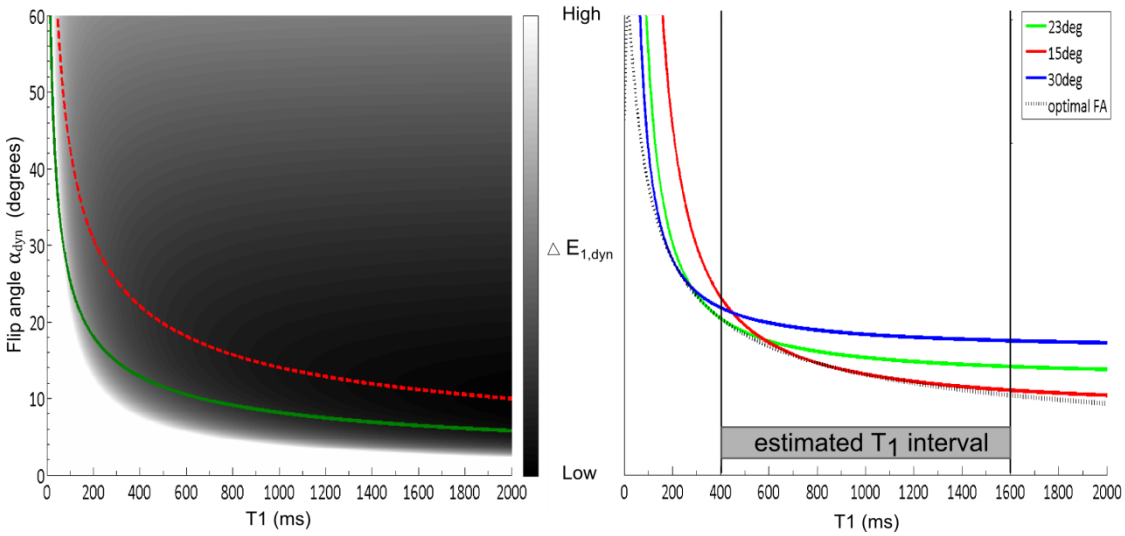

Figure 20: a) The minimum error as a function of T_1 for given T_R is indicated by the dotted red line. For comparison, the Ernst angle is shown as a solid green line. Statistical error $\Delta E_{1,dyn}$ of dynamic T_1 measurement as a function of T_1 and FA is shown grey-scaled. b) Statistical $\Delta E_{1,dyn}$ error for 15°, 23°, and 30° (red, green and blue) is dependent on T_1. Statistical error for the optimal FA for every T_1 is marked with a black dotted line. The estimated T_1 interval is marked with two vertical black lines [62].

Estimated T_1 times in the rat tissue before, during, and after the treatment were 400 ms - 1600 ms. Therefore, for the dynamic T_1 measurement with one FA, 23° was chosen because it provides a low and stable estimated error across the whole T_1 range (Figure 20 b)). All other parameters except the averages stayed the same as the static baseline T_1-measurement described before. Time resolution for one time point was set to 9.73s.

Equation 31 was used to calculate dynamic longitudinal relaxation time $T_{1,dyn}$ for each pixel and for every time point *t,* considering the actual flip angle from preceding DAM measurement.

$$T(t)_{1,dyn} = -TR/log\left(\frac{M_0 * \sin\alpha - S(t)_{dyn}}{(M_0 * \sin\alpha) - S(t)_{dyn} * \cos\alpha}\right)$$

31

Where *TR* is the repetition time, M_0 is the baseline proton density map acquired by the multi-FA measurement, α is the used flip angle, and $S(t)_{dyn}$ is the dynamic signal at time point t.

PRFS measurement

Phase information was also reconstructed from the dynamic TWIST sequence raw data. Thus, a dynamic phase data set with the same sequence parameters as the magnitude images and T_1 calculation was reconstructed retrospectively. For post-processing, phase discontinuities caused by > 2 π phase jumps were corrected by adding an integral number of cycles. One-dimensional phase unwrapping that detects jumps of more than a half cycle in the data set was applied using the MATLAB unwrap function [117]. As only the phase change in the time dimension was evaluated, in-plane phase unwrapping was not necessary. The algorithm was implemented in PMI software. These phase data were used for temperature determination before injection based on equation 18 and as a surrogate marker for chemodosimetry, as described thereafter. For correction of phase drift caused by magnetic field drift and coil sensitivity during long experimental time periods, the phase information of unheated tight muscle was used.

4.1.7 STATISTICAL ANALYSIS

Statistical analysis was performed using SPSS V22 (IBM, Germany). The correlation analysis employed the concept of bivariate correlation according to Pearson. Differences between two data sets were established using the parametric two-tailed student's t-test. Normal distribution was tested with the Kolmogorov-Smirnov-test. For regression analysis, fit models were tested with the ANOVA test [93]. p-values were considered to be "significant" if they were less than or equal to 0.05, and "highly significant" when less than or equal to 0.01. Modified Bland Altman plots, as described by Krouwer [118], were calculated by MATLAB R2012a (MathWorks Inc., Natick, USA).

4.2 DRUG QUANTIFICATION WITH MRI / CHEMODOSIMETRY

To quantify drug delivery in tumor tissue, several semi-quantitative and quantitative parameters derived from the dynamic and static T_1-time information and the phase information were considered as potential parameters to predict the invasive DOX measurement. Semi-quantitative derived parameters based on signal intensity from the signal curve depend strongly on acquisition parameters and external influences, such as coil sensitivity. Therefore, only quantifiable parameters, such as dynamic and static T_1-values and the dynamic phase change information, were used for drug concentration measurements.

In particular, the correlation between the HPLC DOX-concentration and MRI-parameters was examined.

The following parameters were determined from either T_1 or the phase-dynamic tissue curve, as illustrated in figure 21.

- AUC for relative and absolute T_1 change during the treatment (T_1_1FA_AUC_rel [%*s]; T_1_1FA_AUC_abs [ms*s])
- Relative and absolute T_1 difference for total acquisition time measured with one FA (T_1_1FA_total_rel [%]; T_1_1FA_total_abs [ms])
- Relative and absolute T_1 difference for the therapy time measured with one FA (T_1_1FA_treatment_rel [%];T_1_1FA_treatment_abs [ms])
- AUC for proton resonance frequency shift [rad*s] during the treatment (Phase_AUC [rad*s])
- Absolute proton resonance frequency shift during the treatment (Phase_diff [rad])

Furthermore, the VFA measurement with 7FA was used for the analysis of:

- Relative and absolute T_1 time difference for total acquisition time measured with seven FA (T_1_7FA_rel [%]; T_1_7FA_abs [ms]).

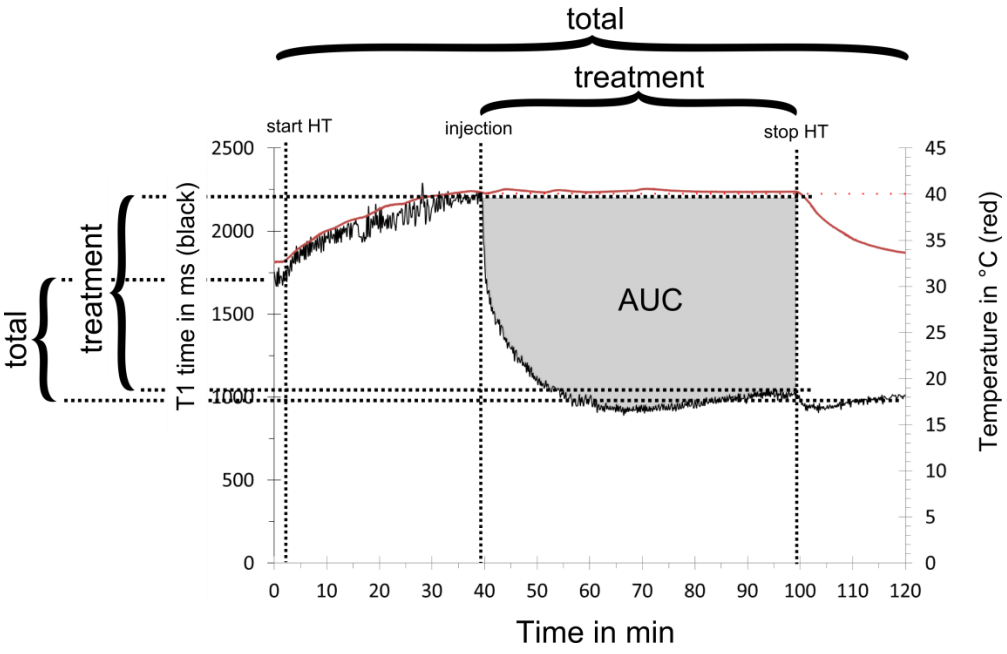

Figure 21: Illustration of several descriptive parameters that were utilized: AUC (grey); total T_1 difference; treatment T_1 difference. The red line depicts the dynamic temperature data.

ROI were chosen manually from the dissected tumor volumes, slice by slice, until the total tumor volume was considered (Figure 22 c). ROIs of a tumor were summarized to a volume of interest (VOI). For each VOI, mean values for each MR parameter were calculated. The ANOVA test was used in order to establish whether a linear regression was a suitable surrogate parameter for DOX, and HPLC DOX-concentration was used as the independent variable. These mean MRI parameters were correlated with the DOX concentration deter-

mined by HPLC using a linear regression analysis of the data from all of the animals (Figure 22 d). Parameter maps were then calculated pixel-by-pixel with this DOX concentration (Figure 22 e). For further analysis, the VOIs of each heated tumor were halved to represent the two halves obtained by bisecting the tumor during excision (Figure 22 c). For all VOIs, mean DOX values were calculated from MRI DOX maps and compared to corresponding DOX measured by HPLC. These data were fed into a Bland Altman plot where the reproducibility coefficient (RPC = 1.96*SD of mean error) facilitated comparison of the different MRI markers (Figure 22 f).

The procedure for calculating tissue DOX concentration based on static T_1-measurement is illustrated in figure 22 for the relative T_1 time difference before and after HT (T_1_1FA_treatment_rel). The figure uses the procedure of DOX calculation representatively, as an example for other parameters.

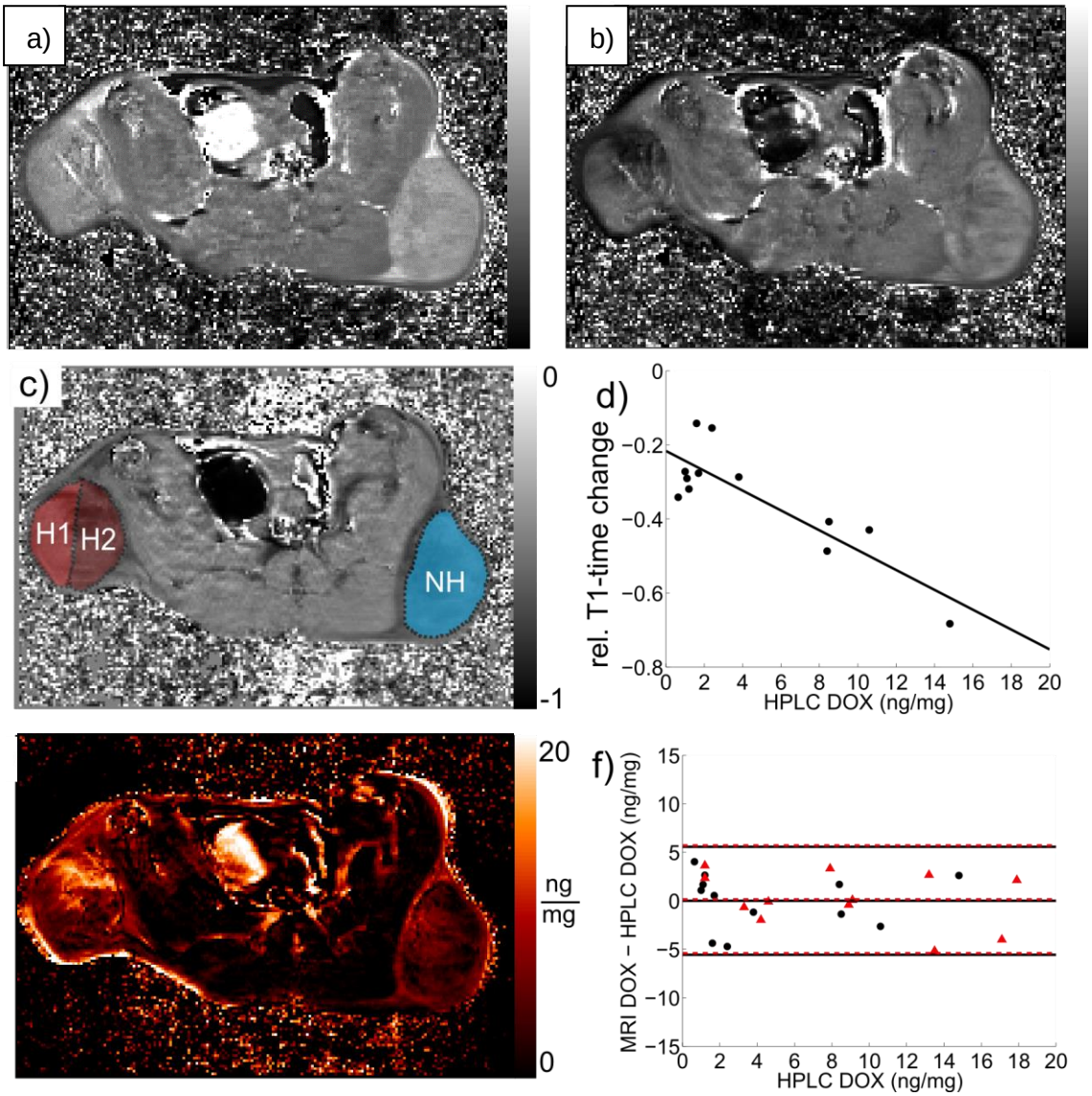

Figure 22: Procedure for calculating T_1-based liposomal DOX concentration from T_1_1FA_treatment_rel as an example for other parameters. a) Corresponding T_1-map [ms; 0 ms – 2000 ms] before injection calculated with 1 FA b) Corresponding T_1-map [ms; 0 ms - 2000 ms] before cooling down calculated with 1 FA c) Calculated T_1-time difference [%/100] with used ROI's (H1 → lateral tumor part; H2 → medial tumor part; NH → unheated reference tumor) for correlation drug concentration in tissue d) Results for HPLC validated DOX measurements [ng/mg] from each animal compared to corresponding T_1-difference for whole tumors with resultant linear regression e) Pixel-by-pixel calculated DOX concentration map [0 ng/mg – 20 ng/mg] f) Bland Altman plot for HPLC validated DOX measurements [ng/mg] for all animals and whole tumors (black, solid, dot) and halved tumors (red, dashed, triangle) compared to MRI calculated DOX concentration [ng/mg].

4.3 RESULTS

All six animals were examined successfully: the four animals in which one tumor was exposed to mild HT (rat weight of 313 g ± 75 g; N61, N62; N84; N85) were included in group A, and two without HT (357 g ± 33 g; N66, N67) were included in group B as a control group. HPLC analysis was performed on the 18 tumor samples. Tumor volume was 1.2 cm^3 with a standard deviation of 0.7 cm^3 for heated tumors and 1.0 cm^3 ±1.3 cm^3 for unheated tumors. Two animals exhibited a reddish skin with no signs of burning on the heated tumor. In the proton density weighted images, all tumors demonstrated a relatively homogeneous hyperintense signal compared to muscle tissue with few hypointense structures. The T_1 weighted images depicted hypointense structures uniformly distributed throughout the whole tumors, with a tendency towards an appearance in the medial part of tumor. In the T_2 weighted images, the tumors were hyperintense with hypointense structures. No specific CA enhancement patterns, such as those described by Ponce et al., were detected [101].

The target temperature calculated with equation 23 and the measured tumor temperatures for all experiments are displayed in table 8. For animal N85, T_1 mapping with 7 FA after treatment was not possible due to motion artefacts. For one experiment (N62), a temporal malfunction of the laser resulted in temperature fluctuation throughout the therapy, but a mean temperature of 40.2 ± 0.7 °C was still achieved. Two animals remained unheated as reference. All animals were used for analysis.

Animal	distance to base [mm]	Target temperature [°C]	mean tumor temperature with SD [°C]
N61	1	40.4	40.3 ± 0.1
N62	2	40.9	40.2 ± 0.7
N84	1	40.4	40.2 ± 0.1
N85	4	41.9	41.9 ± 0.1
N66	1	unheated	32.9 ± 0.1
N67	2	unheated	33.7 ± 0.3

Table 8: Distance to the base of the tumor with corresponding target temperature and reached mean tumor probe temperature during therapy with SD for all MRI experiments.

The laser heating device induced no visible artefact at with the distance of 10 mm between the metal coating of the prism and the tumor. Laser light did not interfere with the temperature probe.

All shown MRI pictures are from animal N62 and serve as representative examples of the rest of the experiments.

4.3.1 T_1-MEASUREMENT AND VALIDATION

Flip angles for T_1 calculation were corrected by a relative flip angle map (Figure 23 b)) measured for each animal. For every tumor-VOI and region in the muscle, the mean T_1 was calculated (Table 9) from corresponding T_1-maps (Figure 23 c)-f)).

		T_1 time (ms)			
		VFA (7FA)		VFA (1FA)	
Animal / Group	tumor part	prae	post	prae	post
N61 / A	heated tumor	1586	657	1446	459
N62 / A		1498	1030	1539	998
N84 / A		1363	983	1300	879
N85 / A		1557	X	1369	890
Mean		1501 (99)	890 (203)	1414 (103)	807 (238)
N61 / B	reference tumor	1617	1458	1544	1111
N62 / B		1846	1338	1909	1344
N66 / B		1467	935	1480	1029
N67 / B		1386	805	1430	968
N66 / B		1807	1150	1827	1315
N67 / B		1472	1013	1581	1279
N84 / B		1557	1145	1505	1044
N85 / B		1559	X	1331	1200
Mean		1589 (163)	1121 (227)	1576 (197)	1161 (143)
N61	muscle	1302	1353	1307	1325
N62		1372	1323	1243	1074
N66		1350	1215	1339	1234
N67		1411	1254	1329	1285
N84		1349	1289	1167	1116
N85		1406	X	1394	1223
Mean		1365 (41)	1287 (55)	1279 (80)	1210 (97)

Table 9: T_1 [ms] values before and after therapy for the heated tumor (A), reference tumor (B) and muscle tissue for all experiments as well as the different T_1 measurement methods pre-heating and post heating. ROIs for muscle has 150 pixels in one plane. SD values are given in brackets.

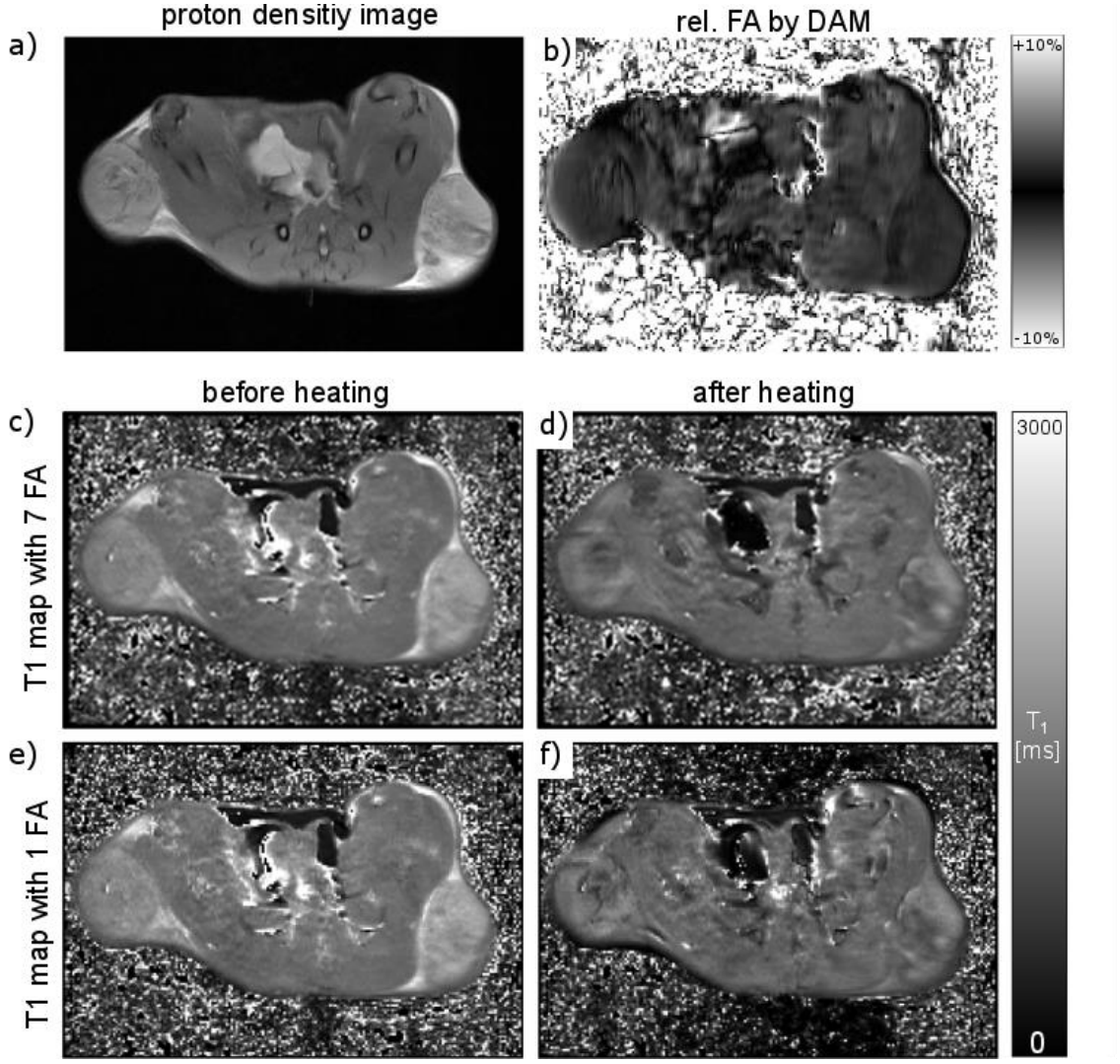

Figure 23: a) Representative morphologic proton density image. b) Corresponding relative FA map gained by the DAM-method. c) - f) T_1-relaxation times acquired with the VFA Method with seven FA and with one FA before and after the treatment.

4.3.2 PHASE SHIFT MEASUREMENT

Phase shifts acquired by the dynamic TWIST sequence were used for temperature measurements and drug dose painting, as described previously. Phase shift ranged from -1.19 rad to +0.12 rad for whole tumors after injection of CA-TSL. Injection of CA-TSL had only minor effects on phase change in the muscle tissue that lasted less than 2 min.

4.3.3 TEMPERATURE MEASUREMENT

Temperature data from the fiberoptic temperature probe

A target mean temperature level of 40°C was reached for all animals treated with mild HT. Body temperature did not reach a temperature above 37 °C. For every experiment except for N62, temperature was kept constant above the target temperature. During the N62 experiment, a technical malfunction of the laser led to short periods (~ 4 x 120 s) with no heating. During these periods, temperature decreased below the target temperature. Temperature data for all experiments is shown in table 10.

		After injection				
Experiment number		T_{10} (°C)	T_{50} (°C)	T_{90} (°C)	Mean tumor temperature (°C)	Maximum temperature (°C)
Group A	N61	40.4	40.3	40.1	40.3 ± 0.1	40.6
	N62	40.6	40.4	37.7	40.2 ± 0.7	41.4
	N84	40.3	40.2	40.1	40.2 ± 0.1	40.4
	N85	42.0	41.9	41.1	41.9 ± 0.1	42.2
Group B	N66	32.7	32.7	32.5	32.9 ± 0.1	33.0
	N67	33.8	33.6	33.4	33.7 ± 0.3	34.8

Table 10: Temperature data from the temperature probe after injection of drugs until 1 h after injection. T_{10} and T_{90} denote 10% or 90% of the temperature data were above this temperature level.

MRI temperature measurement

Temperature maps based on MRI were calculated retrospectively using PRFS and with T_1 change as described in chapter 2.5.8 and 4.1.4. Results are shown in figure 24. For T_1 temperature measurements, the temperature dependency was determined to be 1.2 %/ °C, as described in chapter 4.1.4. Accuracy of the temperature measurements was within + 0.4 °C with a standard deviation of ± 1.1 °C for experiments with HT and 0.7 °C ± 1.5 °C for all experiments in the same ROIs as in PRFS temperature measurement (Table 11). After injection of CA-TSL, an error of up to ± 30 °C occurred in T_1 and PRFS temperature measurements.

	PRFS		T_1	
Experiment	mean error [°C]	SD [°C]	mean error [°C]	SD[°C]
N61	0.1	0.8	-0.2	1.2
N62	-0.1	0.9	0.1	1.5
N66	-0.2	1.1	0.3	1.9
N67	1.3	3.1	2.2	2.6
N84	0.0	1.0	0.9	0.6
N85	0.0	1.2	0.6	1.1
Mean	0.2	1.4	0.7	1.5

Table 11: Mean error for temperature measurement from start of measurement until injection of TSL and temperature in the tumor right before injection with SD as an indicator for temperature distribution for all experiments.

Temperature change calculated with PRFS indicated a significant ($p < 0.000$) correlation of about 0.944 to temperature change measured with the fiberoptic probe before injection of the CA-TSL for all experiments. This is demonstrated by a temperature change measurement with an accuracy of -0.1 °C and with a standard deviation of ± 1.0 °C for experiments with HT and 0.2 °C ± 1.35 for all experiments within a ROI (amount of pixel $6 < n < 15$) around the tip of the probe from the beginning of heating until injection. By contrast, after injection MRI temperature measurements revealed an error from -2 °C up to + 9 °C for all experiments.

Temperature histograms and temperature standard deviation from the heated tumor just prior to injection were developed as an indicator for temperature distribution in the heated tumor. Figure 24 illustrates the temperature histogram corresponding to temperature maps for animal N62. Temperature maps generated with PRFS resulted in a homogeneous temperature map, while T_1-generated maps showed a higher noise level.

Dynamic tumor temperature data for N62 is shown in figure 25 (a) visualize the temperature curve before and after injection during laser malfunction. Immediate strong fluctua-

tions were observed for temperature changes around 40 °C for the T_1 based parameter. The temperature curve for an experiment with a temperature above the target temperature for the entire duration of the treatment is shown in figure 25 (b). There were no rapid changes during the treatment in the T_1 and PRFS temperature measurements. The calculated temperature after injection of CA-TSL yields unrealistic temperature values, and data was only shown in figure 25 to demonstrate this effect.

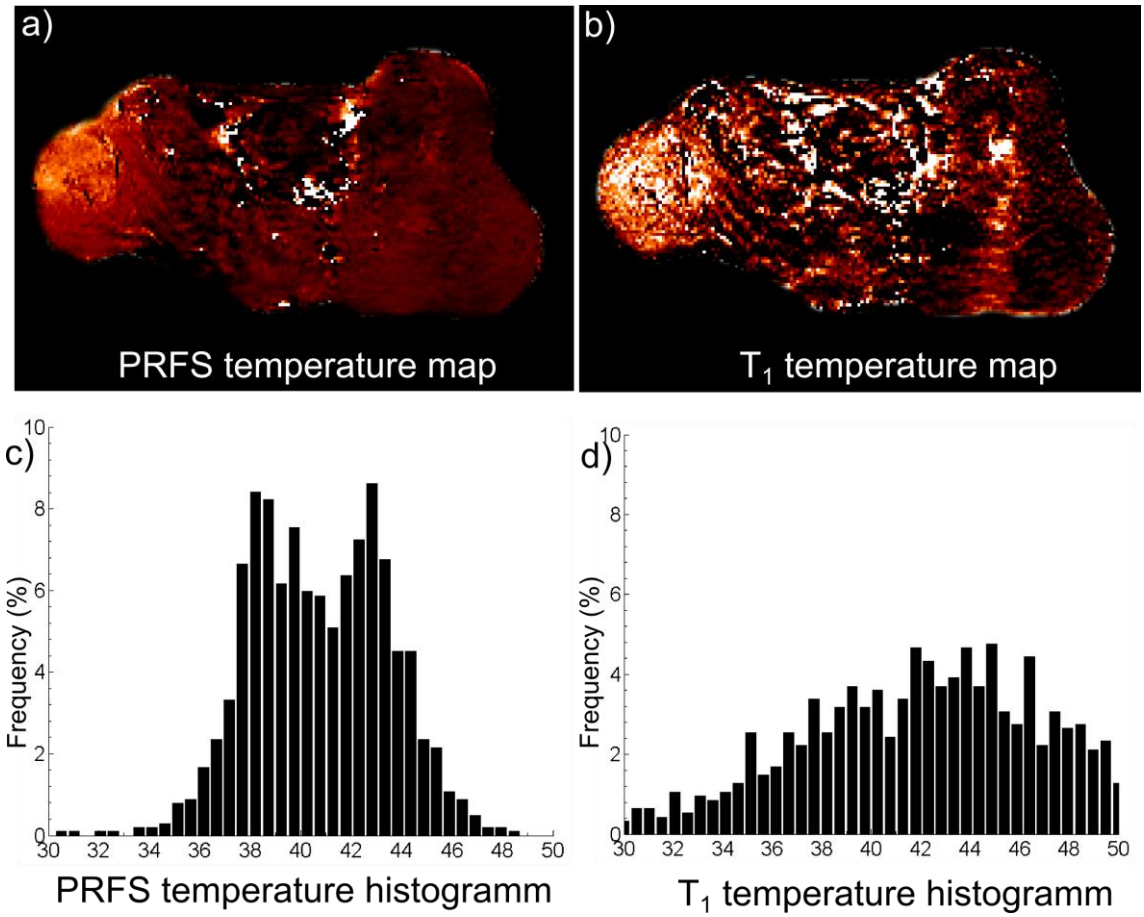

Figure 24: Temperature map axial cross-section of rat with heated and reference tumor for a) PRFS and b) T_1 based temperature change calculation for each pixel immediately before injection c) - d) corresponding temperature histogram to analyze temperature distribution in the heated tumor on the left side.

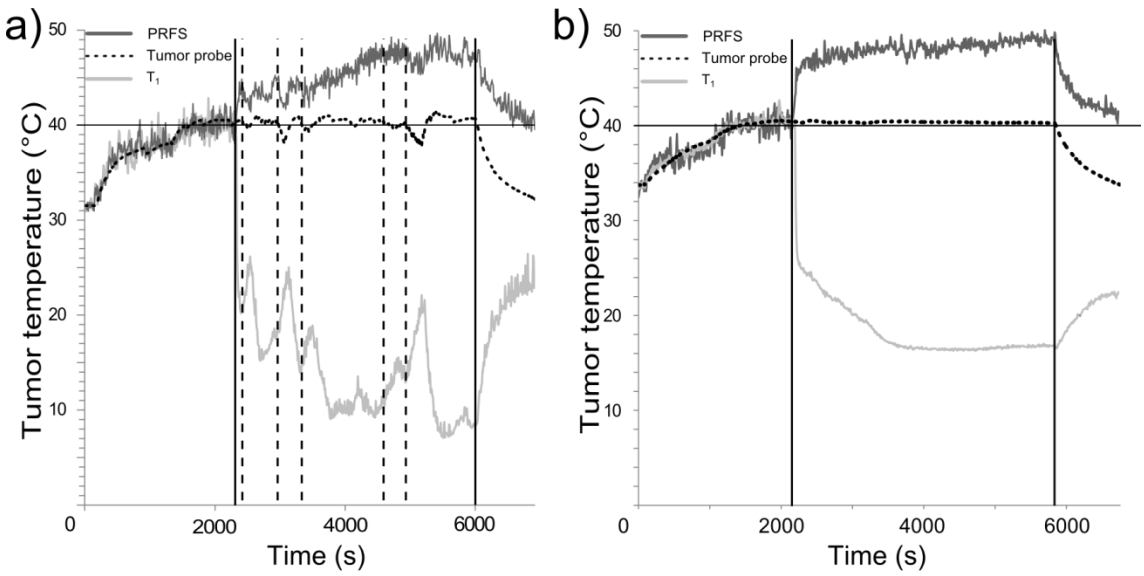

Figure 25: a) Dynamic temperature curves for experiment N62. Temperature changes measured by probe were caused by temporal malfunction of the laser. b) Dynamic temperature curves for experiment N84. Vertical solid black lines shows the injection and the end of heating while the dashed black lines mark temperature changes from above to below 40 °C.

4.3.4 HPLC DOX CONCENTRATION

HPLC analysis was used as reference for drug dose painting and was performed successfully in the 18 tumor samples. The mean DOX concentration of heated tumors in group A was 10.6 ± 2.6 ng/mg, and 1.2 ±0.4 ng/mg for unheated tumors in group A. Tumors in the control group B resulted in a DOX value of 2.1 ± 1.1 ng/mg. Comparing HT-induced drug delivery, the mean DOX ratio for heated to unheated tumors in Group A was 9.4 ± 2.9 (5.3 – 13.1). For group B, the mean ratio was 1.3 (1.1 and 1.6). DOX concentrations by HPLC of the two halves in the bisected tumors were juxtaposed and were seen as indicators of intratumoral homogeneity of DOX release. The mean ratio between the lateral and the medial DOX concentration was 1.9 ± 1.1 for the heated tumors in group A and 1.1 (1.0 and 1.3) for the unheated tumors of group B. This indicates a higher DOX concentration in tumor tissue, which is closer to the results obtained using the laser applicator.

4.3.5 CHEMODOSIMETRY

The overall aim of the study was to facilitate accurate prediction of drug concentration in tissue with MR-imaging. Static measured T_1 values (Table 9), phase difference, and parameters containing dynamic information were generated from dynamic tissue curves (Figure 26) and static measurements.

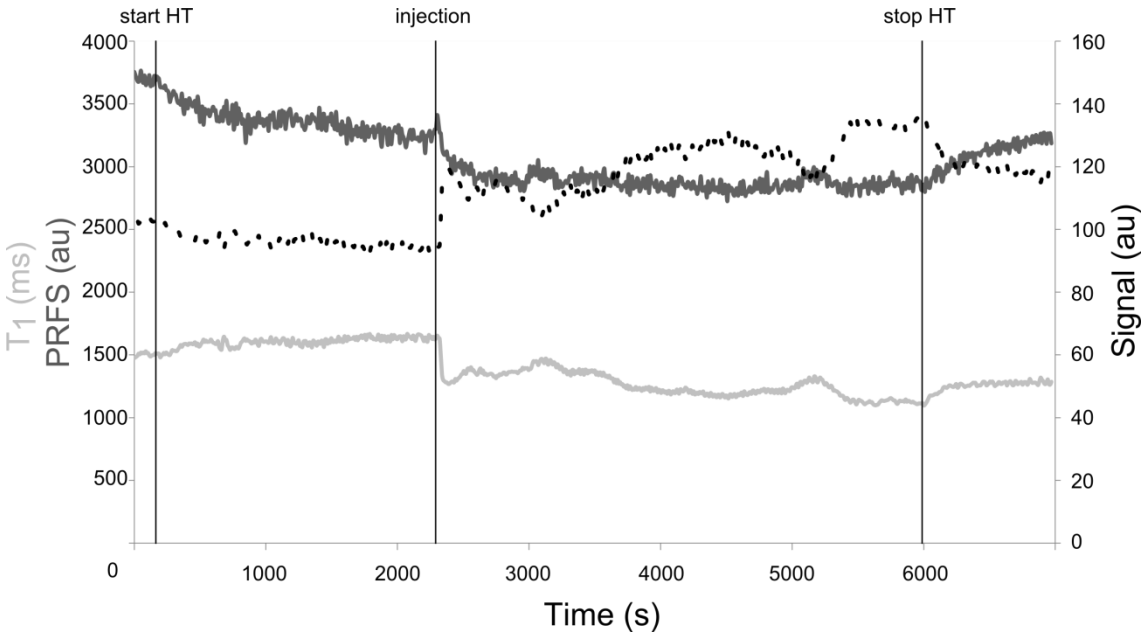

Figure 26: Representative dynamic tissue curves for T_1, PRFS and signal enhancement for the heated tumor. From these tissue curves, MR parameters were extracted for further investigation.

Correlation coefficients between HPLC DOX concentration and MRI parameters were analyzed and are shown in table 12. The AUC of the dynamic phase (Phase_AUC) and the relative T_1 change showed the highest correlation with the HPLC DOX-concentration, whereas the relative T_1 time difference (T_1_7FA_rel) resulted in the lowest correlation. Corresponding correlation of the medial, lateral and unheated tumor to HPLC DOX concentration is shown in supplementary table 7, where the r-values are of the same order of magnitude as the data in table 12.

With these data, linear regressions (y = m * x +a) were calculated and used for drug dose painting, and the calculated DOX concentrations were analyzed by a modified Bland Altman Plot (Fig. 22 f) afterwards.

linear regression of MRI Parameter and HPLC DOX concentration					
regression with HPLC DOX-concentration and		Slope (m)	Intercept (a) [ng/mg]	R	p
static data	T_1_1FA_total_abs [(ng/mg)/ms]	-27.1	-352.7	-0.648	< 0.0005
	T_1_1FA_total_rel [(ng/mg)/%]	-2.2	-21.4	-0.764	0.004
	T_1_1FA_treatment_abs [(ng/mg)/ms]	-42.5	-341.3	-0.819	0.001
	T_1_1FA_treatment_rel [(ng/mg)/%]	-2.7	-21.6	-0.857	0.023
	T_1_7FA_abs [(ng/mg)/ms]	-19.9	-417.2	-0.496	0.287
	T_1_7FA_rel [(ng/mg)/%]	-1.5	-26.0	-0.335	0.145
	Phase_diff [(ng/mg)/rad]	-0.070	0.039	-0.847	0.001
dynamic data	Phase_AUC [(ng/mg)/(rad*s)]	-97.4	-329.0	-0.856	< 0.0005
	T_1_1FA_AUC_rel [(ng/mg)/(%*s)]	$9.6*10^{-3}$	$-61.6*10^{-3}$	-0.842	0.001
	T_1_1FA_AUC_abs [(ng/mg)/(ms*s)]	$-1.5*10^{-5}$	$-8.8*10^{-5}$	-0.793	0.002

Table 12: Data for linear regressions of HPLC DOX with different MRI parameters with their corresponding r-values as correlation factor and their p-values (0.000 → p<0.0005). DOX concentrations and ROI values of whole tumors were used for correlation.

With this information and the measured HPLC DOX-concentration, MRI DOX-concentration maps were calculated pixel-by-pixel with equation (32):

$$\boldsymbol{D_{MRI} = m * P_{MRI} + a}$$

32

were D_{MRI} is the DOX concentration in ng/mg calculated with the corresponding MRI Parameter P_{MRI}, slope (m) and intercept (a) from table 12.

As a control, the calculated DOX concentrations were compared to the HPLC-DOX concentration for each region, and then fitted with a linear model (Figure 28, table 13). . The AUC of the relative dynamic T_1 time change has a slope nearest to one, and the lowest intercept difference from zero, while the relative T_1 time difference has the highest slope and the highest intercept difference from zero. Linear regression and corresponding Bland Altman plots are shown in figure 28 for HPLC and MRI DOX-concentration. The smallest reproducibility coefficient (RPC = 1.96*SD of mean error) was found for the AUC of the dynamic phase and for the relative T_1 difference before and after treatment, measured with 1 FA with 5.6 ng/mg. The highest RPC was found for the relative and absolute T_1 difference measured before and after heating with 7 FA, recorded at 13.7 ng/mg and 17.0 ng/mg, respectively.

As an internal control, the results of bisected tumors were analyzed as well (supplement table. 10). The calculated DOX concentrations corresponding to the bisected tumors were comparable to those of the whole tumors (supplement table 11). Additionally, DOX concentration of unheated muscle was calculated and compared to the muscle DOX concentration gained by experiments from chapter 3 (figure 27). Data used, are shown in supplementary table 8 and 9.

Linear regression of MRI calculated DOX and HPLC DOX concentration					
regression with HPLC DOX and MRI DOX of		Slope	Intercept	r^2	**RPC (ng/mg)**
static data	T_1_1FA_treatment_rel	0.69	1.46	0.818	**5.6**
	T_1_1FA_treatment_abs	0.66	1.27	0.765	**6.5**
	T_1_1FA_total_rel	0.70	0.51	0.658	**7.8**
	T_1_1FA_total_abs	0.53	1.16	0.550	**10.9**
	T_1_7FA_rel	0.46	1.53	0.405	**13.7**
	T_1_7FA_abs	0.37	1.92	0.377	**17.0**
	Phase_diff	0.69	1.01	0.760	**5.8**
dynamic data	Phase_AUC	0.72	1.09	0.813	**5.6**
	T_1_1FA_AUC_rel	0.69	1.16	0.772	**5.9**
	T_1_1FA_AUC_abs	0.58	1.16	0.721	**7.1**

Table 13: Linear regression for measured vs. calculated DOX values for every ROI in [(ng/mg)/(ng/mg)]. Data were generated with data from table 12. The RPC factor was generated from the Bland Altman plot.

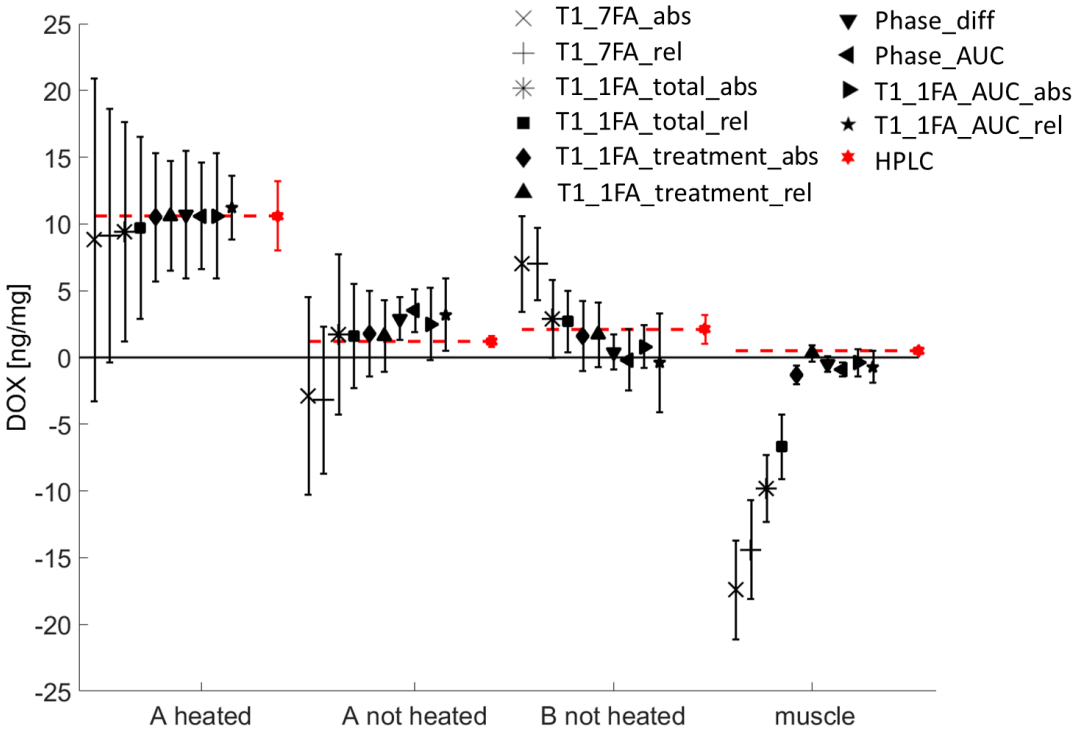

Figure 27: Mean DOX concentration with standard deviation determined by MRI parameters in group A and B compared to DOX concentration determined by HPLC. DOX concentration in muscle was determined in preceding experiments (chapter 3).

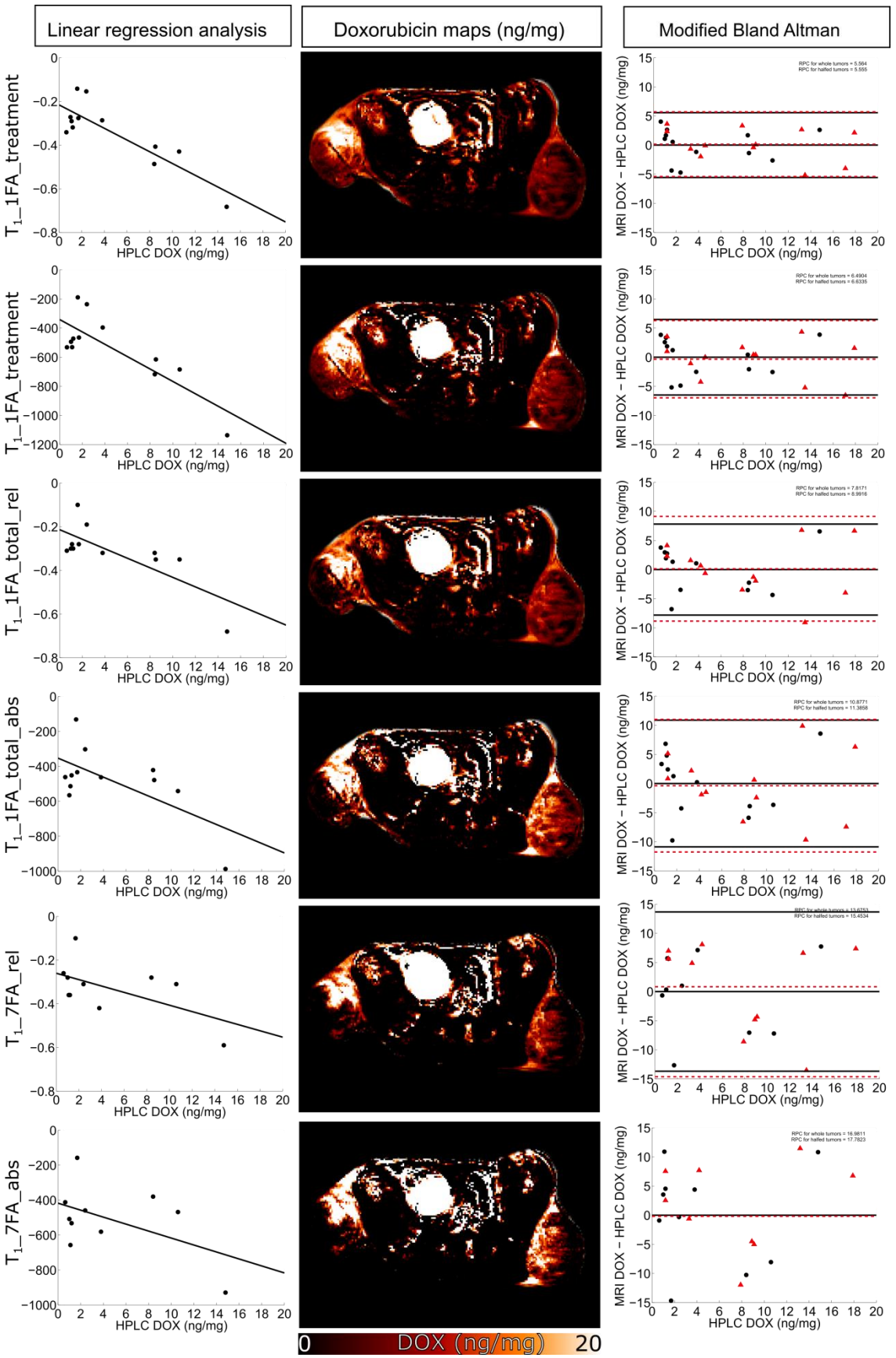

Figure 28-1: Left: Scatterplots for whole tumors HPLC tissue DOX concentration [ng/mg] compared to the extracted MRI parameter with linear regression. Middle: Representative image with pixelwise calculated DOX concentration [ng/mg] for N62. Right: Bland Altman plot for HPLC DOX concentration [ng/mg] compared to the MRI DOX-concentration [ng/mg] for whole tumors (black, solid line, dots) and lateral and medial tumor parts. (red, dashed, triangle).

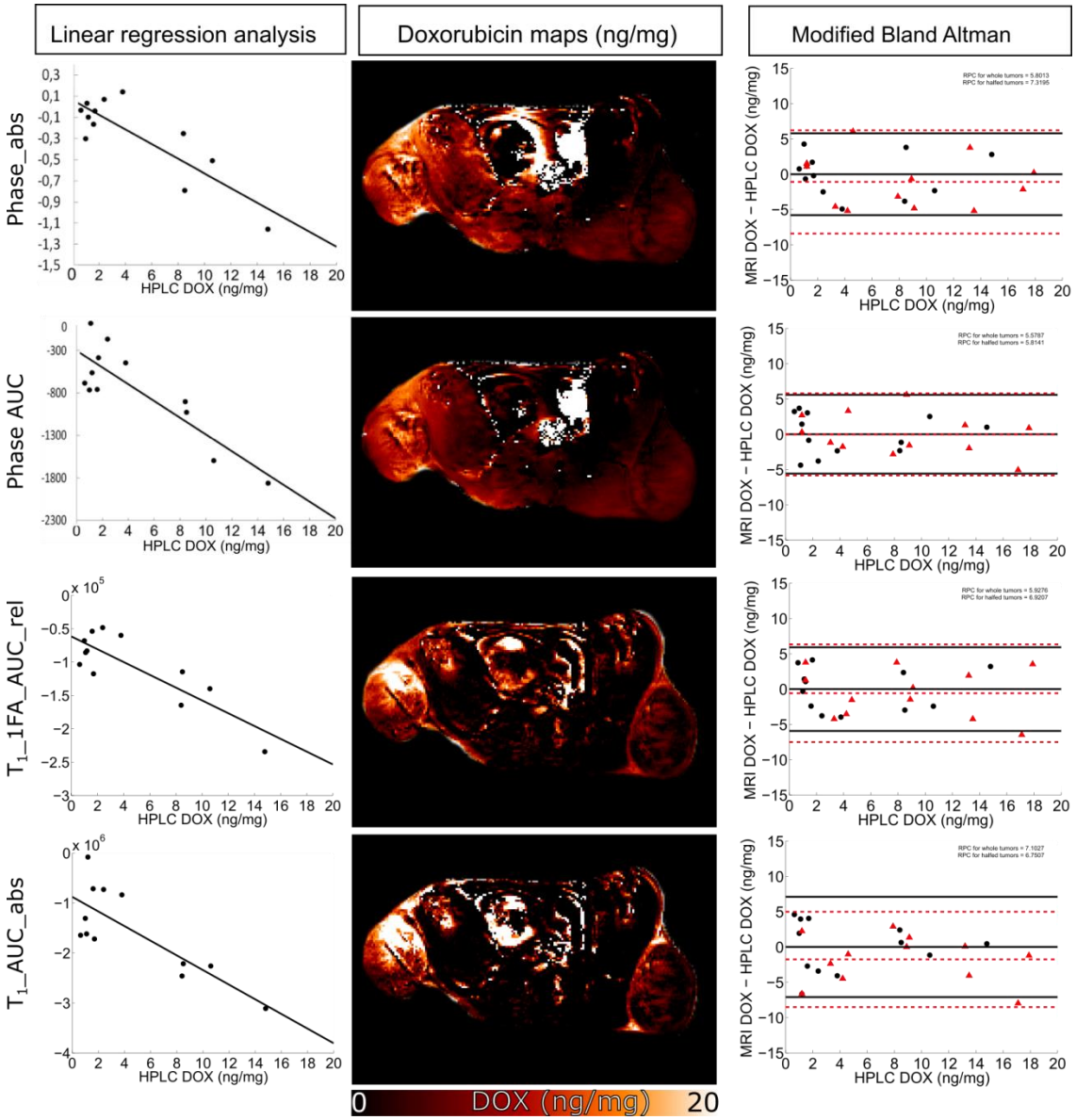

Figure 28-2: As described in figure 28-1.

4.4 DISCUSSION

Thermosensitive liposomes supply an advancement towards temperature-induced targeted chemotherapy. The encapsulated drug is protected against metabolism and interaction in the human body, and can reach the target tissue easily. Several types of chemotherapeutics, such as doxorubicin, gemcitabine and miltefosine [20,119] as well as different MR contrast agents [88], can currently be loaded into the liposomes. This method contributes to targeted chemotherapeutic therapy, while CA-release from the liposomes with MR-imaging can also be characterized by different MRI parameters.

In this work, various MR parameters are analyzed to determine their potential use for drug dose painting. For this purpose, static and dynamic tissue parameters were compared to their corresponding drug concentration. To develop a system for clinical use, it is necessary to minimize patient stress, so well-tolerated and clinical approved components must be used in injections. In this study, FDA-approved gadolinium-based MRI-CA and FDA-approved chemotherapeutical drug doxorubicin were encapsulated in TSL. The administered DOX-dosage (2 mg/kg) was selected according to the usual dose for cancer treatment in humans [34]. The applied dosage of CA is a well-tolerated dose used for clinical MR-imaging [120]. All lipids used in this study were declared safe in the **A**natomical **T**herapeutic **C**hemical classification system ATC

4.4.1 DRUG RELEASE

Drug delivery after injection of mixed DOX- and CA-TSL during laser-induced mild HT was highly effective, as evidenced by the enhanced DOX release in the heated tumors. This result was in accordance with the findings in chapter 3 using the same DOX-TSL and experimental setup, but with the addition of three temperature probes in the tumor. As the heating method and DOX-TSL were the same, these previous data were assumed directly comparable, thus the HPLC DOX concentration in muscle was used to compare with MRI-determined DOX concentration in muscle tissue.

4.4.2 HEATING OF THE TUMOR

As shown in chapter 3.3.2, the laser heating device provides a relatively homogeneous heat pattern with no signs of long term side effects in the subcutaneous tumor HT. In contrast to the experimental setup used for validation of the laser light applicator, only one temperature probe was used. The tumor probe was implanted in the medial third of the tumor, which guaranteed measurement of the temperature in the tumor volume at the

minimum temperature level or above (see chapter 3). To reach a minimum temperature of 40 °C in the whole tumor, target temperature was chosen depending on probe position.

Mean tumor probe temperatures differed from the target temperature by less than or equal to - 0.2 °C, which provides a sufficient heating expectation of less than half a millimeter. This was considered to be an adequate heating. For one experiment (N62), a laser malfunction caused a variation in temperature (40.2 ± 0.7 °C), which resulted in a temporary tumor temperature less than 40 °C. This was accepted because chemotherapy should also work on tumors that are not adequately heated.

Temperature determined with one tumor probe for the whole heating volume is questionable if inhomogeneities in the temperature distribution are present. Therefore, MRI temperature measurements by T_1, or with PRFS, were performed to examine tumor temperature in the whole tumor.

MRI thermometry is capable of mapping temperature change. The results demonstrated that there was a temperature decrease from the tumor part near the laser light applicator to the opposite side.

4.4.3 MRI MEASUREMENTS

T_1 quantification

Since, a rapid CA release from the TSL was assumed to be a key mechanism, a fast gradient echo image sequence was applied.

The T_1 time difference between the VFA method with one and with seven flip angles is less than 36 ms ± 180 ms (SD). Furthermore, measured T_1-time for muscle tissue at body temperature (1377 ms ± 79 ms (SD)) corroborates human muscle tissue data in the literature (1412 ms ± 13 ms (SD)) [121].

For T_1 calculation, a source of a systematic error was neglected in order to realize a quick acquisition time. For the dynamic VFA-method, it was assumed that T_2* and M_0 remain constant over the whole treatment time to permit the use of only one flip angle during the dynamic scan, which accelerated the acquisition rate. To establish whether this assumption is justified, a measurement was performed after the treatment with the entire set of all flip angles as acquired before injection. The T_1 value obtained in this manner was compared to the T_1-time calculated from the last acquired time point with one flip angle and the M_0 from the previous measurement. This resulted in an error of -36 ms ± 144 ms (SD) in T_1 quantification. Therefore, in agreement with Dietrich et al. [122]—where a relevant

error in T_1 measurement only occurs for higher CA concentrations—the T_2* effect and changes of M_0 can be neglected.

A limitation of the flip angle correction used in this work is that it does not apply to the whole dataset, for example, wherever the signal was bad due to decreased receiver coil sensitivity for the outer regions of the FOV and wherever there was a resulting bad signal to noise ratio. This phenomenon had no effect for evaluation because the tumor slices were located in the center of the FOV.

Temperature measurement

For an accurate and precise temperature measurement with the T_1 relaxation time, a tissue-dependent factor is necessary. This factor was calculated for the tumor tissue with the data from all of the animals. Temperature change measurements by MRI before injection were possible with an accuracy of ± 0.7 °C ± 1.5 °C. After injection, MRI temperature measurement based on T_1 depicted a significant deviation from the temperature detected by the fiber-optic probe. This was expected for the T_1-temperature measurement because of the CA-induced T_1 change. Therefore, a temperature change measurement with the T_1 relaxation time in combination with liposomes-encapsulated CA-is not possible. On the other hand, when exceeding the phase transition temperature, the T_1 time changes rapidly. This data could be used for absolute temperature measurements and is observable in experiment N62 (Figure 25), in which exceeding or falling below the T_m leads to a significant change in the longitudinal relaxation time. This effect changes the MRI-signal when exceeding the phase transition temperature and was illustrated in vivo by Peller [74]. This works as long as CA-TSL are present and CA is not completely released. The limitation of this method is that only one temperature level can be measured.

Phase measurements are always affected by phase drift during long lasting, repeated measurements. This phase drift was corrected with a reference in less perfused muscle tissue, where a low CA enhancement is expected, promising the lowest error for drift correction after injection. Fat tissue is more suitable for drift correction because of its low perfusion and absence of hydrogen bonding that results in insensitivity to temperature change [123]; however, there was insufficient available adipose tissue for drift correction. Due to the restricted volume in the receiver coil, no external phantom for drift correction could be used. However, the high accuracy (-0.21 °C) of PRFS temperature measurements—before injection—shows that the drift correction aided by a reference tissue was sufficient.

Changes in T_1 and T_2 time should have no effect [124] on temperature measurement with the PRFS method, but the results reveal a mismatch relative to the invasive temperature

measurement after injection. This effect was also described by Hijnen in 2013 [107]. This discrepancy cannot be explained by relaxation time change, because normally the PRFS method is based on change in the shielding constant of the H-nucleus and a change in relaxation time should have no effect on the phase shift [125]. The deviation in temperature measurements assumed to be caused by a susceptibility change. The temperature sensitivity of the susceptibility can be neglected for temperature measurement normally [63], but the susceptibility change caused by CA-TSL and free CA is much higher. These CA-induced susceptibility fluctuations influence the local magnetic field around the nucleus, resulting in a change of Larmor frequency, and thus in an error with the PRFS temperature. Therefore, an accurate temperature measurement for mild HT with T_1 time change or with the PRFS method is was not possible after injection of CA-TSL.

4.4.4 CHEMODOSIMETRY

The main objective of this study was to estimate drug concentration in target tissues using MRI parameters. Until now, the parameter of choice for drug dose painting with TSL and mild HT was T_1. The preceding studies compared T_1 maps acquired before and after HT for chemodosimetry [101,126]. In this study, T_1- and PRFS-based data were used, which were acquired before and after (static data) as well as during the treatment (dynamic data). One challenge for this work was the accurate placement of the ROIs corresponding to the excised tumor parts for the heated tumor and are a potential source of error

For drug dose painting, the CA concentration was not calculated. On one hand there is the linear correlation between relative T_1 change and CA concentration in a defined range of CA concentration, and on the other hand there is a tissue- and temperature-dependent relaxivity of gadolinium-based CA [127]. Thus, a precise calculation of CA-concentration was not possible because data, such as the r_1 for every temperature and the tumor tissue, were not available.

It is assumed that a linear correlation between relative T_1 change and CA concentration—a nonlinear correlation for absolute T_1 change—may explain why static and dynamic change for absolute T_1 parameters has a lower correlation coefficient to the HPLC DOX concentration compared to the relative T_1 change parameters.

Additionally, the PRFS measurement was used for drug dose painting. The hypothesis was that this parameter facilitates a better prediction of the drug concentration in the tumor compared to T_1-quantification because of TSL's characteristics. This means that water exchanges through the membrane as the temperature rises. Above T_m, the drug is released. As mentioned before, the water exchange induces a T_1-change without drug release. Furthermore, the PRFS method was used by Korporaal et al. in 2011 to quantify contrast

agent concentration and to obtain the concentration of CA in an arterial input function for perfusion measurement [128]. Korporaal determined that the phase change is linear to the amount of MR-CA, even for high concentrations.

Temperature change after reaching the target temperature was neglected in this paper because the temperature in the tumor was relatively stable. A temperature change of ± 1 °C over the whole treatment time (60min) would generate a calculated error of ± 0.9 $^{ng}/_{mg}$ for DOX quantification, which is minimal, compared to the RPC, and therefore was assumed acceptable.

The calculated drug concentration in the present work evidences a better correlation for dynamic MRI acquisition (AUC of T1-change or Phase-change) compared to the static data, whereas the AUC for relative T_1 change is slightly better than the PRFS method. On the other hand, the PRFS method does not require additional B1 correction measurements, which reduces total scan time. This would be beneficial in clinical use. To simultaneously measure T_1 and phase change, sequence parameters were adapted to provide sufficient quantification for both parameters. Drug dose painting could be improved by selecting a specific MRI marker with optimized sequence parameters that are modified especially for T_1 time measurements (shorter TE, longer TR) or for phase measurement (longer TE). For phase measurements, a longer TE generates a larger phase change when all other sequence parameters are held constant. This larger phase change supplies a higher SNR and thus better drug dose painting and temperature sensitivity, whereas for T_1-time measurement, a shorter TE, and a longer TR lead to a higher SNR, and thus to a better drug dose painting and temperature sensitivity as well.

In the literature, the possibility of in vivo monitoring for drug release is calculated qualitatively, but only a few studies have performed quantitative drug dose painting [28,30,31,101]. In 2007, Viglianti et al. and Ponce et al. demonstrated that drug dose painting was feasible with MRI. They used a $MnSO_4$-doxorubicin TSL in combination with mild HT [26,29,101]. In these studies, an implanted water tube passing through the tumor induced HT. Tissue probes were taken, analyzed by HPLC, and correlated to the CA uptake after the treatment. Viglianti et al. revealed a linear regression between the CA-uptake calculated DOX concentration in the tumor and the tissue DOX-concentration of 0.86 ± 0.48 (SD) $\left(\frac{ng/mg}{ng/mg}\right)$, and an intercept of -0.01 ± 10.05 (SD) (ng/mg) in 2006 [29]. They used only the CA enhancement calculated from two T_1-maps, one acquired before and one acquired after heating. Ponce recorded a T_1 map every 90 s in order to calculate drug concentration for the whole tumor. The MRI DOX concentration at the last time point

was compared to an HPLC measurement, which demonstrated no significant difference. There was no further statistical analysis reported from Ponce et al..

It is assumed that a drug dose painting based on T_1 acquired at only two time points before and after HT neglects processes that occur during the treatment, such as washout of CA from the tissue, while drugs like DOX exhibit rapid intercalation with DNA and are permanently built into the cell. This might be compensated for by Mn^{2+}, which binds to DOX and prompts a DOX-CA relationship. This binding reduces the error of a washout of the MRI-CA, and thus can be beneficial for drug dose painting when CA and DOX are combined in one TSL. But there is also an interaction of Mn^{2+} with the head groups of the liposomes that reduce the drug retention capability of the TSL [129]. Furthermore, Mn^{2+} is toxic and thus cannot be used in patients.

For further studies, it has to be considered if the high temporal resolution used in this work is necessary. For example, a higher SNR could be achieved with longer acquisition time and a high temporal resolution as it is needed for perfusion is not necessary due to the fact that no arterial input function needs to be acquired.

For a clinical application, it has to be investigated if drug dose painting with these imaging methods is possible. Thus, it is not possible to inject the CA- and DOX-TSL as a bolus because of the high injection volume, which makes an infusion necessary. It also has to be investigated if this type of chemodosimetry is possible for different chemotherapeutics.

4.4.5 LIMITATIONS

Dynamic T_1 mapping with one FA is affected by neglecting the T_2* effect of CA. This error increases with increasing CA concentration and with decreasing FA as described by Dietrich et al. [122]. Therefore, without T_2* correction the calculated T_1 values were systematically too high. The estimated maximum error of 3 % for the setup used in this work can interfere with the drug dose painting.

During a long lasting MR-measurement, a phase drift can occur, which has to be compensated for. In this work an internal muscle reference was used instead of an external reference due to a lack of space. To exclude a possible error using internal references because of contrast agent or movement, external reference phantoms may be an advantage for PRFS measurements.

MR temperature measurements with CA-TSL depend on the setting of the pulse sequences and are discussed in the literature. Fossheim et al. [73] reports susceptibility effects while investigating *in vitro* TSL encapsulating Gd-DTPA-BMA. Apart from the type of CA, such

susceptibility depends on the size of the liposomes and the susceptibility difference between the vesicle interior and exterior [130]. This suggests that MR thermometry based on the chemical shift of the proton resonance frequency, which is determined by phase changes, is sensitive to CA-TSL injection and heat induced release of CA from TSL. Hijnen et al [131] considered this as potentially relevant to MR thermometry for HIFU guidance in combination with co-encapsulated gadolinium-based CA, although such effects were not reported in earlier studies [109]. The same group verified an effect in phantom and *in vivo* muscle tissue [107]. Therefore, temperature measurements using phase shift must be verified in the presence of CA-TSL for every experimental setting.

Absolute temperature measurements are especially necessary for subcutaneous tumors because of the difference between body and tumor temperature and—as noted in chapter 3.3—a possible temperature gradient before heating.

5. CONCLUSION

Drug delivery through the combination of $DPPG_2$-TSL encapsulating DOX and the new laser applicator in a clinical MRI setting was highly effective when a minimum temperature of 40°C was achieved in the targeted tumor; these conditions resulted in an almost 10-fold higher DOX tissue concentration compared to the unheated tumor.

For visualization, a new approach was tested using a mixture of $DPPG_2$-TSL encapsulating either DOX or CA showing that this is a promising method for following HT-triggered local DOX delivery with MRI. This approach has several advantages over the application of TSL with co-encapsulated drug and CA. Firstly, complexity in development of single compound formulations is significantly reduced. Secondly, independent dosing of drug and CA is facilitated *in vivo*, whereas co-encapsulation allows application with only a fixed dose-ratio. Finally, other formulations containing gemcitabine [11], such as $DPPG_2$-TSL, could be easily investigated in MRI by adding CA-TSL.

Besides determining T_1 parameter maps at specific time points, as preferred in literature, other MRI parameters were also identified as promising surrogate marker for DOX accumulation in tumor tissue. Phase-based MR thermometry was severely affected by the presence of CA-TSL; however, for the first time, this CA-TSL-related phase change was demonstrated to be suitable for the assessment of DOX concentration. Tumor temperature was stable during HT, and MRI surrogate markers acquired during HT were preferable over the previously preferred change in T_1 possible using TSL with co-encapsulated drug and CA.

MRI-derived parameter maps of DOX concentration demonstrated local differences, indicating that visualization of CA released from TSL could be usable for targeting HT to a specific tissue volume. This concept must be investigated in more detail in future studies.

In conclusion, promising MRI surrogate parameters were also identified for the assessment of DOX tissue concentration when using a mixture of CA-TSL and DOX-TSL.

6. SUPPLEMENT

6.1 CHEMICALS

The phospholipids 1,2-dipalmitoyl-*sn*-glycero-3-phosphocholine (DPPC) and 1,2-distearoyl-*sn*-glycero-3-phosphocholine (DSPC) were obtained from Corden Pharma Switzerland LLC (Liestal, Switzerland). 1,2-distearoyl-*sn*-glycero-3-phosphodiglycerol ($DPPG_2$) was synthesized as described above [40]. DOX was purchased from Sigma Aldrich GmbH (Munich, Germany) and Gd-DTPA-BMA (Omniscan™) was from GE Healthcare Buchler GmbH & Co. KG (Braunschweig, Germany). The FCS came from Biochrom AG (Berlin, Germany). All other chemicals were either from Carl Roth GmbH (Karlsruhe, Germany) or from Sigma Aldrich GmbH (Munich, Germany). Purified, deionized water generated with the Milli-Q Advantage A10 system (Merck Millipore, Billerica, MA, USA) was used in all experiments.

6.2 COMPARISON AND VALIDATION OF HEATING METHODS

6.2.1 CHARACTERIZATION OF LIPOSOMES

Lipid (mM)	DOX (mM)	DOX/Lipid (mol/mol)	z average (nm)	PDI	Zeta potential (mV)	$DPPG_2$ (%)	Lyso-PC (%)
21.6	3.0	0.14	104	0.11	-24.7	30.5	0.1
(± 4.6)	(± 0.6)	(± 0.02)	(± 10)	(± 0.06)	(± 3.7)	(± 6.1)	(± 0.2)

Supplementary table 1: Characterization of DPPC/DSPC/$DPPG_2$ 50/20/30 (mol/mol) TSL ($DPPG_2$-TSL) formulations encapsulating DOX. Four independent preparations have been used. The molar content of $DPPG_2$ and Lyso-PC was quantified with thin layer chromatography. The standard deviation is given in parentheses. PDI: polydispersity index.

Temperature (°C)	k_{DOX} (10^{-4} s^{-1})	
	HN buffer	FCS
37	0.2 (0.787)	0.9 (0.895)
38	0.3 (0.975)	3.2 (0.917)
39	0,7 (0.987)	10.0 (0.992)
40	3.3 (0.973)	51.8 (0.998)
41	30.5 (0.953)	73.0 (0.895)
42	53.0 (0.990)	105.7 (0.954)

Supplementary table 2: Release kinetics of DOX from DPPC/DSPC/$DPPG_2$ 50/20/30 (mol/mol) TSL ($DPPG_2$-TSL) measured with fluorescence spectroscopy, as described previously [18]. Calculated DOX release rate constants k_{DOX} from measurements performed in (A) 20 mM HEPES, 150 mM NaCl (HN buffer), pH 7.4 (n = 3), and (B) FCS (n = 3). The coefficient of determination (R2) is given in parentheses.

6.2.2 SUPPLEMENTARY DATA

Supplementary figure 1: Transmission curve for color filter "RED" (kindly provided by Optich PL 2000, Photonic Optische Geräte GmbH & Co. KG, Austria)

Experiment			DOX concentration [ng/mg]			
			lateral tumor part	medial tumor part	whole tumor	reference tumor
Lamp	large	N20	18.9	7.0	14.2	0.8
		N23	23.4	2.0	13.5	1.0
		V33	28.0	14.6	18.7	1.3
	small	V23	23.2	23.4	23.3	2.0
		V36	24.6	21.6	22.6	1.2
		V37	24.8	20.9	23.4	1.0
Laser	large	N44	9.7	5.1	7.0	0.9
		V27	2.8	7.9	6.1	0.6
		V39	22.1	14.5	18	1.0
	small	N47	31.6	14.2	23.3	0.9
		V21	22.3	13.3	19.7	1.1
		V29	19.4	10.9	14.8	1.8
Water bath	large	V26	3.6	5.7	4.5	0.7
		V32	5.4	4.6	4.8	1.6
		V35	3.2	5.2	4.3	1.0
	small	V24	5.3	7.2	6.1	1.6
		V28	9.2	9.3	9.3	1.7
		V38	20.9	27.0	24.5	1.0

Supplementary table 3: HPLC DOX-concentration for all experiments and tumor parts. DOX concentration for the whole tumor was subjected to a weighted calculation by weight of tumor parts.

6.2.3 *TECHNICAL DRAWINGS*

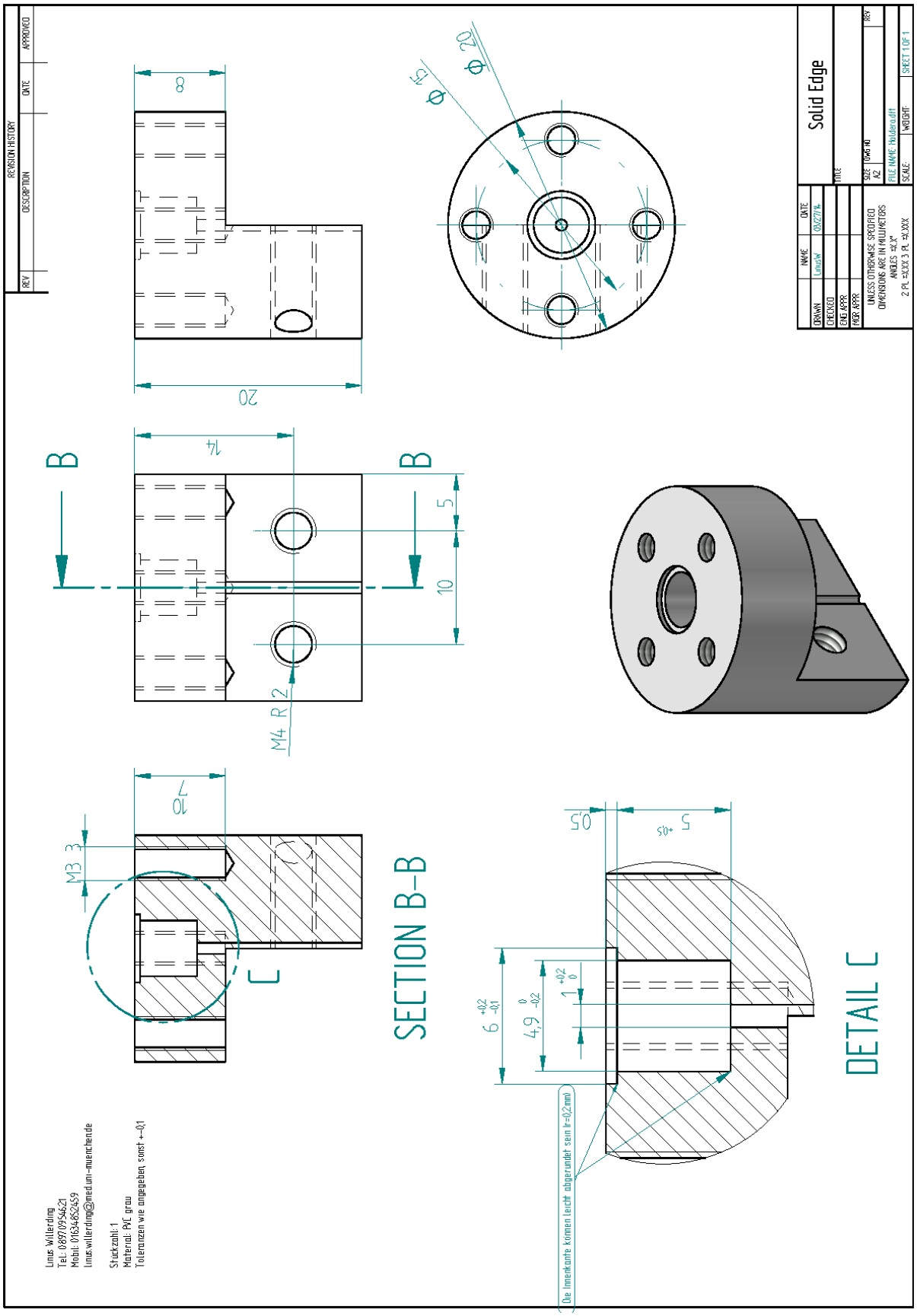

Supplementary figure 2: Lensholder

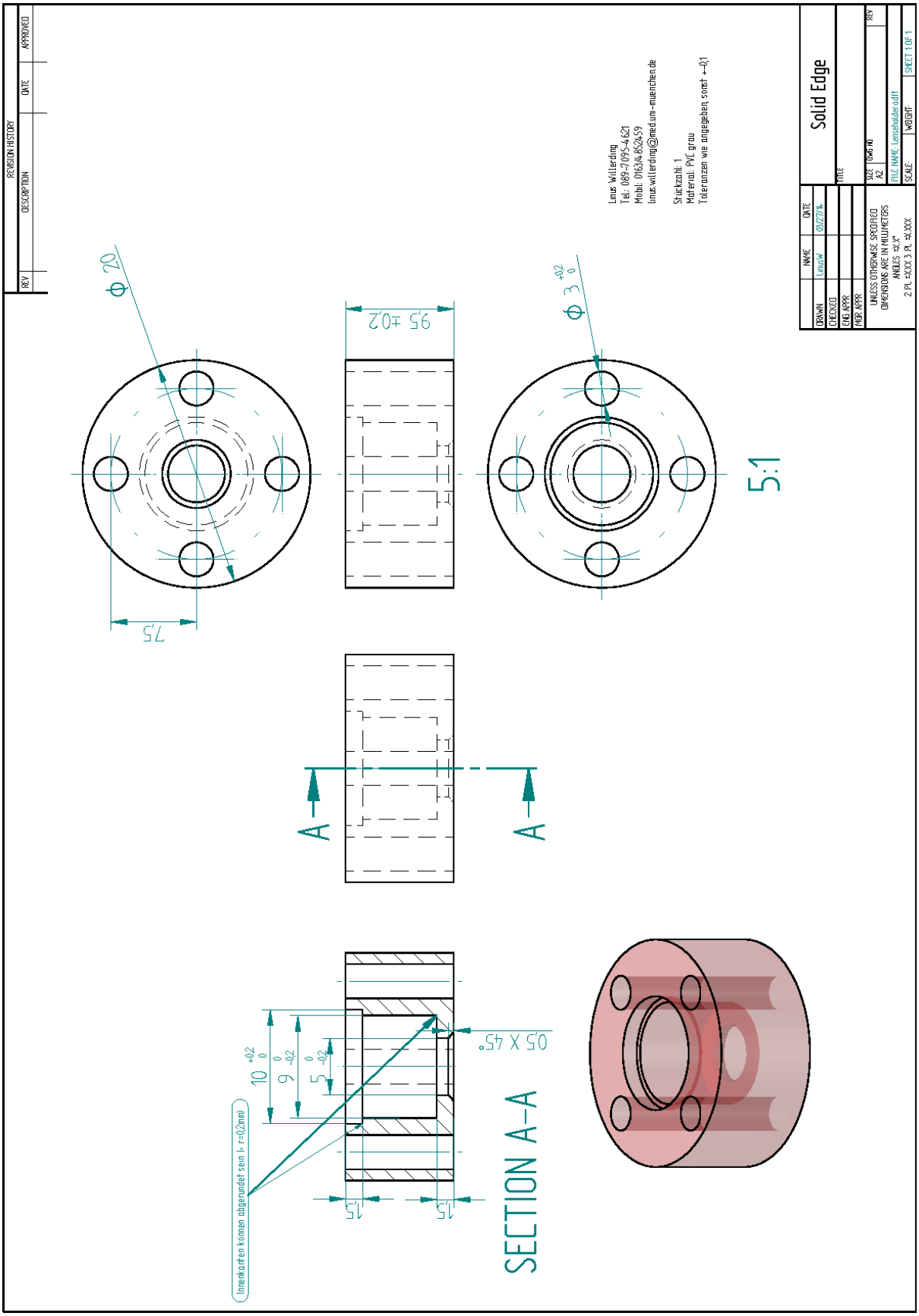

Supplementary figure 3: Lensholder disc 1

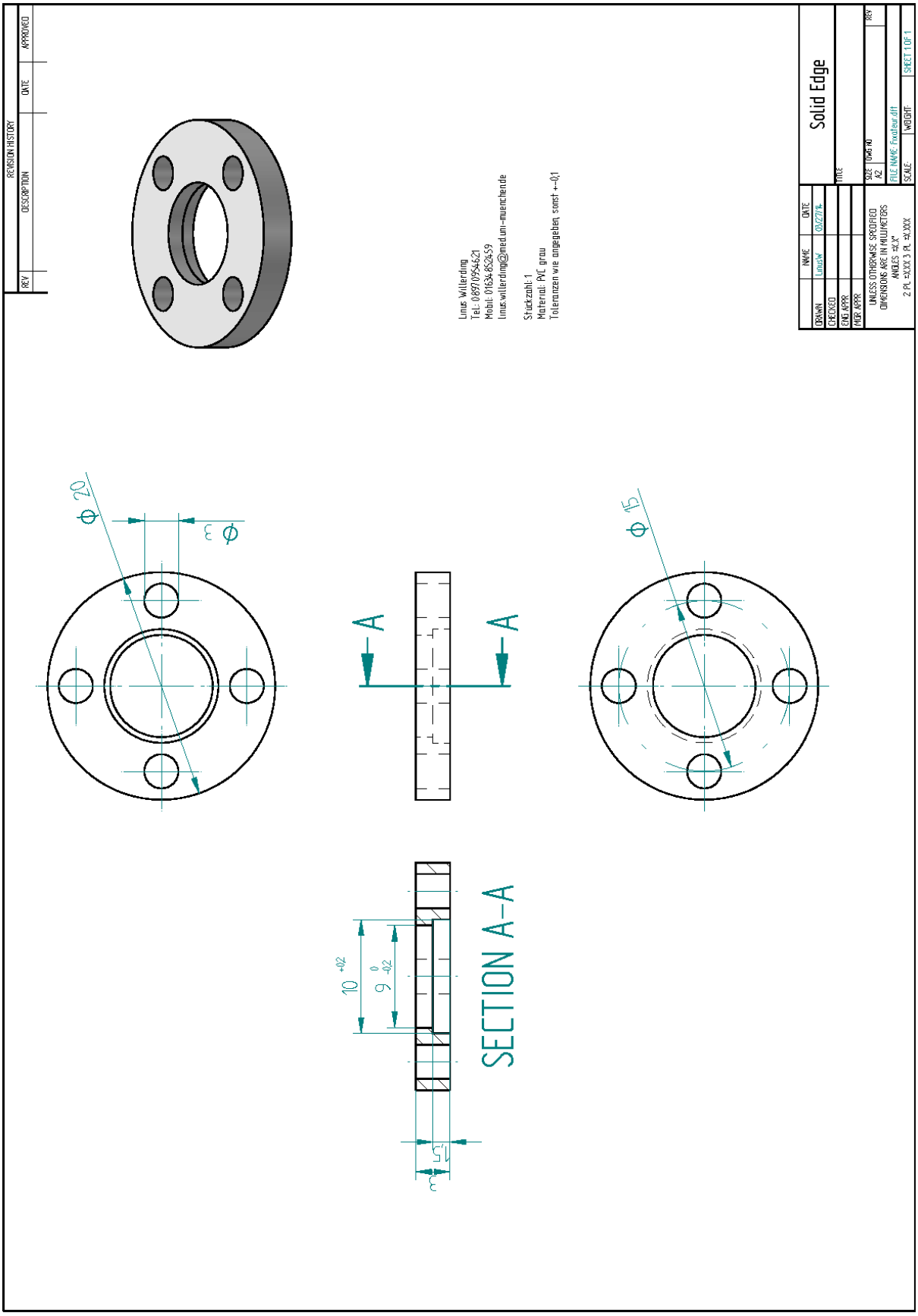

Supplementary figure 4: Lensholder disc 2

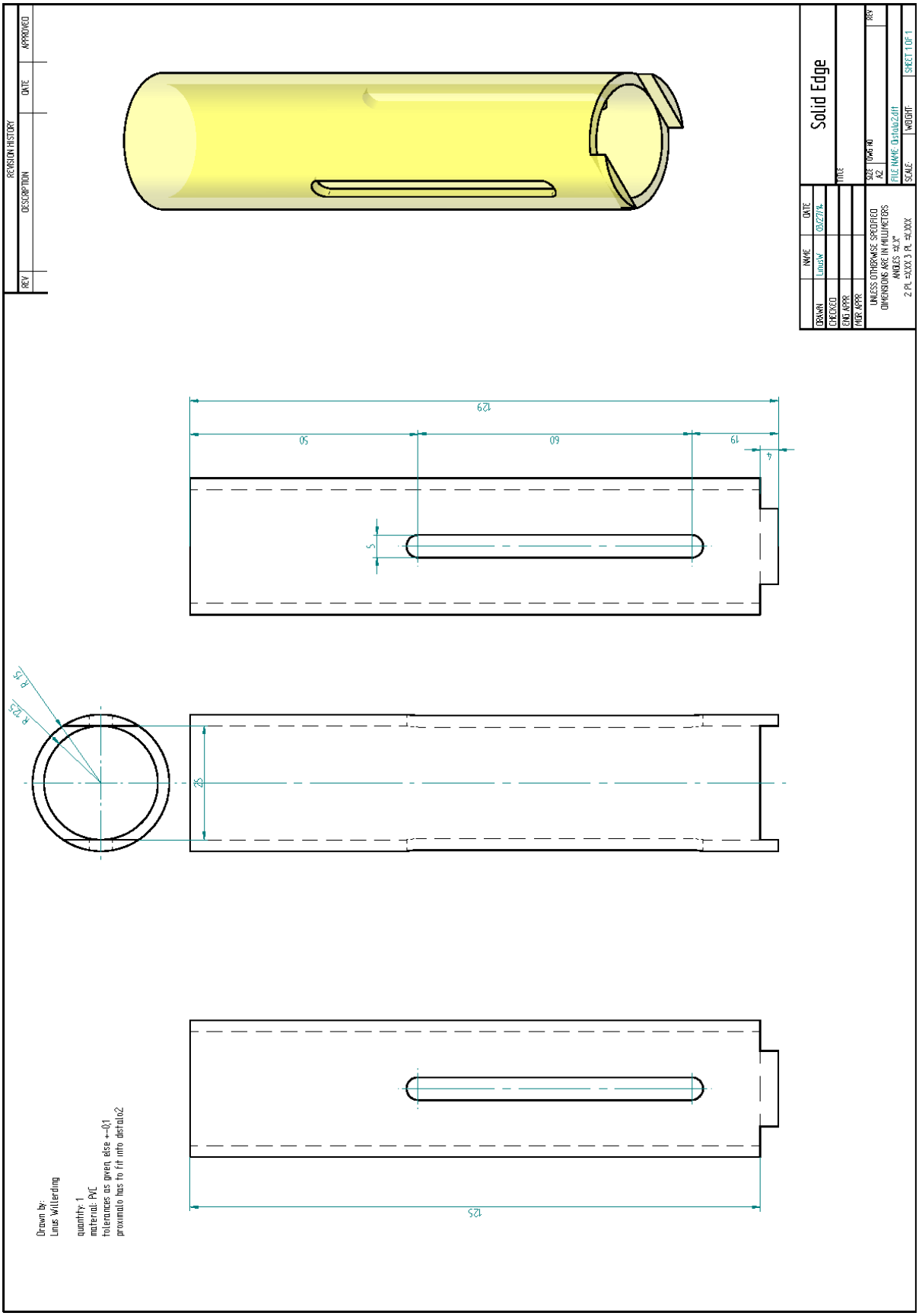

Supplementary figure 5: Outer tube

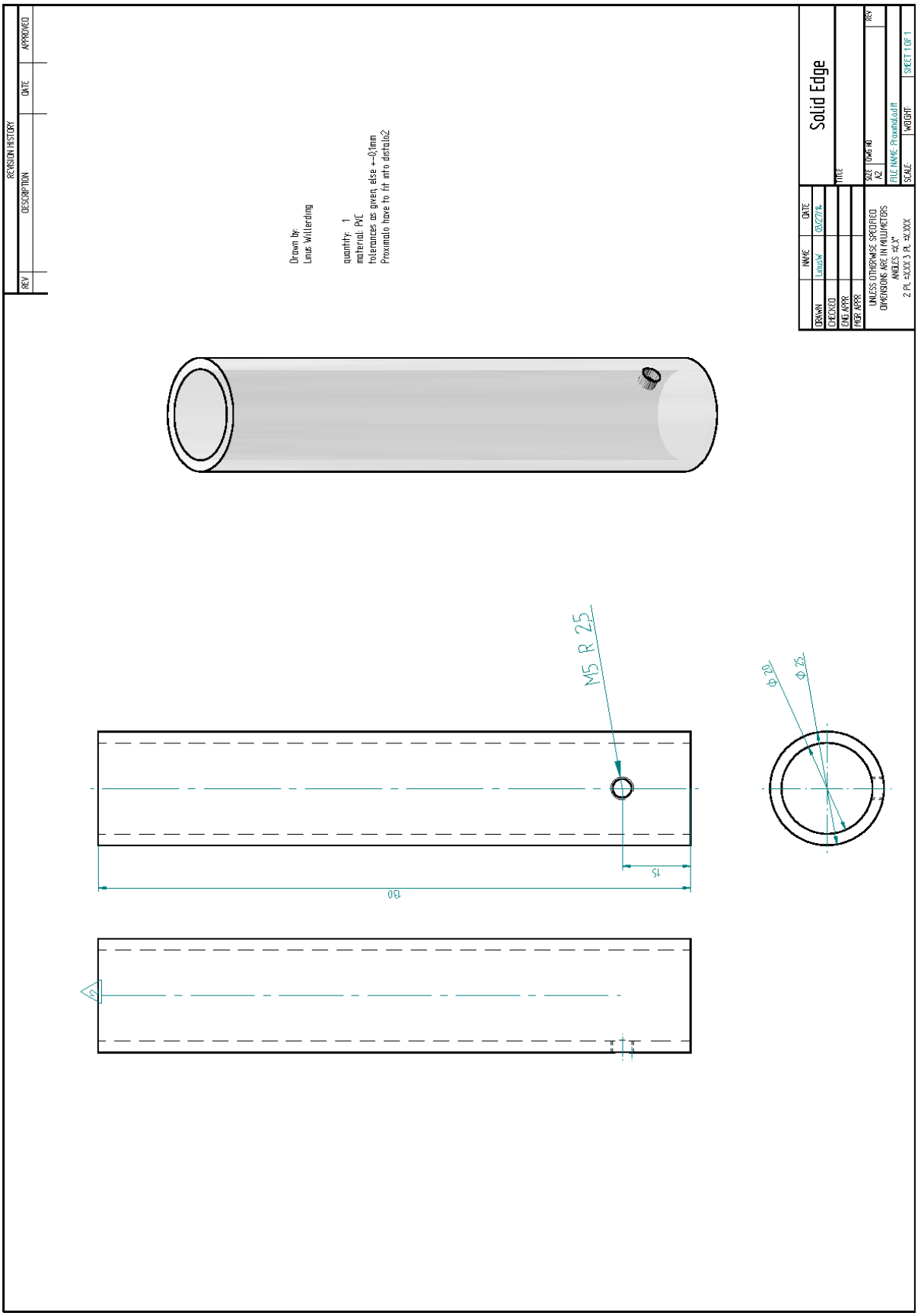

Supplementary figure 6: Inner tube

6.3 THERAPY MONITORING WITH MRI

6.3.1 CHARACTERIZATION OF LIPOSOMES

	Lipid (mM)	DOX CA (mM)	DOX/Lipid CA/Lipid (mol/mol)	z average (nm)	PDI	Zeta potential (mV)	$DPPG_2$ (%)	Lyso-PC (%)
DOX-TSL	**30.9** ± 6.9	**3.8** ± 0.1	**0.13** ± 0.03	**118** ± 4	**0.09** ± 0.01	**-27.9** ± 1.8	**25.7** ± 10.1	**0.6** ± 1.0
CA-TSL	**29.5** ± 2.7	**12.9** ± 2.7	**0.44** ± 0.12	**128** ± 24	**0.12** ± 0.08	**-20.6** ± 1.9	**24.9** ± 6.0	**0.0** ± 0.0

Supplementary table 4: Characterization of DPPC/DSPC/$DPPG_2$ 50:20:30 (mol/mol) TSL ($DPPG_2$-TSL) formulations with encapsulated DOX and Gd-DTPA-BMA. Three independent preparations have been used. The molar content of $DPPG_2$ and Lyso-PC was quantified with thin layer chromatography. Mean values are displayed with standard deviations. PDI: poly-dispersity index.

Temperature (°C)	k_{DOX} (10^{-4} s^{-1})
37	0.9 (0.895)
38	3.2 (0.917)
39	10.0 (0.992)
40	51.8 (0.998)
41	73.0 (0.895)
42	105.7 (0.954)

Supplementary table 5: Release kinetics of doxorubicin (DOX) from DPPC/DSPC/$DPPG_2$ 50:20:30 (mol/mol) TSL ($DPPG_2$-TSL) measured with fluorescence spectroscopy, as described previously [18]. Calculated DOX release rate constants k_{DOX} from measurements performed in FCS (n = 3). The coefficient of determination (R2) is given in parentheses.

Temperature (°C)	r_1 (s^{-1} mM^{-1})	SD (s^{-1} mM^{-1})
30.0	0.93	0.22
31.9	0.94	0.14
33.8	1.11	0.11
35.7	1.23	0.12
37.6	1.37	0.07
39.6	1.84	0.14
41.5	4.00	1.27
43.4	4.17	0.96
45.3	4.02	0.75
47.2	4.11	0.76
49.2	4.28	0.94

Supplementary table 6: Mean r1 relaxivity of CA-TSL (DPPC/DSPC/DPPG2) 50:20:30 (mol/mol) TSL (DPPG2-TSL) measured by a 0.47 T NMR-analyzer (Minispec NMS120, Bruker BioSpin GmbH, Rheinstetten, Germany) [88]. Experiments were performed in 1:20 dilution with FCS/0.9% saline 1:1 (vol/vol), as described previously [18].

6.3.2 SUPPLEMENTARY DATA

	Correlation coefficient between HPLC DOX-concentration of the **medial and lateral parts of the heated tumor** and the **unheated tumor** to the corresponding ROI values of:	r-value	p-value
static data	T_1_1FA_treatment_rel [%]	-0.875	0.000
	T_1_1FA_treatment_abs [ms]	-0.826	0.000
	T_1_1FA_total_rel [%]	-0.782	0.000
	T_1_1FA_total_abs [ms]	-0.661	0.003
	T_1_7FA_rel [%]	-0.207	0.410
	T_1_7FA_abs [ms]	-0.470	0.077
	Phase_abs [rad]	-0.842	0.001
dynamic data	Phase_AUC [rad*s]	-0.862	0.000
	T_1_1FA_AUC_rel [%*s]	-0.843	0.000
	T_1_1FA_AUC_abs [ms*s]	-0.794	0.000

Supplementary table 7: Correlation of DOX concentration with different MRI parameters with corresponding p-value (0.000 → p<0.0005). Medial and lateral parts of the heated tumor and the unheated tumor were used for correlation.

		Doxorubicin concentration [ng/mg]		
		A		**B**
		DOX heated tumor	**Dox unheated tumor**	**Dox unheated tumor**
static data	**T_1_1FA_treatment_rel [%]**	10.6 (4.1)	1.6 (2.7)	1.7 (2.4)
	T_1_1FA_treatment_abs [ms]	10.5 (4.8)	1.8 (3.2)	1.6 (2.6)
	T_1_1FA_total_rel [%]	9.7 (6.8)	1.6 (3.9)	2.7 (2.3)
	T_1_1FA_total_abs [ms]	9.4 (8.2)	1.7 (6.0)	2.9 (2.9)
	T_1_7FA_rel [%]	9.1 (9.59	-3.2 (5.5)	7.0 (2.7)
	T_1_7FA_abs [ms]	8.8 (12.1)	-2.9 (7.4)	7.0 (3.6)
	Phase_abs [rad]	10.7 (4.8)	2.9 (1.6)	0.4 (1.3)
dynamic data	**Phase_AUC [rad*s]**	10.6 (4.0)	3.5 (1.6)	-0.2 (2.3)
	T_1_1FA_AUC_rel [%*s]	11.2 (2.4)	3.2 (2.7)	-0.4 (3.7)
	T_1_1FA_AUC_abs [ms*s]	10.6 (4.7)	2.5 (2.7)	0.8 (1.6)
	HPLC	10.6 (2.6)	1.2 (0.4)	2.1 (1.1)

Supplementary table 8: Mean doxorubicin concentration determined for whole tumors by MRI and HPLC analysis.). SD is given in parentheses.

		Doxorubicin concentration [ng/mg]				
		A		B		A+B
		Medial half	Lateral half	Medial half	Lateral half	Muscle
static data	**T_1_1FA_treatment_rel [%]**	13.2 (4.3)	9.5 (4.1)	2.9	3.7	0.3 (0.6)
	T_1_1FA_treatment_abs [ms]	12.0 (4.4)	10.2 (4.7)	1.1	3.5	-1.3 (0.7)
	T_1_1FA_total_rel [%]	11.6 (8.3)	9.7 (6.1)	4.2	5.1	-6.7 (2.4)
	T_1_1FA_total_abs [ms]	9.8 (8.9)	10.6 (7.6)	2.2	5.9	-9.8 (2.5)
	T_1_7FA_rel [%]	8.2 (12.1)	9.6 (7.3)	9.6	8.2	-14.4 (3.7)
	T_1_7FA_abs [ms]	6.1 (13.2)	11.1 (9.6)	7.8	5.7	-17.4 (3.7)
	Phase_abs [rad]	11.5 (5.3)	10.0 (4.6)	0.9	0.5	-0.5 (0.6)
dynamic data	**Phase_AUC [rad*s]**	11.9 (4.9)	11.1 (3.4)	3.2	1.8	-0.9 (0.5)
	T_1_1FA_AUC_rel [%*s]	11.5 (3.1)	9.1 (3.5)	-2.9	2.2	-0.7 (1.2)
	T_1_1FA_AUC_abs [ms*s]	13.3 (4.8)	8.7 (4.3)	2.8	0.8	-0.4 (1.0)
	HPLC	14.1 (3.9)	9.0 (3.0)	2.7	2.3	*0.5 (0.1)

Supplementary table 9: Mean doxorubicin concentration for bisected tumors and non-heated muscle tissue for MRI and HPLC analysis. *DOX was determined in preceding experiments [87]. SD is given in parentheses. Because group B consisted only of two bisected tumors, values were stated without DS.

linear regression of MRI Parameter and HPLC DOX concentration for the lateral, medial heated tumor parts and the unheated tumor				
regression with HPLC DOX-concentration and		Slope (m)	Intercept (a)	r^2
static data	T_1 1FA total abs [ms]	-23.44	-371.85	0.468
	T_1 1FA total rel [%]	-20.17	-22.55	0.612
	T_1 1FA treatment abs [ms]	-36.55	-370.58	0.709
	T_1 1FA treatment rel[%]	-2.41	-23.26	0.777
	T_1 7FA abs [ms]	-16.72	-431.63	0.238
	T_1 7FA rel [%]	-0.062	-25.11	0.281
	Phase difference [rad]	-0.061	0.022	0.538
dynamic data	AUC of dynamic phase [rad*s]	-85.93	-402-02	0.619
	AUC of dynamic T_1 [%*s]	$-8.50*10^{-3}$	$-66.01*10^{-3}$	0.726
	AUC of dynamic T_1 [ms*s]	$-1.13*10^{-5}$	$-9.77*10^{-5}$	0.667

Supplementary table 10: Linear regression of MRI Parameter vs. HPLC DOX concentration.

Linear regression of MRI calculated DOX and HPLC DOX concentration					
regression with HPLC DOX and MRI DOX of		Slope	intercept	r^2	**RPC (ng/mg)**
static data	T_1_1FA_treatment_rel	0.80	1.18	0.818	**5.6**
	T_1_1FA_treatment_abs	0.78	1.10	0.765	**6.6**
	T_1_1FA_total_rel	0.79	0.40	0.658	**9.0**
	T_1_1FA_total_abs	0.64	1.24	0.550	**11.4**
	T_1_7FA_rel	0.47	2.21	0.405	**18.9**
	T_1_7FA_abs	0.39	2.71	0.377	**19.5**
	Phase_abs	0.78	1.25	0.760	**7.3**
dynamic data	Phase_AUC	0.83	0.78	0.813	**5.8**
	T_1_1FA_AUC_rel	0.78	1.19	0.772	**6.9**
	T_1_1FA_AUC_abs	0.76	1.26	0.721	**6.8**

Supplementary table 11: Linear regression for measured vs. calculated DOX values for lateral, medial-heated tumor parts and the unheated tumor ROI in [(ng/mg)/(ng/mg)]. Data were generated with data from supplementary table 10. RPC factor is generated from the Bland Altman plot.

7. ABBREVIATIONS

AUC	area under the curve
CA	contrast agent
CAD	computer-aided design
cm^2	square centimeter
CT	computed tomography
CW	continuous wave
DAM	double angle method
DNA	deoxyribonucleic acid
DOX	doxorubicin
$DPPG_2$	1,2-dipalmitoyl-*sn*-glycero-3-phosphodiglycerol
DSPC	1,2-dipalmitoyl-sn-glycero-3-phosphocholine
EPR	enhanced permeability and retention
e.g.	for example (exempli gratia)
FA	flip angle
FCS	fetal calf serum
FID	free induction decay
FUS	focused ultrasound
FOV	field of view
Gd	gadolinium
GRE	gradient echo
HIFU	high intense focused ultrasound
HPLC	high pressure liquid chromatography
HT	hyperthermia
i. v.	intra venous
IR	infrared
LITT	laser induced thermotherapy
MRI	magnetic resonance imaging
NIR	near infrared
NMR	nuclear magnetic resonance
PDT	photo dynamic therapy
PET	positron emission tomography
Phase_AUC	AUC for PRFS
Phase_diff	absolute PRFS
PK	pharmacokinetic
PRFS	proton resonance frequency shift
RF	radio frequency
ROI	region of interest
RES	reticuloendothelial system
RPC	reproducibility coefficient
SD	standard deviation
SENSE	sensitivity encoding
SNR	signal to noise ratio
SPECT	single photon emission computed tomography
SR	saturation recovery
T_1	longitudinal relaxation time
T_1_1FA_AUC_abs	AUC for absolute T1 change during the treatment
T_1_1FA_AUC_rel	AUC for relative T1 change during the treatment
T_1_1FA_total_abs	absolute T_1 difference for total acquisition time
T_1_1FA_total_rel	relative T_1 difference for total acquisition time
T_1_1FA_treatment_rel	relative T_1 difference for the therapy time
T_1_1FA_treatment_abs	absolute T_1 difference for the therapy time
T_1_7FA_abs	absolute T_1 time difference for total acquisition time measured with 7 FA

T_1_7FA_rel	relative T_1 time difference for total acquisition time measured with 7 FA
T_2	transversal relaxation time
TE	echo time
TLC	thin layer chromatography
T_m	transition temperature
TSL	thermosensitive liposomes
TR	repetition time
TWIST	time-resolved angiography with stochastic trajectories
UV	ultra violet
VFA	variable flip angle
VOI	volume of interest
W	watt
VOI	volume of interest

8. REFERENCES

[1] International Agency for Research on Cancer. GLOBOCAN 2012: Estimated Cancer Incidence: Mortality and Prevalence Worldwide in 2012. [August 14, 2014]; Available from: http://globocan.iarc.fr/Pages/fact_sheets_cancer.aspx.

[2] Issels RD, Lindner LH, Verweij J, Wust P, Reichardt P, Schem B-C et al. Neo-adjuvant chemotherapy alone or with regional hyperthermia for localised high-risk soft-tissue sarcoma: a randomised phase 3 multicentre study. Lancet Oncol 2010;11(6):561–70.

[3] Kitamura K, Kuwano H, Watanabe M, Nozoe T, Yasuda M, Sumiyoshi K et al. Prospective randomized study of hyperthermia combined with chemoradiotherapy for esophageal carcinoma. J. Surg. Oncol. 1995;60(1):55–8.

[4] van der Zee, J, González González D, van Rhoon, G C, van Dijk, J D, van Putten, W L, Hart AA. Comparison of radiotherapy alone with radiotherapy plus hyperthermia in locally advanced pelvic tumours: a prospective, randomised, multicentre trial. Dutch Deep Hyperthermia Group. Lancet 2000;355(9210):1119–25.

[5] Datta NR, Bose AK, Kapoor HK, Gupta S. Head and neck cancers: results of thermoradiotherapy versus radiotherapy. Int. J Hyperthermia 1990;6(3):479–86.

[6] Overgaard J, Bentzen SM, Gonzalez Gonzalez D, Hulshof M, Arcangeli G, Dahl O et al. Randomised trial of hyperthermia as adjuvant to radiotherapy for recurrent or metastatic malignant melanoma. Lancet 1995;345(8949):540–3.

[7] Issels R, Lindner L, Ghadjar P, Reichardt P, Hohenberger P, Verweij J et al. (eds.). LATE BREAKING ABSTRACT: Improved overall survival by adding regional hyperthermia to neo-adjuvant chemotherapy in patients with localized high-risk soft tissue sarcoma (HR-STS): Long-term outcomes of the EORTC 62961/ESHO randomized phase III study; 2015.

[8] Issels RD. Regional hyperthermia in high-risk soft tissue sarcomas. Curr Opin Oncol 2008;20(4):438–43.

[9] Partanen A, Yarmolenko PS, Viitala A, Appanaboyina S, Haemmerich D, Ranjan A et al. Mild hyperthermia with magnetic resonance-guided high-intensity focused ultrasound for applications in drug delivery. Int. J Hyperthermia 2012;28(4):320–36.

[10] Koning GA, Eggermont AMM, Lindner LH, Hagen TLM ten. Hyperthermia and thermosensitive liposomes for improved delivery of chemotherapeutic drugs to solid tumors. Pharm. Res. 2010;27(8):1750–4.

[11] Landon CD, Park J-Y, Needham D, Dewhirst MW. Nanoscale Drug Delivery and Hyperthermia: The Materials Design and Preclinical and Clinical Testing of Low Tempera-

ture-Sensitive Liposomes Used in Combination with Mild Hyperthermia in the Treatment of Local Cancer. Open Nanomed J 2011;3:38–64.

[12] Manzoor AA, Lindner LH, Landon CD, Park J-Y, Simnick AJ, Dreher MR et al. Overcoming limitations in nanoparticle drug delivery: triggered, intravascular release to improve drug penetration into tumors. Cancer Research 2012;72(21):5566–75.

[13] Kong G, Braun RD, Dewhirst MW. Hyperthermia enables tumor-specific nanoparticle delivery: effect of particle size. Cancer Research 2000;60(16):4440–5.

[14] Li L, ten Hagen, Timo L.M., Bolkestein M, Gasselhuber A, Yatvin J, van Rhoon GC et al. Improved intratumoral nanoparticle extravasation and penetration by mild hyperthermia. J Control Release 2013;167(2):130–7.

[15] Li L, ten Hagen, Timo L.M., Haeri A, Soullié T, Scholten C, Seynhaeve AL et al. A novel two-step mild hyperthermia for advanced liposomal chemotherapy. J Control Release 2014;174:202–8.

[16] Lindner LH, Eichhorn ME, Eibl H, Teichert N, Schmitt-Sody M, Issels RD et al. Novel temperature-sensitive liposomes with prolonged circulation time. Clin. Cancer Res. 2004;10(6):2168–78.

[17] Hossann M, Wiggenhorn M, Schwerdt A, Wachholz K, Teichert N, Eibl H et al. In vitro stability and content release properties of phosphatidylglyceroglycerol containing thermosensitive liposomes. Biochim. Biophys. Acta 2007;1768(10):2491–9.

[18] Hossann M, Wang T, Wiggenhorn M, Schmidt R, Zengerle A, Winter G et al. Size of thermosensitive liposomes influences content release. J Control Release 2010;147(3):436–43.

[19] Hossann M, Syunyaeva Z, Schmidt R, Zengerle A, Eibl H, Issels RD et al. Proteins and cholesterol lipid vesicles are mediators of drug release from thermosensitive liposomes. J Control Release 2012;162(2):400–6.

[20] Limmer S, Hahn J, Schmidt R, Wachholz K, Zengerle A, Lechner K et al. Gemcitabine treatment of rat soft tissue sarcoma with phosphatidyldiglycerol-based thermosensitive liposomes. Pharm. Res. 2014;31(9):2276–86.

[21] Gensler D, Fidler F, Ehses P, Warmuth M, Reiter T, Düring M et al. MR safety: Fast T1 thermometry of the RF-induced heating of medical devices. MRM 2012;68(5):1593–9.

[22] Peller M, Löffler R, Baur A, Turner P, Abdel-Rahman S, Futschik G et al. MRT-gesteuerte regionale Tiefenhyperthermie. Radiologe 1999;39(9):756–63.

[23] Pahernik SA, Peller M, Dellian M, Loeffler R, Issels R, Reiser M et al. Validation of MR thermometry technology: a small animal model for hyperthermic treatment of tumours. Res Exp Med (Berl) 1999;199(2):59–71.

[24] Hijnen N, Langereis S, Grüll H. Magnetic resonance guided high-intensity focused ultrasound for image-guided temperature-induced drug delivery. Adv. Drug. Deliv. Rev. 2014;72:65–81.

[25] Grissom WA, Rieke V, Holbrook AB, Medan Y, Lustig M, Santos J et al. Hybrid referenceless and multibaseline subtraction MR thermometry for monitoring thermal therapies in moving organs. Med Phys 2010;37(9):5014–26.

[26] Viglianti BL, Abraham SA, Michelich CR, Yarmolenko PS, MacFall JR, Bally MB et al. In vivo monitoring of tissue pharmacokinetics of liposome/drug using MRI: illustration of targeted delivery. MRM 2004;51(6):1153–62.

[27] Sauer R. Strahlentherapie und Onkologie. 5th ed. München: Elsevier, Urban & Fischer; 2010.

[28] Bhatnagar A, Hustinx R, Alavi A. Nuclear imaging methods for non-invasive drug monitoring. Adv. Drug. Deliv. Rev. 2000;41(1):41–54.

[29] Viglianti BL, Ponce AM, Michelich CR, Yu D, Abraham SA, Sanders L et al. Chemodosimetry of in vivo tumor liposomal drug concentration using MRI. MRM 2006;56(5):1011–8.

[30] Matteucci ML, Anyarambhatla G, Rosner G, Azuma C, Fisher PE, Dewhirst MW et al. Hyperthermia increases accumulation of technetium-99m-labeled liposomes in feline sarcomas. Clin. Cancer Res. 2000;6(9):3748–55.

[31] Leander P, Månsson S, Ege T, Besjakov J. CT and MR imaging of the liver using liver-specific contrast media. A comparative study in a tumour model. Acta Radiol 1996;37(3 Pt 1):242–9.

[32] Remedy Health Media, LLC. Chemotherapy. [August 06, 2014]; Available from: http://www.healthcentral.com/encyclopedia/408/155.html.

[33] Tacar O, Sriamornsak P, Dass CR. Doxorubicin: an update on anticancer molecular action, toxicity and novel drug delivery systems. J. Pharm. Pharmacol. 2013;65(2):157–70.

[34] accord healthcare ltd. Fachinformation: Doxorubicin Accord 2mg/ml; 2013.

[35] Lindner LH, Issels RD. Hyperthermia in soft tissue sarcoma. Curr Treat Options Oncol 2011;12(1):12–20.

[36] Issels R, Kampmann E, Kanaar R, Lindner LH. Hallmarks of hyperthermia in driving the future of clinical hyperthermia as targeted therapy: translation into clinical application. Int J Hyperthermia 2016;32(1):89–95.

[37] Dewhirst MW, Vujaskovic Z, Jones E, Thrall D. Re-setting the biologic rationale for thermal therapy. Int. J Hyperthermia 2005;21(8):779–90.

[38] Soft tissue and visceral sarcomas: ESMO Clinical Practice Guidelines for diagnosis, treatment and follow-up. Ann Oncol 2014;25 Suppl 3:iii102-12.

[39] Bangham AD, Standish MM, Watkins JC. Diffusion of univalent ions across the lamellae of swollen phospholipids. J. Mol. Biol. 1965;13(1):238–52.

[40] Eibl H. Synthesis of glycerophospholipids. Chem. Phys. Lipids 1980;26(4):405–29.

[41] Lindner LH, Issels RD. Thermosensitive Liposomen für die regionale Hyperthermie. Dtsch. Med. Wochenschr 2003;128(39):2020–2.

[42] Mouritsen OG. Lipids, curvature, and nano-medicine. Eur J Lipid Sci Technol 2011;113(10):1174–87.

[43] Yatvin MB, Weinstein JN, Dennis WH, Blumenthal R. Design of liposomes for enhanced local release of drugs by hyperthermia. Science 1978;202(4374):1290–3.

[44] Svaasand LO, Gomer CJ, Morinelli E. On the physical rationale of laser induced hyperthermia. Laser Med. Sci. 1990;5(2):121–8.

[45] Jelínková H (ed.). Lasers for medical applications: Diagnostics, therapy, and surgery; 2013.

[46] Douplik A, Saiko G, Schelkanova I, Tuchin V. The response of tissue to laser light. In: Jelínková H, editor. Lasers for medical applications: Diagnostics, therapy, and surgery; 2013, p. 47–109.

[47] Berlien H-P. Safety and laser tissue interaction. Landsberg: Ecomed; 1989.

[48] Boulnois J-L. Photophysical processes in recent medical laser developments: A review. Laser Med. Sci. 1986;1(1):47–66.

[49] Bashkatov AN, Genina EA, Kochubey VI, Tuchin VV. Optical properties of human skin, subcutaneous and mucous tissues in the wavelength range from 400 to 2000 nm. J. Phys. D: Appl. Phys. 2005;38(15):2543–55.

[50] Wang LV, Wu H-i. Biomedical optics: Principles and imaging. Hoboken, N.J: Wiley-Interscience; 2007.

[51] Bloch F. Nuclear Induction. Phys. Rev. 1946;70(7-8):460–74.

[52] Purcell E, Torrey H, Pound R. Resonance Absorption by Nuclear Magnetic Moments in a Solid. Phys. Rev. 1946;69(1-2):37–8.

[53] Haacke EM. Magnetic resonance imaging: Physical principles and sequence design. New York: Wiley; 1999.

[54] Bernstein MA, King KF, Zhou XJ (eds.). Handbook of MRI pulse sequences. Amsterdam, Boston: Academic Press; 2004.

[55] Hanson LG. Is quantum mechanics necessary for understanding magnetic resonance? Concepts Magn Reson Part A Bridg Educ Res 2008;32A(5):329–40.

[56] Gold GE, Han E, Stainsby J, Wright G, Brittain J, Beaulieu C. Musculoskeletal MRI at 3.0 T: Relaxation Times and Image Contrast. AJR Am J Roentgenol 2004;183(2):343–51.

[57] Carr H, Purcell E. Effects of Diffusion on Free Precession in Nuclear Magnetic Resonance Experiments. Phys. Rev. 1954;94(3):630–8.

[58] Haase A, Frahm J, Matthaei D, Hanicke W, Merboldt K-D. FLASH imaging. Rapid NMR imaging using low flip-angle pulses. J. of Magn. Reson. 1986;67(2):258–66.

[59] Bernstein MA. Basic Pulse Sequences: Gradient Echo. In: Bernstein MA, King KF, Zhou XJ, editors. Handbook of MRI pulse sequences. Amsterdam, Boston: Academic Press; 2004, p. 579–605.

[60] Fram EK, Herfkens RJ, Johnson GA, Glover GH, Karis JP, Shimakawa A et al. Rapid calculation of T1 using variable flip angle gradient refocused imaging. Magn Reson Imaging 1987;5(3):201–8.

[61] Brookes JA, Redpath TW, Gilbert FJ, Needham G, Murray AD. Measurement of spin-lattice relaxation times with FLASH for dynamic MRI of the breast. Br J Radiol 1996;69(819):206–14.

[62] Dietrich O, Freiermuth M, **Willerding L**, Reiser MF, Peller M. Flip angle-optimized fast dynamic T1 mapping with a 3D gradient echo sequence. Magn Reson Med 2015(73):1158–63.

[63] Rieke V, Butts-Pauly K. MR thermometry. JMRI 2008;27(2):376–90.

[64] Bloembergen N, Purcell EM, Pound RV. Relaxation effects in Nuclear Magnetic Resonance Absorption. Phys. Rev. 1948(73):679–712.

[65] Parker DL. Applications of NMR imaging in hyperthermia: an evaluation of the potential for localized tissue heating and noninvasive temperature monitoring. IEEE Trans Biomed Eng 1984;31(1):161–7.

[66] Abragam A. Principles of nuclear magnetism. Oxford: Clarendon Press; 1983(1986).

[67] Parker DL, Smith V, Sheldon P, Crooks LE, Fussell L. Temperature distribution measurements in two-dimensional NMR imaging. Med Phys 1983;10(3):321–5.

[68] Hindman JC. Proton Resonance Shift of Water in the Gas and Liquid States. J. Chem. Phys. 1966;44(12):4582.

[69] Poorter J de. Noninvasive MRI thermometry with the proton resonance frequency method: study of susceptibility effects. MRM 1995;34(3):359–67.

[70] Poorter J de, Wagter C de, Deene Y de, Thomsen C, Ståhlberg F, Achten E. Noninvasive MRI thermometry with the proton resonance frequency (PRF) method: in vivo results in human muscle. MRM 1995;33(1):74–81.

[71] Hao D, Ai T, Goerner F, Hu X, Runge VM, Tweedle M. MRI contrast agents: Basic chemistry and safety. JMRI 2012;36(5):1060–71.

[72] Ai T, Morelli JN, Hu X, Hao D, Goerner FL, Ager B et al. A historical overview of magnetic resonance imaging, focusing on technological innovations. Invest. Radiol. 2012;47(12):725–41.

[73] Fossheim SL, Fahlvik AK, Klaveness J, Muller RN. Paramagnetic liposomes as MRI contrast agents: influence of liposomal physicochemical properties on the in vitro relaxivity. Magn Reson Imaging 1999;17(1):83–9.

[74] Peller M, Schwerdt A, Hossann M, Reinl HM, Wang T, Sourbron S et al. MR characterization of mild hyperthermia-induced gadodiamide release from thermosensitive liposomes in solid tumors. Invest. Radiol. 2008;43(12):877–92.

[75] Peller M, Kurze V, Loeffler R, Pahernik S, Dellian M, Goetz AE et al. Hyperthermia induces T1 relaxation and blood flow changes in tumors. A MRI thermometry study in vivo. Magn Reson. Imaging 2003;21(5):545–51.

[76] Needham D, Anyarambhatla G, Kong G, Dewhirst MW. A new temperature-sensitive liposome for use with mild hyperthermia: characterization and testing in a human tumor xenograft model. Cancer Research 2000;60(5):1197–201.

[77] Kong G, Anyarambhatla G, Petros WP, Braun RD, Colvin OM, Needham D et al. Efficacy of liposomes and hyperthermia in a human tumor xenograft model: importance of triggered drug release. Cancer Research 2000;60(24):6950–7.

[78] Li L, ten Hagen, Timo L.M., Hossann M, Süss R, van Rhoon GC, Eggermont AM et al. Mild hyperthermia triggered doxorubicin release from optimized stealth thermosensitive liposomes improves intratumoral drug delivery and efficacy. J Control Release 2013;168(2):142–50.

[79] Sien H, Jain R. Intratumour temperature distributions during hyperthermia. J Therm Biol 1980;5(2):127–30.

[80] Morita K, Zywietz F, Kakinuma K, Tanaka R, Katoh M. Efficacy of doxorubicin thermosensitive liposomes (40 degrees C) and local hyperthermia on rat rhabdomyosarcoma. Oncol. Rep. 2008;20(2):365–72.

[81] Ickenstein LM. Triggered drug release from thermosensitive liposomes. Ottawa: National Library of Canada; 2003.

[82] Dou YN, Zheng J, Foltz WD, Weersink R, Chaudary N, Jaffray DA et al. Heat-activated thermosensitive liposomal cisplatin (HTLC) results in effective growth delay of cervical carcinoma in mice. J Control Release 2014;178:69–78.

[83] Hijnen NM, Heijman E, Köhler MO, Ylihautala M, Ehnholm GJ, Simonetti AW et al. Tumour hyperthermia and ablation in rats using a clinical MR-HIFU system equipped with a dedicated small animal set-up. Int. J Hyperthermia 2012;28(2):141–55.

[84] Novák P, Moros EG, Parry JJ, Rogers BE, Myerson RJ, Zeug A et al. Experience with a small animal hyperthermia ultrasound system (SAHUS): report on 83 tumours. Phys. Med. Biol. 2005;50(21):5127–39.

[85] Locke J, Zeug A, Thompson Jr D, Allan J, Mazzarella K, Novak P et al. Localized versus regional hyperthermia: Comparison of xenotransplants treated with a small animal

ultrasound system and waterbath limb immersion. Int. J Hyperthermia 2005;21(3):271–81.

[86] Rebecca Schmidt. Neuartige thermosensitive Liposomen zur zielgerichteten Therapie solider Tumoren - Charakterisierung in vitro und in vivo: Novel thermosensitive liposomes for targeted therapy of solid tumours – characterization in vitro and in vivo [Dissertation]. Munich: Ludwig-Maximilians-University; 2011.

[87] **Willerding L**, Limmer S, Hossann M, Zengerle A, Wachholz K, Ten Hagen, L M Timo et al. Method of hyperthermia and tumor size influences effectiveness of doxorubicin release from thermosensitive liposomes in experimental tumors. J Control Release 2016(222):47–55.

[88] Hossann M, Wang T, Syunyaeva Z, Wiggenhorn M, Zengerle A, Issels RD et al. Non-ionic Gd-based MRI contrast agents are optimal for encapsulation into phosphatidyldiglycerol-based thermosensitive liposomes. J Control Release 2013;166(1):22–9.

[89] Sapareto SA, Dewey WC. Thermal dose determination in cancer therapy. Int. J. Radiat. Oncol. Biol. Phys. 1984;10(6):787–800.

[90] Kogelnik H, Li T. Laser beams and resonators. Appl Opt 1966;5(10):1550–67.

[91] Galettis P, Boutagy J, Ma DD. Daunorubicin pharmacokinetics and the correlation with P-glycoprotein and response in patients with acute leukaemia. Br. J. Cancer 1994;70(2):324–9.

[92] Schwartz HS, Grindey GB. Adriamycin and daunorubicin: a comparison of antitumor activities and tissue uptake in mice following immunosuppression. Cancer Research 1973;33(8):1837–44.

[93] Janssen J, Laatz W. Statistische Datenanalyse mit SPSS: Eine anwendungsorientierte Einführung in das Basissystem und das Modul Exakte Tests. 8th ed. Berlin: Springer; 2012.

[94] Dombrovsky LA, Timchenko V, Jackson M. Indirect heating strategy for laser induced hyperthermia: An advanced thermal model. Int J Heat Mass Transf 2012;55(17-18):4688–700.

[95] Svaasand LO, Boerslid T, Oeveraasen M. Thermal and optical properties of living tissue: application to laser-induced hyperthermia. Lasers Surg. Med. 1985;5(6):589–602.

[96] Waldow SM, Morrison PR, Grossweiner LI. Nd:YAG laser-induced hyperthermia in a mouse tumor model. Lasers Surg. Med. 1988;8(5):510–4.

[97] Dewhirst MW, Viglianti BL, Lora-Michiels M, Hanson M, Hoopes PJ. Basic principles of thermal dosimetry and thermal thresholds for tissue damage from hyperthermia. Int. J Hyperthermia 2003;19(3):267–94.

[98] Rhoon GC, Samaras T, Yarmolenko PS, Dewhirst MW, Neufeld E, Kuster N. CEM43°C thermal dose thresholds: a potential guide for magnetic resonance radiofrequency exposure levels? Eur. Radiol. 2013;23(8):2215–27.

[99] Yarmolenko PS, Moon EJ, Landon C, Manzoor A, Hochman DW, Viglianti BL et al. Thresholds for thermal damage to normal tissues: An update. Int. J Hyperthermia 2011;27(4):320–43.

[100] Waldow SM, Russell GE, Wallner PE. Microprocessor-controlled Nd:YAG laser for hyperthermia induction in the RIF-1 tumor. Lasers Surg. Med. 1992;12(4):417–24.

[101] Ponce AM, Viglianti BL, Yu D, Yarmolenko PS, Michelich CR, Woo J et al. Magnetic Resonance Imaging of Temperature-Sensitive Liposome Release: Drug Dose Painting and Antitumor Effects. JNCI 2007;99(1):53–63.

[102] Lindner LH, Hossann M. Factors affecting drug release from liposomes. Curr Opin Drug Discov Devel 2010;13(1):111–23.

[103] Karino T, Koga S, Maeta M. Experimental studies of the effects of local hyperthermia on blood flow, oxygen pressure and pH in tumors. Jpn J Surg 1988;18(3):276–83.

[104] Song CW. Effect of local hyperthermia on blood flow and microenvironment: a review. Cancer Research 1984;44(10 Suppl):4721.

[105] Smet M de, Langereis S, van den Bosch S, Bitter K, Hijnen NM, Heijman E et al. SPECT/CT imaging of temperature-sensitive liposomes for MR-image guided drug delivery with high intensity focused ultrasound. J Control Release 2013;169(1-2):82–90.

[106] Fossheim SL, Colet JM, Månsson S, Fahlvik AK, Muller RN, Klaveness J. Paramagnetic liposomes as magnetic resonance imaging contrast agents. Assessment of contrast efficacy in various liver models. Invest. Radiol. 1998;33(11):810–21.

[107] Hijnen NM, Elevelt A, Pikkemaat J, Bos C, Bartels LW, Grüll H. The magnetic susceptibility effect of gadolinium-based contrast agents on PRFS-based MR thermometry during thermal interventions. J Ther Ultrasound 2013;1(1):8.

[108] Smet M de, Heijman E, Langereis S, Hijnen NM, Grüll H. Magnetic resonance imaging of high intensity focused ultrasound mediated drug delivery from temperature-sensitive liposomes: An in vivo proof-of-concept study. J Control Release 2011;150(1):102–10.

[109] Hey S, Smet M de, Stehning C, Grüll H, Keupp J, Moonen CTW et al. Simultaneous T1 measurements and proton resonance frequency shift based thermometry using variable flip angles. MRM 2011;67(2):457–63.

[110] Peller M, **Willerding L**, Limmer S, Hossann M, Dietrich O, Ingrisch M et al. Surrogate MRI markers for hyperthermia-induced release of doxorubicin from thermosensitive liposomes in tumors. J Control Release 2016;237:138–46.

[111] Song T, Laine AF, Chen Q, Rusinek H, Bokacheva L, Lim RP et al. Optimal k-space sampling for dynamic contrast-enhanced MRI with an application to MR renography. MRM 2009;61(5):1242–8.

[112] Laub G, Kroeker R. syngo TWIST for Dynamic Time-Resolved MR Angiography. Magnetom Flash 2006(3):92–5.

[113] Cunningham CH, Pauly JM, Nayak KS. Saturated double-angle method for rapidB1+ mapping. MRM 2006;55(6):1326–33.

[114] Stollberger R, Wach P, McKinnon G, Justich E, Ebner F. Rf-field mapping in vivo. In: Proceedings of the 7th Annual Meeting of SMRM, CA, USA, 1988, p. 106.

[115] Insko E, Bolinger L. B1 Mapping. In: Proceedings of the 11th Annual Meeting of SMRM, Berlin, Germany, 1992, p. 4302.

[116] Balezeau F, Eliat P-A, Cayamo AB, Saint-Jalmes H. Mapping of low flip angles in magnetic resonance. Phys. Med. Biol. 2011;56(20):6635–47.

[117] Markwardt CB. Unwrap phase jumps to recover cycle counts: http://www.physics.wisc.edu/~craigm/idl/down/phunwrap.pro. USA; 2006.

[118] Krouwer JS. Why Bland-Altman plots should use X, not (Y+X)/2 when X is a reference method. Stat Med 2008;27(5):778–80.

[119] Lindner LH, Hossann M, Vogeser M, Teichert N, Wachholz K, Eibl H et al. Dual role of hexadecylphosphocholine (miltefosine) in thermosensitive liposomes: active ingredient and mediator of drug release. J Control Release 2008;125(2):112–20.

[120] Arzneimittel-Kompendium der Schweiz. Fachinformation Omniscan; 2007.

[121] Stanisz GJ, Odrobina EE, Pun J, Escaravage M, Graham SJ, Bronskill MJ et al. T1, T2 relaxation and magnetization transfer in tissue at 3T. MRM 2005;54(3):507–12.

[122] Dietrich O, Freiermuth M, **Willerding L**, Peller M, Reiser M. Fast dynamic measurements of T1 relaxation times: influence and correction of T2* effects. In: Proceeding of the 23rd Annual Meeting and Exhibition; 2015, p. 443.

[123] Todd N, Diakite M, Payne A, Parker DL. Hybrid proton resonance frequency/T(1) technique for simultaneous temperature monitoring in adipose and aqueous tissues. MRM 2013;69(1):62–70.

[124] Rieke V, Vigen KK, Sommer G, Daniel BL, Pauly JM, Butts-Pauly K. Referenceless PRF shift thermometry. MRM 2004;51(6):1223–31.

[125] Schenck JF. The role of magnetic susceptibility in magnetic resonance imaging: MRI magnetic compatibility of the first and second kinds. Med Phys 1996;23(6):815–50.

[126] Tagami T, Foltz WD, Ernsting MJ, Lee CM, Tannock IF, May JP et al. MRI monitoring of intratumoral drug delivery and prediction of the therapeutic effect with a multifunctional thermosensitive liposome. Biomaterials 2011;32(27):6570–8.

[127] Rohrer M, Bauer H, Mintorovitch J, Requardt M, Weinmann H-J. Comparison of magnetic properties of MRI contrast media solutions at different magnetic field strengths. Invest. Radiol. 2005;40(11):715–24.

[128] Korporaal JG, van den Berg CAT, van Osch, Matthias MJP, Groenendaal G, van Vulpen M, van der Heide UA. Phase-based arterial input function measurements in the femoral arteries for quantification of dynamic contrast-enhanced (DCE) MRI and comparison with DCE-CT. MRM 2011;66(5):1267–74.

[129] Yeo SY, Smet M de, Langereis S, Vander Elst L, Muller RN, Grüll H. Temperature-sensitive paramagnetic liposomes for image-guided drug delivery: Mn(2+) versus [Gd(HPDO3A)(H2O)]. Biochim. Biophys. Acta 2014;1838(11):2807–16.

[130] Tilcock. Delivery of contrast agents for magnetic resonance imaging, computed tomography, nuclear medicine and ultrasound. Advanced Drug Delivery Reviews 1999;37(1-3):33–51.

[131] Hijnen NM, Elevelt A, Grüll H. Stability and trapping of magnetic resonance imaging contrast agents during high-intensity focused ultrasound ablation therapy. Invest Radiol 2013;48(7):517–24.

9. FIGURES

10. TABLES

11. AFFIDAVIT

Willerding, Linus Johannes

Ich erkläre hiermit an Eides statt,

dass ich die vorliegende Dissertation mit dem Thema

“Surrogate MRI markers for chemodosimetry of doxorubicin with thermosensitive liposomes in tumors”

selbständig verfasst, mich außer der angegebenen keiner weiteren Hilfsmittel bedient und alle Erkenntnisse, die aus dem Schrifttum ganz oder annähernd übernommen sind, als solche kenntlich gemacht und nach ihrer Herkunft unter Bezeichnung der Fundstelle einzeln nachgewiesen habe.

Ich erkläre des Weiteren, dass die hier vorgelegte Dissertation nicht in gleicher oder in ähnlicher Form bei einer anderen Stelle zur Erlangung eines akademischen Grades eingereicht wurde.

München, den 4 Dezember 2017 _____